Title
Analysis & Simulation of Dynamics in Supercooled Liquids

Author
Elmatad, Yael Sarah

Publication Date
2011

Peer reviewed|Thesis/dissertation

Analysis & Simulation of Dynamics in Supercooled Liquids

by

Yael Sarah Elmatad

A dissertation submitted in partial satisfaction of the
requirements for the degree of
Doctor of Philosophy

in

Chemistry

in the

Graduate Division

of the

University of California, Berkeley

Committee in charge:

Professor David Chandler, Chair
Professor Phillip L. Geissler
Assistant Professor Jhih-Wei Chu

Fall 2011

Analysis & Simulation of Dynamics in Supercooled Liquids

Abstract

Analysis & Simulation of Dynamics in Supercooled Liquids

by

Yael Sarah Elmatad

Doctor of Philosophy in Chemistry

University of California, Berkeley

Professor David Chandler, Chair

The nature of supercooled liquids and the glass transition has been debated by many scientists. Several theories have been put forth to describe the remarkable properties of this out-of-equilibrium material. Each of these theories makes specific predictions as to how the scaling of various transport properties in supercooled materials should behave. Given access to a large pool of high-quality supercooled liquid data we seek to compare these theories to one another. Moreover, we explore properties of a pair of models which are the basis for one particularly attractive theory - Chandler-Garrahan theory - and discuss the models' behavior in space-time and possible implications to the behavior of experimental supercooled liquids.

Here we investigate the nature of dynamics in supercooled liquids using a two pronged approach. First we analyze the transport properties found in experiments and simulations of supercooled liquids. Then, we analyze simulation trajectories for lattice models which reproduce many of the interesting properties of supercooled liquids. In doing so, we illuminate several glass universalities, common properties of a wide variety of glass formers.

By analyzing relaxation time and viscosity data for over 50 data sets and 1200 points [1], we find that relaxation time can be collapsed onto a single, parabolic curve. This collapse supports a theory of universal glass behavior based on facilitated models proposed by David Chandler and Juan Garrahan in 2003. We then show that the parabolic fit parameters for any particular liquid are a *material property*: they converge fast and are capable of predicting behavior in regions beyond the included data sets. We compare this property to other popular fitting schemes such as the Vogel-Fulcher, double exponential, and fractional exponential forms and conclude that these three forms result in parameters which are non predictive and therefore not material properties [2]. Additionally, we examine the role of attractive forces in liquids by comparing simulations of a Lennard-Jones mixture, which contains both attractions and repulsions, with that of a Weeks-Chandler-Andersen mixture, which only retains repulsive forces. We show that within the framework of the parabolic collapse, these two liquids behave identically. This suggests that attractive forces do not play a key role in glassy dynamics. Rather, repulsive forces - as has been shown in dense

liquids - play the largest contributing role in jamming systems into glassy states. We further investigate the predicted fragile-to-strong crossover in glass formers and find no compelling evidence for the crossover in bulk materials at this time [3].

Additionally, we study ensembles of trajectories for a specific class of kinetically constrained models which reproduce the dynamic heterogeneity found in real glass formers. The one dimensional models we consider are the Fredrickson-Andersen (FA) model and the east model. These two models have been shown to behave as supercooled liquids reproducing properties such as the breakdown of the Stokes-Einstein equation relating diffusion constants and relaxation times. We use transition path sampling in the s-ensemble to bias the system into low activity regions. It has been previously shown that the FA model goes through a first-order dynamical phase transition in trajectory space. We extend this to include a slightly softened FA model, which we believe to be more representative of atomistic systems. We have determined that this first order coexistence line ends in a critical point where the surface tension between active and inactive trajectories in space-time disappears [4]. Beyond this region as the softened FA model becomes unconstrained, the transition disappears and no phase transition is detected. Beyond simulations, these results were verified by analytical methods. This verification was achieved by mapping of soft FA model onto a model which undergoes a quantum phase transition. Beyond the FA model, we consider the softened east model. Unlike the FA model, however, the east model relaxes hierarchically and has a particular directionality. Many of the same conclusions - such as the appearance of a non-trivial critical point in space time - appear in the east model. Moreover, many of the same analytical tools can be used to determine the symmetry line that separates the active and inactive phases. However, the exact mapping of the critical point location is unknown and the location of the critical point is determined numerically. We also investigate how the inactive phase created by applying a dynamical field relaxes to the active state under no external field and find that the process appears barrierless.

Lastly, we propose current and ongoing work which seeks to understand how to numerically quantify the degree to which a system is dynamically facilitated by looking at multipoint correlation functions of endured kinks. We contrast this method with previously suggested methods based on locating avalanches by testing both methods on kinetically constrained models such as the east and FA models.

To my little brother, Dorr Elmatad.

Contents

List of Figures

List of Tables

Acknowledgments

First and foremost I would like to thank my advisor, Professor David Chandler, for all his help throughout out the years in his role as teacher and mentor. He has helped me navigate the waters of science as well as helped me to be confident about my convictions. I could not have asked for a better role model.

I would further like to thank all of the brilliant young scientists who have passed through the Chandler group and the Pitzer center during my tenure including, in no particular order, Dr. Lester Hedges, Dr. Adam Willard, Dr. Ulf Pedersen, Dr. Param Dhillon, Dr. Kafui Tay, Dr. Thomas Speck, Dr. John Chodera, Dr. Lutz Maibaum, Professor Michael Hagan, Professor Tommy Miller, Dr. Aaron Keys, James MacFadyen, David Kelsey, David Limmer, Patrick Varilly, Patrick Shaffer, Todd Gingrich, and Ayelet Benjamini.

I would like to especially thank Dr. Robert Jack who was instrumental in mentoring me during my first years as a graduate student. Without his patience for all my early growing pains I would not have been able to accomplish as much as I have.

And to Professor Juan Garrahan for helping me during the beginning, least of which was allowing me to spend two very fruitful months with him at the University of Nottingham in Spring of 2010.

I would like to thank Professor Phillip Geissler for his help over the years and especially for being an exemplary teacher. Additionally, I would like to thank the Geissler Group for making me feel like I had a large "extended" scientific family.

I give my gratitude to Dr. Douglas Ashton and Antonia Mey for showing me that England isn't just about gloomy grey fog.

I would like to thank the ladies of Iota Sigma Pi for helping me stay connected to the larger community of women in science and for helping me remember that there is always work left to be done.

Of course, to my parents - Sima and Ilan Elmatad, for always giving me enough space to decide my own path and encouraging me no matter what my decision - even if it involved a 3,000 mile separation. And to my brothers Tal and Dorr who remind me constantly what a big dork I am.

Last, but certainly not least, to Christopher Ryan who has always been my biggest cheerleader throughout these past 5 years. I don't think I could have done it without him.

Chapter 1

Introduction

1.1 The Glass Transition

Glasses are materials that are formed when liquids are cooled below their melting point, T_{m}, but do not undergo the first-order phase transition into a crystalline, ordered solid. Instead, these liquids transition into supercooled liquids. Using simple measures, supercooled liquids appear to be structurally indistinguishable from ordinary liquids but possess interesting dynamical properties [23, 24]. The change from a liquid to a supercooled liquid is a reversible process and thus the supercooled liquid remains in equilbrium [1]. As the material is further cooled it falls out of equilibrium and becomes an arrested amorphous solid, also known as *a glass* at a glass transition temperature T_{g}. This temperature varies only slightly with the rate of cooling.

At T_{g} the material does not undergo a static phase transition. For example, in Figure 1.1 the density as a function of temperature is shown for freezing as well as for a glass transition. At T_{m} the density jumps discontinuously as the liquid undergoes a first order phase transition from a liquid to a solid [25]. However, at T_{g} no such jump is detected [26]. In fact, no known structural order parameters can distinguish between a liquid and a glass [23] and, therefore, the glass transition does not appear to to be a manifestation of a first-order static phase transition using any currently known order parameter.

1.2 Supercooled Liquid Phenomenology

1.2.1 Self-Intermediate Scattering Function

Two point correlation functions such as the density pair-correlation function $g(r)$ in supercooled liquids vary little from that of their normal liquid counterparts. However, there is a dynamical signature in the self-intermediate scattering function, $F_{\mathrm{s}}(k,t)$. The self-intermediate scattering function correlates a particle's position at time 0 with its position at

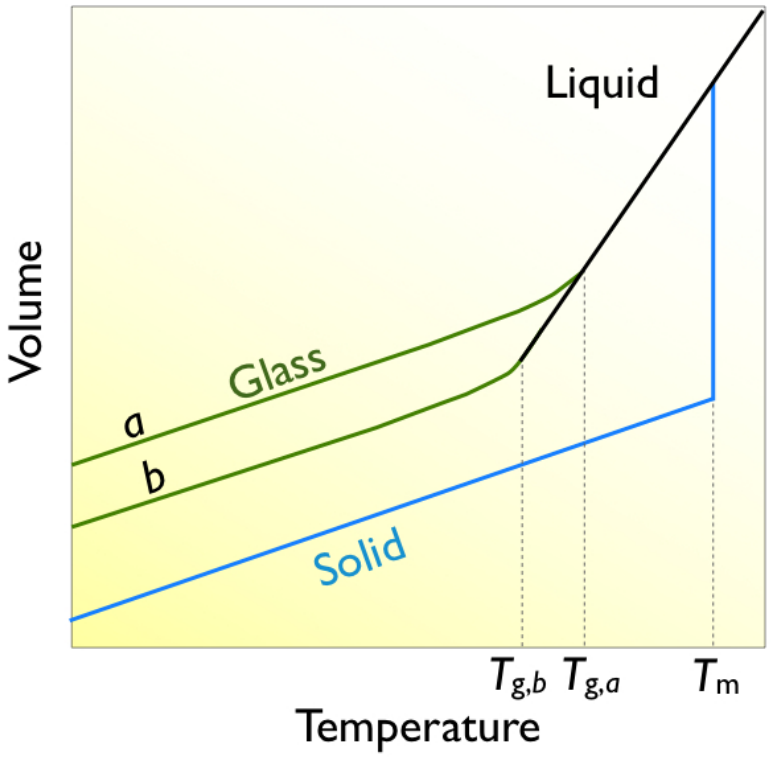

Figure 1.1: Schematic view of the glass transition. As a material is cooled through its melting temperature T_m it either freezes into a crystalline solid causing a sharp, discontinuous jump in the density, or it is supercooled. Eventually, when the supercooled liquid falls out of equilibrium, the system can no longer be further supercooled and arrests into a glass at a glass transition temperature, T_g. This temperature depends on the cooling rate. The a type glass shown in the diagram here is produced via a faster cooling rate and thus falls out of equilibrium sooner at $T_g = T_{g,a}$. Whereas glass b is cooled at a slower rate and has a glass transition temperature of $T_{g,b}$ which is less than $T_{g,a}$.

a later time t. The self-intermediate scattering function, $F_s(k,t)$ is defined as:

$$F_s(k,t) = \langle \exp[ik \cdot \Delta r(t)] \rangle \tag{1.1}$$

here, k is a wavevector and usually taken to be $k = 2\pi/\sigma$ where σ is the average distance between particles and $\Delta r(t)$ is the distance travelled by the particle in time t, and $i = \sqrt{-1}$. Where $\langle . \rangle$ indicates an ensemble average - here over all particles. This is equivalent to finding the k which first maximizes $F_s(k,0) = S(k)$ where $S(k)$ is the static structure factor.

For normal liquids, $F_s(k,t)$ is well characterized by a single decaying exponential function $F_s(k,t) = \exp(-t/\tau)$. Here τ is the structural relaxation time where $F_s(k,t) = 1/e$ [27]. Note, this relaxation time depends on the choice of wavevector k and therefore on a particular

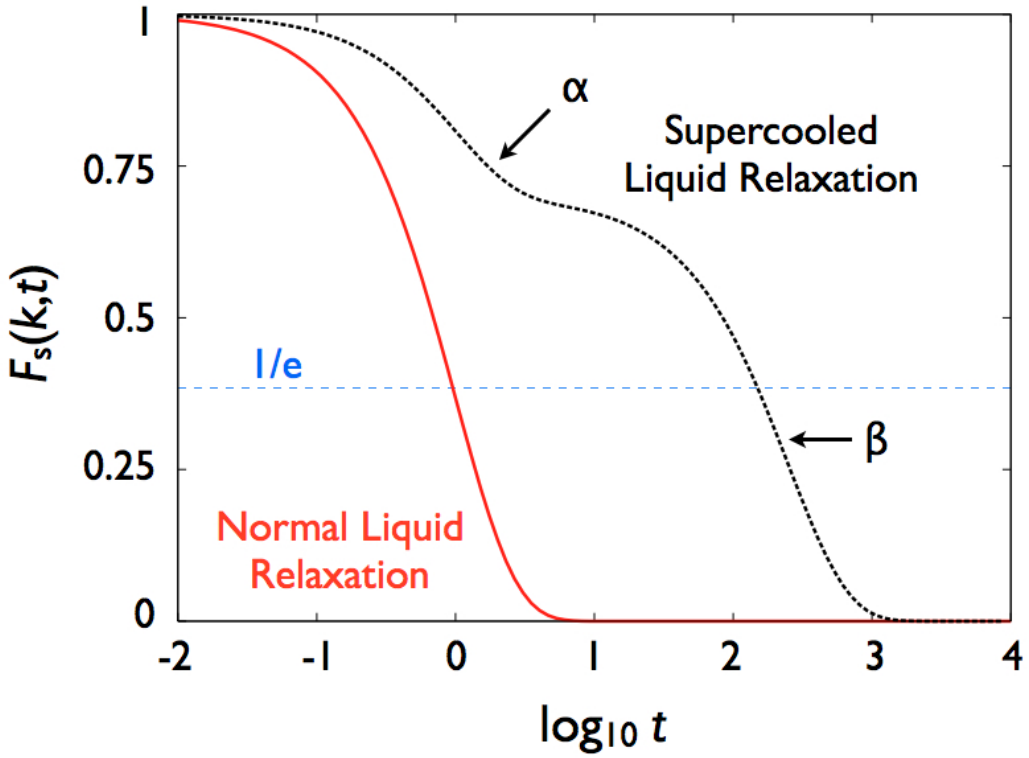

Figure 1.2: Illustration of typical relaxation behavior of the self-intermediate scattering function $F_s(k,t)$ as a function of t for a constant wavevector k for normal liquids and supercooled liquids. Red line indicates normal liquid behavior characterized by a single exponential decay. Black dashed line indicates typical behavior for a supercooled liquid. Labels show the portion of relaxation dominated by either the α or β relaxation processes described in Section 1.2.1. The blue dashed line indicates the $1/e$ line. The time point at which $F_s(k,t)$ intersects the $1/e$ line is typically taken to be the relaxation time, τ.

lengthscale, though, as noted before, k is often taken to be $2\pi/\sigma$. In supercooled liquids, however, the shape of the self-intermediate scattering function becomes stretched. The stretched portion of the scattering function takes on the form $F_s(k,t) = \exp\left[-(t/\tau)^\beta\right]$ where β is some stretching parameter less than 1. This stretching is often discussed in terms of two distinct processes in supercooled liquids: the α and the β processes. Here, the α process is the dominant, slow relaxation of the glass former whereas the β process is determined by the material and is usually thought to correspond to such processes as vibrations and side-chain relaxation in molecular glass formers. The stretching is one of the main phenomena associated with supercooled liquids [28], and the degree to which $\beta \neq 1$ is argued to be a signature of dynamic heterogeneity [24] introduced in Section 1.2.3.

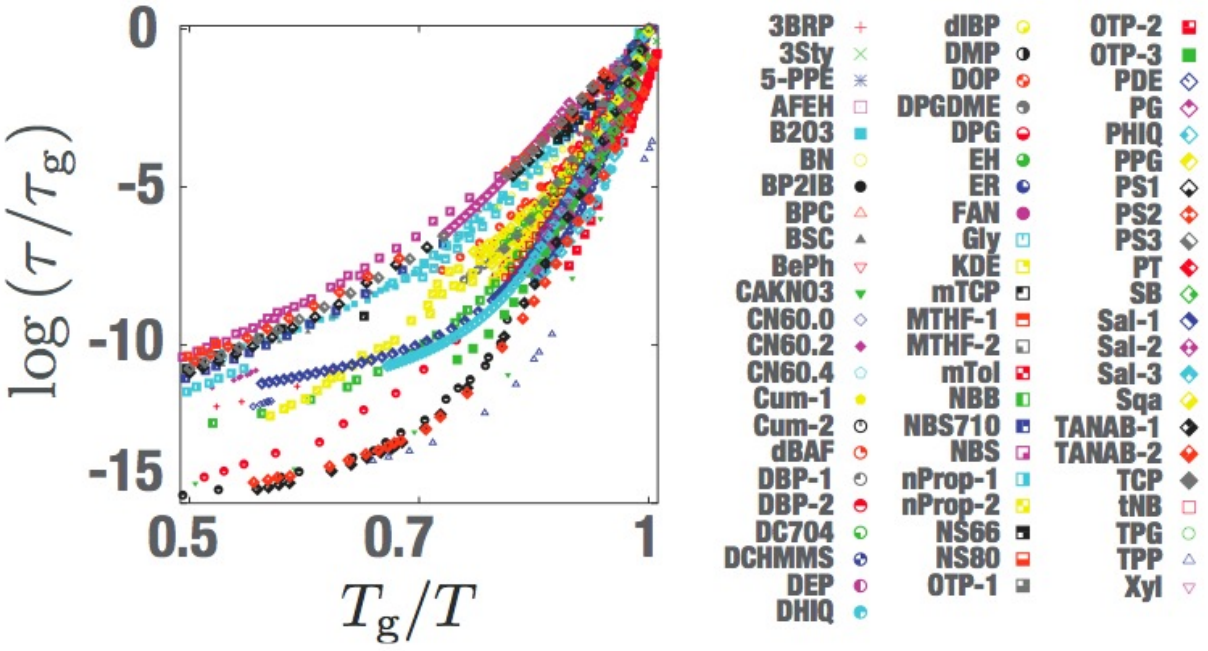

Figure 1.3: Angell plot showing relaxation time τ as a function of temperature T rescaled by the glass transition temperature T_g where $\tau_g = \tau(T_g) = 100$ seconds. Liquid abbreviations are the same as those considered in [1] and Table 2.1.

1.2.2 Stokes-Einstein Breakdown

The Stokes-Einstein relation relates the diffusion constant, D, to the microscopic relaxation time, τ [27]. It is a mean-field result which accounts for a tagged particle in a viscous medium [27, 29]. It is often written as:

$$D \propto \frac{T}{\tau} \tag{1.2}$$

here, T is temperature. The Stokes-Einstein equation implies that $D\tau/T$ is a constant. This relation is known to hold well for normal liquids, however in supercooled liquids it breaks down. In the supercooled regime, the diffusion constant and the relaxation time decouple [23]. Figure 1.4 shows this decoupling for the glass former tris-napthylbenzene (tNB). This suggests that the mean-field approximations within the Stokes-Einstein relation no longer hold in the supercooled regime as that region is known to be *dynamically heterogeneous* as will be introduced in the following section.

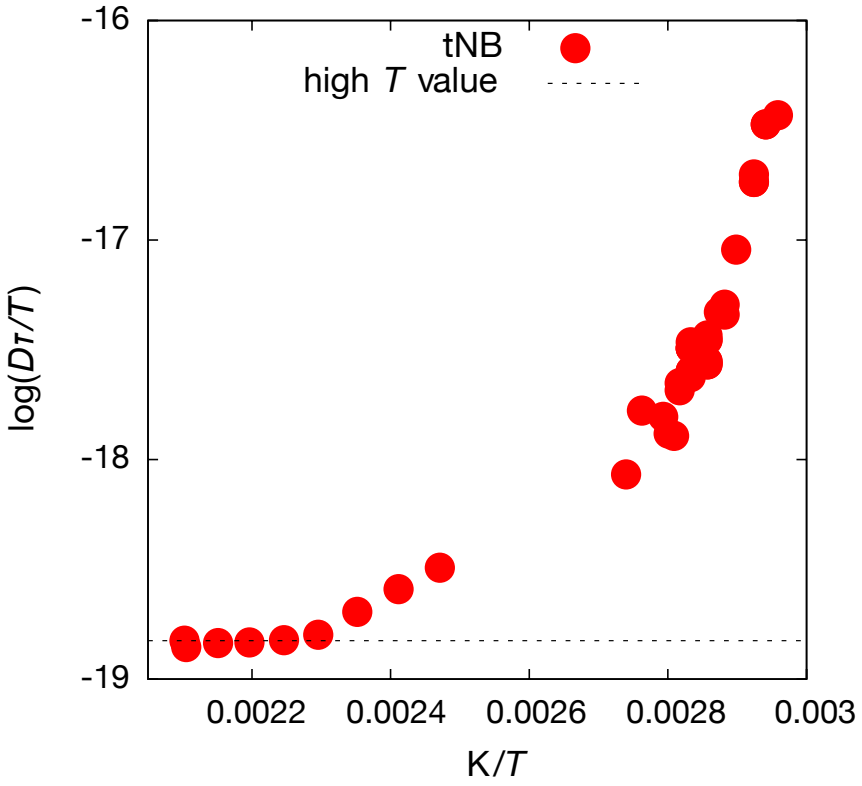

Figure 1.4: Decoupling between the diffusion constant, D, and the relaxation time, τ, as a function of temperature, T, for tris-naphthylbenzene [5]. Red dots indicate experimental data. Black dashed line indicates the high-temperature liquid regime where there is no decoupling and $D\tau/T$ is constant.

1.2.3 Dynamic Heterogeneity

While structural markers, such as the density pair-correlation function $g(r)$, vary little as a material is supercooled, recent works have shown that the dynamics of supercooled liquids are markedly different from that of normal liquids. Supercooled liquids are characterized by *dynamic heterogeneity* [30]. Dynamic heterogeneity is the property by which different spatial regions of glasses relax on different timescales.

In Figure 1.5 a schematic view of a 2D jammed material made of binary hard spheres is shown. In this illustration, particles which have moved a higher than average distance in an interval, Δt, are colored in red and are said to be very mobile. Particles that have moved a less than average amount in the same time interval are colored in blue and are called immobile. Particles with average mobility are shown in yellow. This characterization clusters particles into mobile regions and immobile regions. This illustration is indicative of the dynamic hetoeregeniety seen in various systems including granular materials [31], colloids

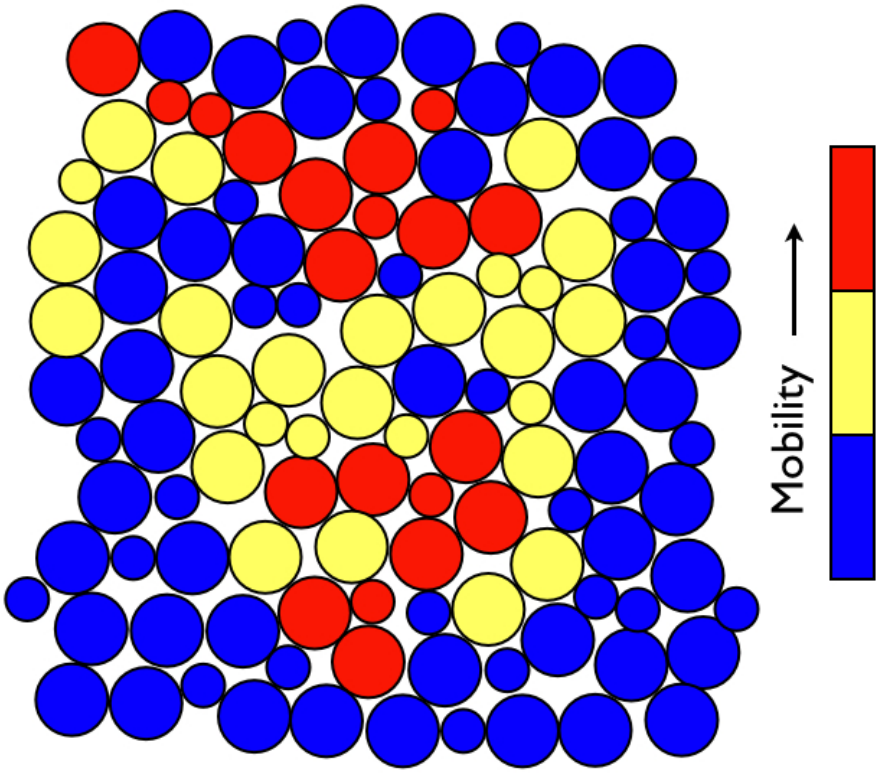

Figure 1.5: Illustration of a 2D jammed system. Particles are colored according to their displacements in a time interval, Δt. Particles which have moved most are colored red. Particles which have hardly moved are colored blue. Particles of average mobility are colored yellow.

[32], and simulations of Lennard-Jones particles [11].

1.2.4 The Kauzmann Temperature, T_{K}

At the freezing temperature T_{m} the entropy of a liquid is higher than the crystal with which it is in equilibrium. Moreover, the heat capacity of that liquid is also higher than the crystal. As a liquid is supercooled, the entropy of the supercooled liquid decreases more rapidly than that of the crystal. When extrapolated, these two entropies eventually cross at a non-zero temperature which is known as the Kauzmann Temperature, T_{K}. At T_{K} the supercooled liquid and the crystal have the same entropy. In the literature, the existence of this extrapolated crossing point is often referred to as the Kauzmann entropy crisis or Kauzmann entropy paradox [24]. Above T_{K} the entropy in excess of that of the crystal is

known as the configurational entropy, s_c, and in Section 1.3 I will introduce a theory related to the configurational entropy known as Adam-Gibbs theory. Of course, the kinetic process of the 'glass transition' at the temperature T_g intervenes at temperatures much higher than T_K and a supercooled liquid at T_K cannot be experimentally observed. A schematic diagram of the volume of a material undergoing a glass transition is shown in Figure 1.1.

One can determine the Kauzmann temperature through extrapolation of the difference in the intensive heat capacities of the liquid and the crystal, Δc_p at pressure p

$$\Delta s_m = \int_{T_K}^{T_m} \frac{\Delta c_p}{T} dT \tag{1.3}$$

here, Δs_m is the difference between the intensive entropy between the liquid and the crystal at the melting temperature.

1.2.5 Fragile and Strong Supercooled Liquids

Supercooled liquids also show a marked increase in the rate of change of their transport properties such as viscosity, η, and relaxation time, τ, as a function of inverse temperature, $1/T$ [1]. This is in contrast with the equilibrium liquid phase where there is little change in the relaxation time as a function of decreasing temperature. In general, two classes of supercooled liquids are considered: strong and fragile glass formers [6]. Strong glass formers include materials such as silica [6] - also known as window glass. Strong glass formers are characterized by *Arrhenius* relaxation, τ (or η) $\sim \exp(A\beta)$ where, A is an activation energy and $\beta = 1/k_B T$ [33]. Fragile materials are categorized by *super*-Arrhenius relaxation whose exact form has been much debated amongst experimentalists and theorists [34, 14, 35, 36]. In the coming section, some of the most popular modern theories regarding supercooled liquids will be introduced, along with their predictions for the scaling of the transport properties in supercooled liquids. Figure 1.6 demonstrates the two main types of scaling of transport properties in supercooled liquids. Figure 1.3 highlights the variety of 'fragilities' which can be found in fragile glass formers.

1.3 Theories of Supercooled Liquids and the Glass Transition

Many papers have been devoted to determining the underlying physics behind the glass transition. Here, I present several of the most widely considered of these theories. In the coming chapters, I will test the predictions of these theories in light of experimental data.

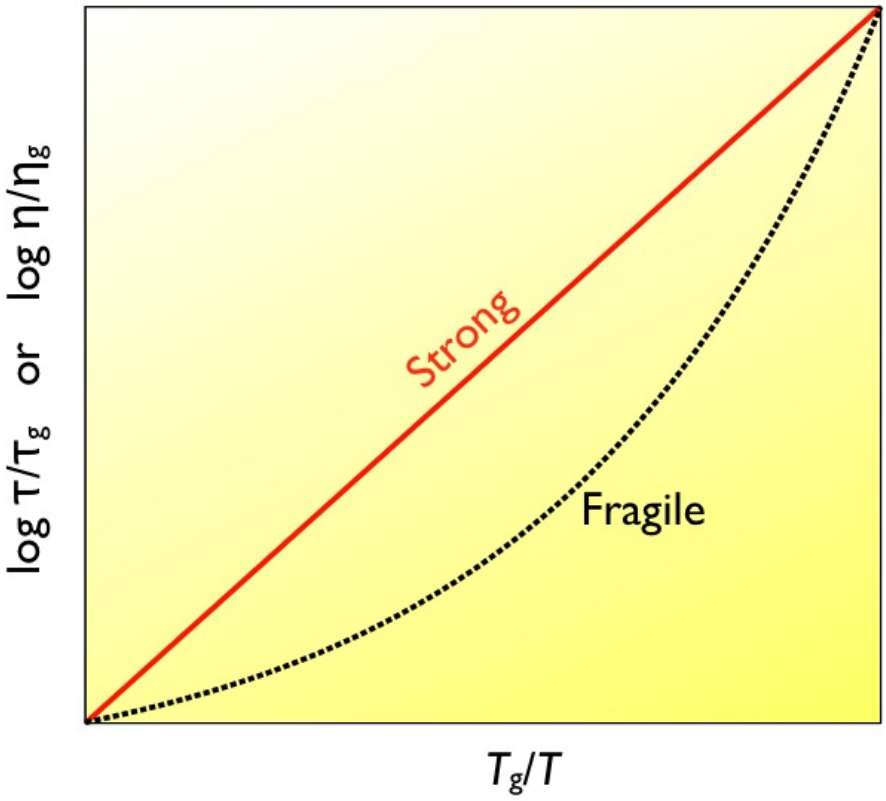

Figure 1.6: Schematic view of the logarithm of transport properties of supercooled liquids as functions of T_g/T. Here, T_g is the glass transition temperature where $\eta_g = 10^{13}$ poise or $\tau_g = 100$ seconds. Strong liquids such as silica [6] follow Arrhenius behavior where the relaxation time (τ) or viscosity (η) go as $\exp(A\beta)$ indicated by the solid, red line. Fragile materials, such as toluene and orthoterphenyl [1] follow a super-Arrhenius form as indicated by the black dashed line.

1.3.1 Mode Coupling Theory

Mode coupling theory (MCT) is a mean field theory for liquids at temperatures well above the glass transition temperature, T_g [34]. Thus, MCT is a good theory for normal liquid behavior approaching the supercooled regime. The basic idea of MCT (and also random first order theory) is to analyze the behavior of a free energy, F, which represents the configurational landscape of a material. However, it is not convenient to choose density as an order paramter to explore this landscape because the various amorphous minima are not distinguishable by density alone. Instead, MCT (and others) have tried to understand the behavior in terms of the entire density field of the system. Mode coupling theory seeks to derive an expression for the density fluctuations from basic equations of motion and begins

with the exact equation [37]:

$$\frac{d^2F(k,t)}{dt^2} + \frac{k^2 k_B T}{mS(k)}F(k,t) + \int_0^t d\tau M(k,\tau)\frac{d}{dt}F(k,t-\tau) = 0 \tag{1.4}$$

where $F(k,t)$ is the dynamic structure factor, $S(k) = F(k,0)$ is the static structure factor, m is the mass of a particle, T is temperature, k is a wavevector and $M(k,t)$ is a memory kernel. One can show that the memory kernel is related to the variance of the random forces on the density field [26]. Therefore, $M(k,t)$ captures the effects of other degrees which couple to the density field. Eq. 1.4, though exact, is impossible to solve directly and therefore MCT seeks to approximate this equation by identifying the slow, and therefore dominant, modes in the system. This allows MCT to derive dynamical equations – though this task is not trivial. This is done through a set of self-consistent MCT equations which are solved simultaneously (see Ref. [26, 37]).

In its idealized form, MCT predicts a transition at a mode coupling temperature, T_{MCT}, where the supercooled liquid goes through a transition from being in an ergodic phase to a non-ergodic phase. MCT predicts that for $T \leq T_{\mathrm{MCT}}$ correlation functions such as $F_s(k,t)$ for some wavevector k will never decay [34] and predicts that the relaxation time τ for temperatures above, but close to, T_{MCT} should go as:

$$\tau(T) \sim (T - T_{\mathrm{MCT}})^{-\gamma} \tag{1.5}$$

where γ is a positive exponent usually stated to be between 2 and 3 [34]. This power law scaling holds near the mode coupling temperature T_{MCT}. At the glass transition temperature, T_{MCT}, MCT predicts a divergence in the relaxation time τ [37]. MCT is successful at predicting much of the behavior of supercooled liquids including the scaling of the β and α relaxation processes [37]. However, it is well established that predictions of T_{MCT} tend to be greater than T_g. Since there is no divergence of τ in the supercooled regime, Eq. 1.5 cannot hold for $T_{\mathrm{MCT}} \geq T > T_g$ even though the material is still said to be in an ergodic, relaxing state. The fact that no divergence is observed at T_{MCT} has been one of the greatest challenges to pure MCT [37].

1.3.2 Adam-Gibbs Theory

Adam and Gibbs [38] formulated a theory of the glass transition based on the idea that there is a connection between thermodynamics and dynamics. They proposed that glasses become more and more viscous because they sample fewer and fewer basins as their energy is decreased via lowering temperature. Eventually, at the Kauzmann temperature, T_K, the material becomes "localized" in one ideal-glass minimum. This localization causes the configurational entropy, s_c, to vanish. The configurational entropy, s_c is related to the total number of basins the material can sample. Adam-Gibbs theory builds upon the idea of cooperatively rearranging regions (CCRs). CCRs are regions in a glass former which

can relax into another configuration, independent of the surrounding particles outside of that region [38]. The main Adam-Gibbs equation for the relaxation time τ as a function of temperature T is given by:

$$\tau = A \exp(B/Ts_c) \tag{1.6}$$

here, A and B are material dependent prefactors [24]. Adam-Gibbs theory has also been used to support the empirical findings of Vogel, Fulcher, and Tamman [36, 39, 40] that

$$\tau = A_{\mathrm{VFT}} \exp(B_{\mathrm{VFT}}/(T - T_{\mathrm{VFT}})) \tag{1.7}$$

where A_{VFT} and B_{VFT} are constant prefactors. This equation is commonly referred to as the VFT equation in honor of the scientists who originally noted its abilities to fit a wide range of experimental, supercooled liquid transport data. T_{VFT} is a temperature where there is a predicted divergence similar to that predicted by MCT at T_{MCT}. Unlike T_{MCT}, T_{VFT} is often fit to be significantly lower than T_g [13]. Moreover, many have correlated T_{VFT} with the expected divergence due to the entropy crisis at T_K. In fact, many go so far as to equate T_{VFT} and T_K [41].

1.3.3 Random First Order Theory

Random first order theory (RFOT) patches several popular supercooled liquid theories into one unified theory and suggests regimes in which each of these theories hold. RFOT, like Adam-Gibbs theory and MCT, still seeks to understand the underlying free energy landscape of density fields. To achieve this, RFOT combines ideas from Adam-Gibbs theory [42] as well as MCT. RFOT views MCT as a good description of supercooled liquid behavior up until the mode coupling temperature T_{MCT}. Here, at T_{MCT}, instead of observing a divergence in transport properties (or an infinite plateau in $F_s(k,t)$), the transition is said to be avoided and instead a crossover is observed. The MCT temperature is interpreted as a location at which the change is purely dynamical, rather than thermodynamic. Beyond this initial MCT regime but above the Kauzman temperature $T_K < T < T_{\mathrm{MCT}}$, the material transitions into a "mosaic state" – borrowing the cooperatively rearranging regions of Adam-Gibbs theory. Here, the liquid is made of a mosaic of domains of width approximately ξ. The interpretation is beyond this length scale, metastable states are no longer well defined [26].

Like Adam-Gibbs theory, RFOT predicts that the relaxation time τ goes as Eq. 1.7 beyond the mode-coupling regime where mean field theories breakdown. Further, like Adam-Gibbs theory, there is a great importance placed on the configurational entropy in the supercooled liquid. However, unlike Adam-Gibbs theory, RFOT predicts a size for these cooperatively rearranging regions (motivated by experiment) and estimates them to be about the size of 100-200 molecules near the glass transition at T_g. Moreover, instead of being dense and packed regions, RFOT purports that these cooperatively rearranging regions are amorphous and fractal-like [42]. In RFOT there is a predicted thermodynamic transition and 'spinodal decomposition' at a temperature T_{RFOT} which is higher than T_g. This corresponds

to a transition between activated motion and glassy dynamics. The theory suggests, therefore, that there is a first order phase transition near T_g and that the dynamic heterogeneities correspond to a nucleation process [42].

1.3.4 Other Empirical Fits to Transport Properties

Like the VFT fit, other fits have been proposed to fit supercooled liquid transport data. One popular fit is the double exponential fit [14, 43]

$$\log(\tau/\tau_{\rm dx}^{(\infty)}) = (K/T)\exp(C/T) \tag{1.8}$$

where K, C, and $\tau_{\rm dx}^{(\infty)}$ are fitting constants. Unlike other forms, the double exponential form predicts no divergence in relaxation time. Yet another proposed fit has been suggested for polymeric glass formers and has a fractional exponential [44] form

$$\log(\tau/\tau_{\rm c}) = X(T_{\rm c}/T-1)^{1.57} \tag{1.9}$$

where X, $T_{\rm c}$, and $\tau_{\rm c}$ are fit parameters. The fractional exponential form predicts a divergence at $T_{\rm c}$.

1.3.5 Chandler-Garrahan Theory

Chandler-Garrahan theory is based on dynamical facilitation [35, 45]. Dynamic facilitation is the idea that relaxation propagates through a supercooled liquid and is clustered in space and time. More specifically, dynamic facilitation implies that regions of a glass formers cannot relax until a nearby "excitation" passes through them. The main predictions of Chandler-Garrahan theory are captured by a set of kinetically constrained models (KCMs) which have facilitation built into them via dynamical constraints.

Basic KCMs

The two most basic KCMs are the one dimensional east model and the one dimensional Fredrickson-Andersen (FA) model. In both models, the underlying thermodynamics is that of a lattice gas [25]. The one dimensional lattice gas is a model with N sites labeled $i = 1, 2, \cdots, N$. Each lattice site can take on one of two values $n_i = \{0, 1\}$. In the context of Chandler-Garrahan theory, the interpretation is that at site i where $n_i = 0$, the glass former is in an unexcited state and cannot facilitate neighboring regions to relax. A region which contains an excitation, where $n_i = 1$, can facilitate neighboring regions to relax. Lattice sites do not interact energetically. The total energy, E, of the system is therefore given by the sum of the lattice occupancy

$$E = \sum_{i=1}^{N} n_i \tag{1.10}$$

The equilibrium concentration $c = \langle n_i \rangle$ of these excitations at inverse temperature $\beta = 1/k_{\mathrm{B}}T$ is given by:

$$c = \langle n_i \rangle = \frac{1}{1 + e^{\beta}}. \tag{1.11}$$

The east and the FA models are distinguished from the lattice gas model by their dynamical rules. For unconstrained dynamics, at some time t any site can change state with some finite rate [25] proportional to the detailed balance condition

$$\frac{k_{0\to1}}{k_{1\to0}} = e^{-\beta} \tag{1.12}$$

here, $k_{0\to1}$ is the rate a site into $n_i = 0$ becomes excited where $n_i = 1$. $k_{1\to0}$ is the reverse process where n_i goes from an excited state to an unexcited state where $n_i = 0$. For an unconstrained process, we can take $k_{0\to1} = e^{-\beta}$ and $k_{1\to0} = 1$, though, as we will see in the FA and east models, any rates which preserve the ratio in Eq. 1.12 are acceptable rate choices.

Unlike for unconstrained dynamics, in KCMs only some sites are capable of changing states at time t. These rules therefore take into account the ideas of facilitation.

FA Model

The FA model [46] is a model for a strong glass former and thus has Arrhenius relaxation scaling as discussed in Section 1.2.5 [47]. In the FA model, sites where $n_i = 1$ can facilitate relaxation in either adjacent lattice site n_{i-1} or n_{i+1}. This introduces a *constraint* function C_i into the rate expressions. For the FA model the constraint function is:

$$C_{i,\mathrm{FA}} = n_{i+1} + n_{i-1} \tag{1.13}$$

and the rate expressions become:

$$k_{0\to1} = e^{-\beta} C_{i,\mathrm{FA}} \tag{1.14}$$

$$k_{1\to0} = C_{i,\mathrm{FA}}. \tag{1.15}$$

Since the detailed balance condition in Eq. 1.12 is preserved, the thermodynamics are unchanged. The difference is entirely *dynamical*. A schematic view of facilitation in the FA model is given in Figure 1.7. A sample trajectory for the FA model for some observation time, t_{obs}, is shown in Figure 1.8. Relaxation in the FA Model is said to be 'diffusive' as there is only one characteristic barrier relaxation – the Arrhenius barrier [35].

East Model

The east model [48] is similar to the FA model except that the constraint function only contains a term in one direction. Sites facilitate their neighbors to their "east." C_i becomes

$$C_{i,\mathrm{east}} = n_{i-1}. \tag{1.16}$$

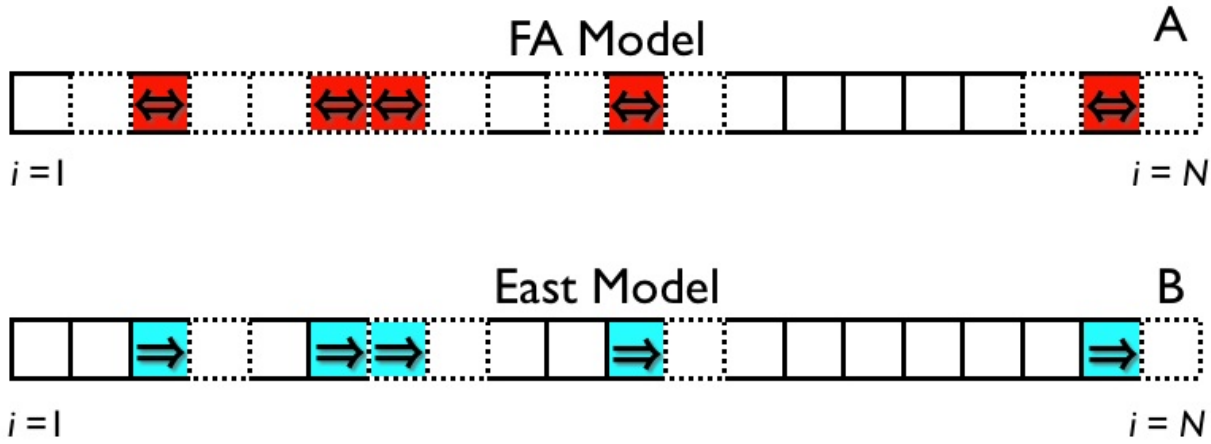

Figure 1.7: Schematic view of constraints in the 1-dimensional east and FA model. Panel (A) shows a configuration of the FA model at some time t where lattice sites are labeled from $i = 1$ to N where $N = 20$. Double arrows in filled, red sites indicate excitations where $n_i = 1$ as well as direction of facilitation. Sites containing no arrows indicate places where $n_i = 0$. Unfilled sites outlined in dashed lines indicate regions where $C_{i,\mathrm{FA}} \neq 0$, and can change state in the next time $t + \delta t$ where δt is an infinitesimal time step. Panel (B) shows a configuration of the east model at some time t where lattice sites are labeled from $i = 1$ to N where $N = 20$. Right pointing arrows in filled, blue sites indicate excitations where $n_i = 1$ as well as eastward direction of facilitation. Unfilled sites containing no arrows indicate places where $n_i = 0$. Sites outlined in dashed lines indicate regions where $C_{i,\mathrm{east}} \neq 0$, and can change state in the next time $t + \delta t$ where δt is some infinitesimal time step.

The rates in the east model are

$$k_{0\to 1} = e^{-\beta} C_{i,\mathrm{east}} \tag{1.17}$$

$$k_{1\to 0} = C_{i,\mathrm{east}}. \tag{1.18}$$

The east model relaxes hierarchically – that is to say that there is no single characteristic barrier because the barriers are a function of distance between sites ℓ [35]. The east model is a good model for fragile dynamics [47]. Again, like the FA model, the difference between the east model and an unconstrained model is purely dynamical; the thermodynamics remains unchanged. A schematic view of facilitation in the east model is given in Figure 1.7 and an example trajectory for some observation time, t_{obs}, is shown in Figure 1.9.

Crossover Model

Most glass formers' behavior falls in between that of the east and the FA model. To interpolate between these two extremes, Garrahan and Chandler consider the the crossover

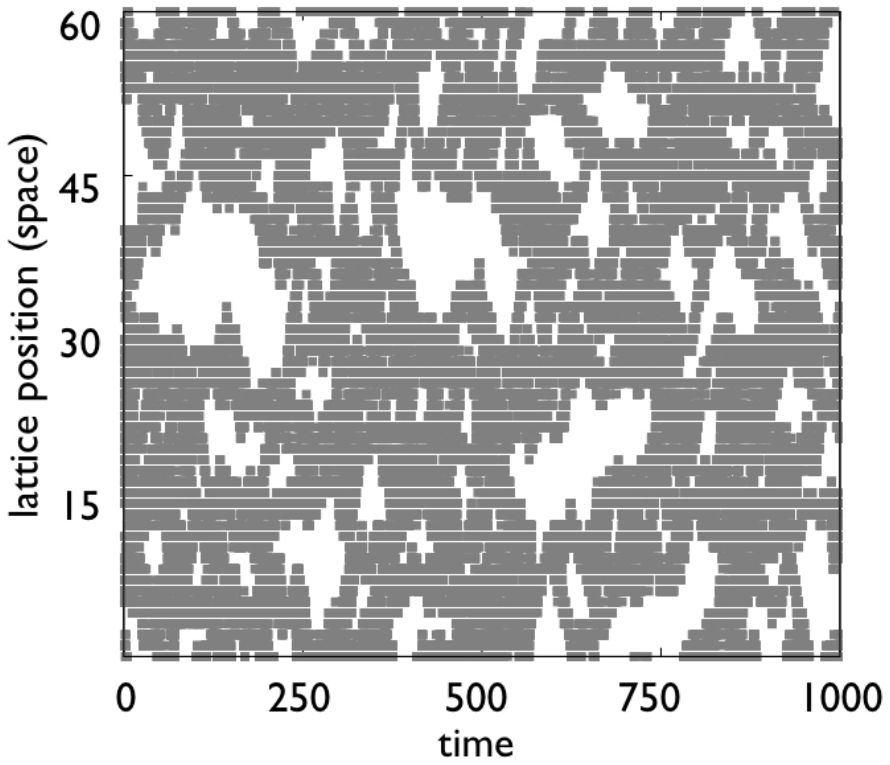

Figure 1.8: Sample FA model trajectory for $\beta = 1$, $N = 60$ and $t_{\rm obs} = 1000$ Monte Carlo cycles. Grey squares indicate places in space-time where $n_i(t) = 1$. White areas indicate places in space-time where $n_i(t) = 0$.

model [35] as a reference model for glass formers. The crossover model is an interpolation between the east and FA models [49]. Here, the constraint function $C_{i,\mathrm{x}}$ is:

$$C_{i,\mathrm{x}} = \varepsilon n_{i+1} + n_{i-1} \tag{1.19}$$

where ε is an interpolating parameter that ranges from 0 to 1. $\varepsilon = 0$ returns the east model. $\varepsilon = 1$ returns the FA model. For the crossover model the rates become

$$k_{0\to 1} = e^{-\beta} C_{i,\mathrm{x}} \tag{1.20}$$

$$k_{1\to 0} = C_{i,\mathrm{x}} \tag{1.21}$$

Chandler-Garrahan Theory

In KCMs (and atomistic systems [50]) for the length scale a which is not much larger than the size of a particle diameter Chandler and Garrahan define an excitation which is

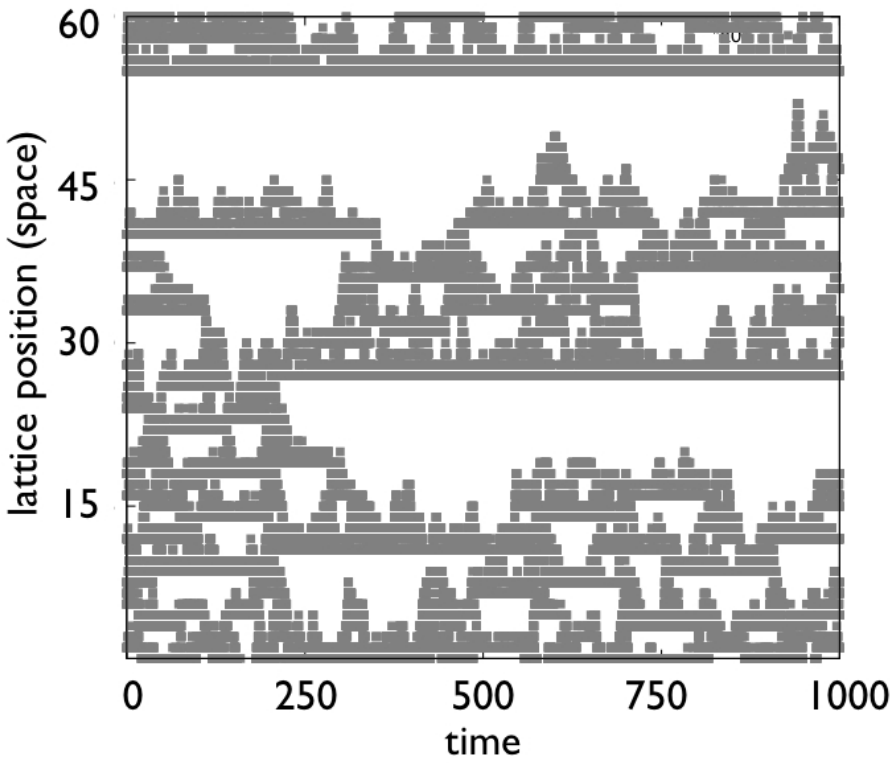

Figure 1.9: Sample east model trajectory for $\beta = 1$, $N = 60$ and $t_{\rm obs} = 1000$ Monte Carlo cycles. Grey squares indicate places in space-time where $n_i(t) = 1$. White areas indicate places in space-time where $n_i(t) = 0$.

an irreversible particle displacement of size a. The concentration of such excitations on the length scale a in a supercooled liquid goes as an ideal gas of uncorrelated excitations

$$c_a \propto \exp[-J_a(1/T - 1/T_{\rm o})], \quad T < T_{\rm o} \tag{1.22}$$

here, J_a is an energy barrier to produce the excitation of size a. And $(1/T - 1/T_{\rm o})$ is a reduced temperature defined for temperatures below an onset temperature $T_{\rm o}$ to supercooled behavior. Based on hierarchical KCMs, they argue that J_a has a weak length scale dependence and grows logarithmically with the size of the excitation

$$(J_a - J_{a'})/J_{a'} = \gamma \ln(a/a') \tag{1.23}$$

where γ is material dependent and near unity and a' is some other length scale. For some distance between elementary excitations, ℓ_a, the relaxation time τ goes as:

$$\tau/\tau_a \sim e^{F\ell_a/k_{\rm B}T} \tag{1.24}$$

where T is temperature, k_{B} is Boltzmann's constant, τ_a is a proportionality constant, and F_a is a free energetic barrier corresponding to the length scale, ℓ_a. Chandler-Garrahan theory predicts that glassy relaxation includes a weak length scale dependence (Eq. 1.23) such that,

$$\tau/\tau_a \sim e^{F_{\mathrm{o}}/k_{\mathrm{B}}T+[1/T-1/T_{\mathrm{o}}]J_a\gamma \ln \ell_a/a}, \quad T < T_{\mathrm{o}} \tag{1.25}$$

where F_{o} is the free energetic barrier lacking length scale dependence and $J_a \ln \ell$ is the length scale dependent perturbation to that free energy below T_{o} where J_a is an energetic barrier in units of k_{B}^{-1}.

The distance between excitations of size a, ℓ_a depends on the concentration of excitations, c. For kinetically constrained models these excitations are independent from one another and the concentration therefore goes as

$$\ell_a/a \sim c_a^{-1/d}/a \sim (\exp[-J_a(1/T - 1/T_{\mathrm{o}})])^{-1/d} \tag{1.26}$$

here, c_a is the concentration of excitations of at least size a and d is the fractal dimensionality [50]. The proportionality $\ln c_a \sim [-J_a(1/T - 1/T_{\mathrm{o}})]$ is a result from the analytical treatment of KCMs [35]. Combining Eq. 1.26 and Eq. 1.25 we find

$$\log \tau/\tau_{\mathrm{o}} = \left(\frac{J}{T_{\mathrm{o}}}\right)^2 \left(\frac{T_{\mathrm{o}}}{T} - 1\right)^2 \tag{1.27}$$

where $J = \sqrt{J_{\mathrm{a}}^2\gamma/d}$ and $\log \tau_{\mathrm{o}}$ is the relaxation time of the material at T_{o} (and has observed all constant prefactors). This is known as the parabolic fit or, alternatively, in recent literature as the Elmatad-Chandler-Garrahan (ECG) fit [51]. Here, T_{o} is the onset to supercooled liquid behavior where this form begins to hold and J is an energetic barrier. The values of these parameters are material dependent. Unlike MCT, Adam-Gibbs theory, RFOT, or the VFT equation, the parabolic form of Eq. 1.27 predicts no divergence in τ at a metaphysical temperature. Moreover, the parabolic fit holds for all points where $T_{\mathrm{g}} \leq T \leq T_{\mathrm{o}}$.

Fragile-to-Strong Crossover

Chandler-Garrahan theory makes a further prediction that at some temperature $T_{\mathrm{x}} < T_{\mathrm{o}}$ the behavior of so-called "fragile" glass formers (those whose relaxation time follow a super-Arrhenius form of Eq. 1.27) should cross over to the behavior of "strong" glass formers. For strong glass formers the relaxation time follows a simple Arrhenius form, $\tau \sim \exp(-\beta A)$ where A is an activation energy. Chandler-Garrahan theory suggests that this is a crossover between hierarchical relaxation in fragile glass formers to diffusive relaxation in strong glass formers. This is because hierarchical barriers grow as $1/T^2$ whereas diffusive barriers grow as $1/T$. Eventually, hierarchical barriers will become too energetically expensive and the system will switch to relaxing diffusively. This is confirmed in simulations of the crossover model with various values of ε [49].

Chapter 2

Supercooled Liquid Universality

2.1 Introduction

In Chapter 1 several common theories of the glass transition were presented as well as their predictions for the temperature dependence of transport properties such as viscosity η and relaxation time τ. Where η and τ are interchangeable as they are related to one another by

$$\eta = G^{\infty}\tau \tag{2.1}$$

where G^{∞} is the instantaneous shear modulus [52] and is a constant that varies little with changes of temperature. In this chapter, I will study the experimental temperature dependence of transport properties.

While in irreversible or driven cases, transport properties can be singular [53, 20]. Here, I will restrict myself to "equilibrium" relaxation time data in the region between liquid behavior at high temperature and the glass transition temperature T_{g} where the system falls out of equilibrium and into the glass state. This data is in "equilibrium" in the sense that the sample has been cooled and warmed sufficiently slowly such that the process is reversible.

The most commonly used form in the literature is that of Vogel, Fulcher, and Tammann (VFT) [36, 39, 40]. The VFT form is an empirical fit to supercooled transport data and is often written as:

$$\tau = A_{\mathrm{VFT}} \exp(B_{\mathrm{VFT}}/(T - T_{\mathrm{VFT}})) \tag{2.2}$$

where A_{VFT}, B_{VFT} and T_{VFT} are fitting constants. The VFT form predicts a singularity at T_{VFT} where τ becomes infinite and the material can no longer relax. In practice, experimentally $T_{\mathrm{VFT}} < T_{\mathrm{g}}$ such that T_{VFT} is a metaphysical temperature which can not be verified. The VFT form is not the only form which predicts a singularity. Another popular form is the Mode Coupling Equation

$$\tau(T) \sim (T - T_{\mathrm{MCT}})^{-\gamma} \tag{2.3}$$

where the divergence is at the mode coupling temperature T_{MCT}. T_{MCT} is usual predicted to be higher than T_{g} despite no apparent divergence as T approaches T_{MCT}.

Recently, however, many have begun to question whether or not transport properties should be fit with singular functions. In a recent work by Hecksher et al [54] they find no compelling evidence for fitting with a singular function as compared with a form that goes as $\log \tau \sim B/T^n$ where B and n are fitting parameters. Moreover, in their work they found that for most supercooled liquids $n \approx 2$. Using this form, they found that they could fit supercooled liquid transport properties as well as the VFT form thus suggesting that there was no compelling evidence for fitting with a singular function over a continuous function. In their study, they considered supercooled liquid transport properties for over 40 liquids, all of which are also considered here.

Unlike these popular theories, Chandler-Garrahan [35] predicts no such divergence and instead predicts the parabolic form

$$\log \tau/\tau_{\rm o} = \left(\frac{J}{T_{\rm o}}\right)^2 \left(\frac{T_{\rm o}}{T} - 1\right)^2 \tag{2.4}$$

where J, $T_{\rm o}$, and $\log \tau_{\rm o}$ are fit parameters. This fit is motivated by Garrahan-Chandler theory as derived at the end of Chapter 1 [35]. In the following sections we will apply this form to over 58 distinct structural glass-forming liquids and find that this form is capable of collapsing all fragile glass former data onto one, single curve [1].

We expect the range of validity of this quadratic behavior to be bounded [55]. In particular, it should not apply above a temperature $T_{\rm o}$ where excitations facilitating molecular motions are present throughout the system. In that regime, correlated dynamics is not required for molecular motions, and accordingly, temperature variation of transport is nearly negligible [56, 57]. The quadratic form should also not apply below another temperature, which I call $T_{\rm x}$. The reasoning here recognizes that correlated dynamics leading to super-Arrhenius behavior [58] is the result of constraints due to intermolecular forces. At an energetic cost, E, these constraints can be avoided. The time scale to pay that cost is $\tau_{\rm x} \exp(E/T)$. While this time can be very long, at a low enough temperature it will become shorter than a super-Arrhenius time. This is the temperature $T_{\rm x}$, below which relaxation will be dominated by dynamics that avoid hierarchical constraints.

2.2 Fitting Procedure

Here, I summarize the procedure I employ to fit data with the parabolic form.

- First, I collect relaxation time or viscosity data spanning several orders of magnitude.
- Next, I examine the data to attempt to identify normal liquid and fragile regimes, and thereby obtain an approximate location of the onset lying between the two.
- Then, I fit the data spanning several orders of magnitude starting with the lowest temperatures available, using a least squares analysis to obtain a first estimate of J,

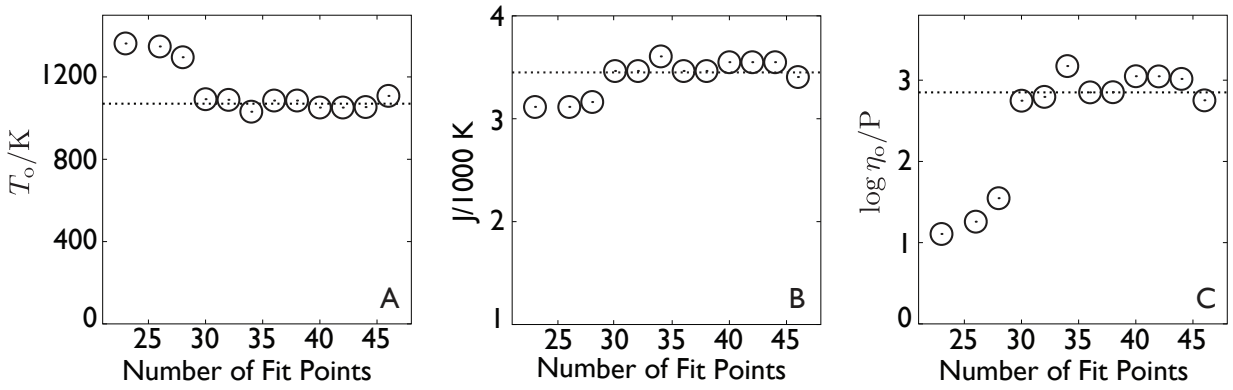

Figure 2.1: An example of fitting parameter convergence for B_2O_3. In the fragile regime, 47 data points ranging continuously over 11 orders of magnitude in η are available for fitting. Including the liquid regime, there are 62 data points in this set spanning 13 orders of magnitude in η. Initially, only the lowest temperature points are considered and subsequent fits with more points come from adding higher temperature points to the considered set. (A) shows the convergence of T_o as a function of number of points used for fitting. (B) shows the convergence of J as a function of number of points used for fitting. (C) shows the convergence of η_o (analogous to τ_o) as a function of number of points used for fitting. For this system, T_o is 1066 K, J/T_o is 3.3, and $\log \eta_o$ is 2.9 Poise.

T_o and $\log \tau_o$. I begin with the lowest temperature data points because the highest temperature points often have significant "mixing" with the liquid regime - where transport properties have little temperature dependence - and deconvoluting these two behaviors near the onset temperature is difficult. Moreover, including only the lowest temperatures ensures that you are almost certainly fitting in a regime where $T < T_o$.

- With this estimate for T_o as an indication of the highest temperature point for which to fit, I continue to add higher temperature points until the values of J, T_o and $\log \tau_o$ converge. (An illustration of the minimal amount of data needed to fit viscosity data for B_2O_3 [15] is shown in Figure 2.2. An illustration of the parameter convergence for the B_2O_3 fit is shown in Figure 2.1.) As points are added after convegence, it is not uncommon to see very small, but systematic changes in the parameters. Generally, J and T_o tend to rise together where as $\log \eta_o$ will decrease and vice versa. This may be due to the nature of the large number of degrees of freedom and the presence of local minima in fits of nearly equal standard deviation that swap from being local to global as certain data points are added. However, these changes are barely perceivable and only highlight that experimental data contains some error and it must be understood that fits with large degrees of freedom cannot, therefore, be perfect.

Caveat:

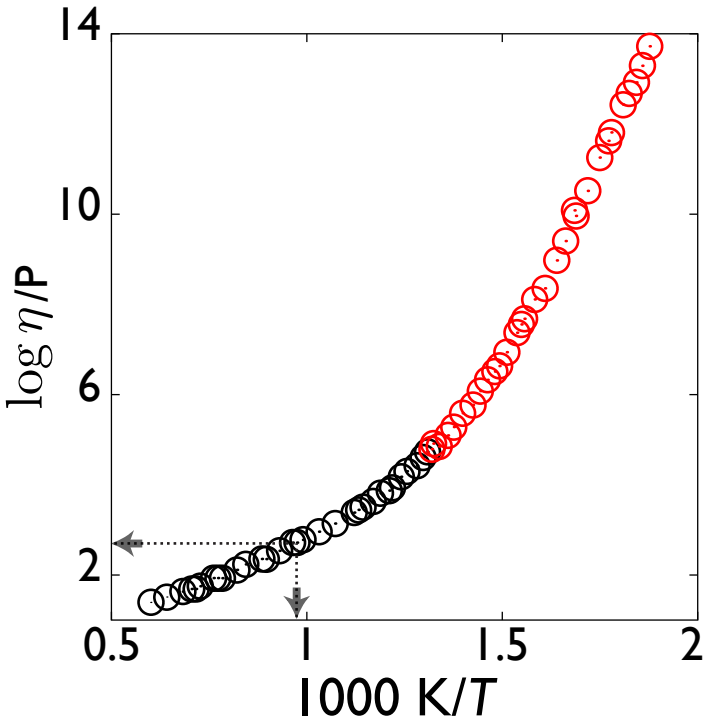

Figure 2.2: An example of fitting parameter convergence for B_2O_3. Red points indicate the minimal data set required to converge fitting parameters when beginning from the low temperature data and extrapolating downward. Dashed lines are guides to the eye to indicate the location of the onset of fragile behavior.

While in my B_2O_3 example I have chosen to start at the lowest temperature point and add higher and higher temperature points until the parameters converge, it should be noted that often the lowest temperature points are the hardest to measure and therefore sometimes data in this region is not always as reliable as data taken from a more moderate, yet still supercooled regime. It may be useful to check if a fit through such a moderate range properly predicts the lowest temperature data as an estimate for the quality of the lowest temperature data.

2.3 Fitting Experimental Data

In Figure 2.3 I demonstrate a universal collapse for over 68 data sets representing more than 1200 data points. A similar collapse was noted a few years ago, when Rössler and co-workers showed how seemingly varied behaviors for the transport properties of several supercooled liquids could be represented by a single function of temperature [43]. The fitting in Figure 2.3 differs mainly in the functional form adopted for the data collapse. This

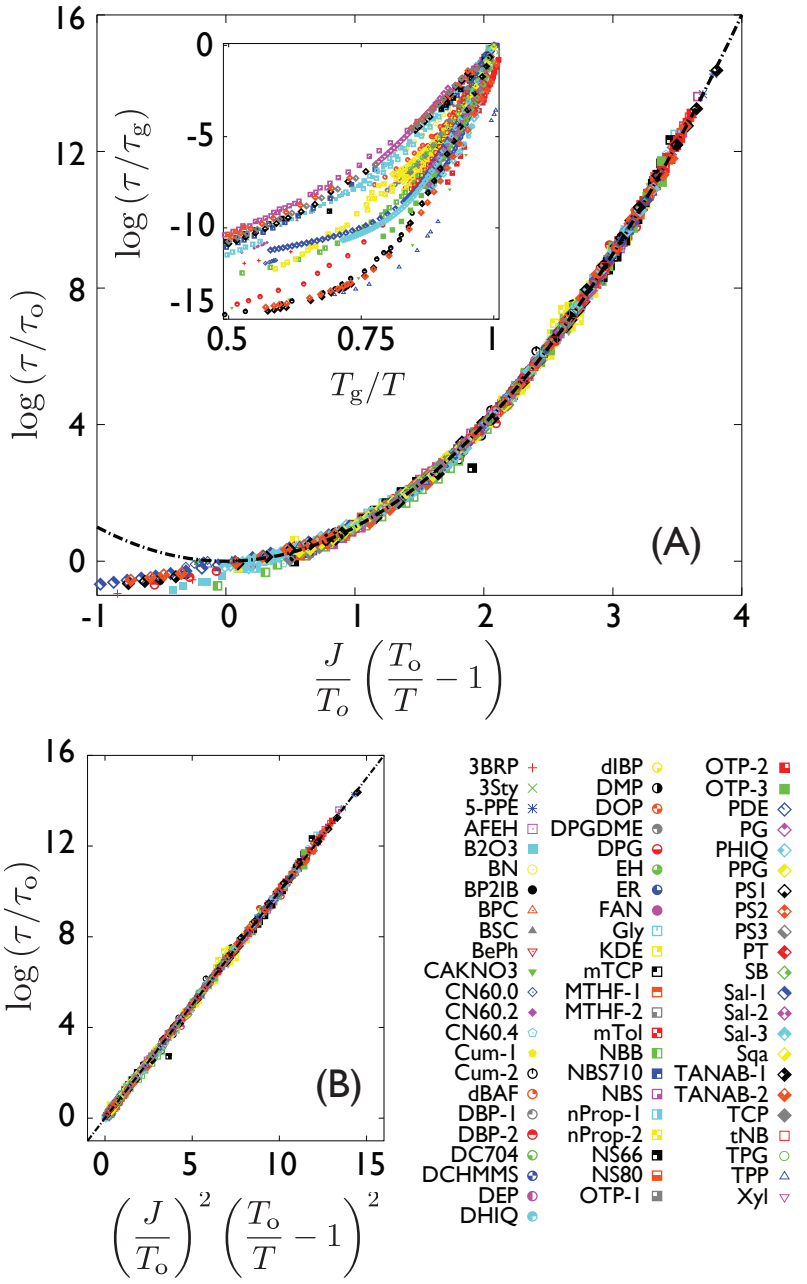

Figure 2.3: (A) Collapse to a parabolic form of the structural relaxation times, τ, and viscosities, η, as functions of temperature T for fragile glass forming liquids. Parameters τ_o, T_o and J are listed in Table 2.1. Inset shows the same data when graphed in Angell-type plots, where T_g refers to the temperature at which the viscosity of the liquid is 10^{13} Poise or when the relaxation time reaches 10^2 seconds. (B) Data for temperatures $T < T_o$ graphed as a function of the square of the collapse variable. Key at right lists the 68 liquid data sets considered in the graphs. The meaning of each acronym is given in Table 2.1.

difference enables a universal fit over a range of temperatures larger than the fit suggested by Rössler [43]. For example, for liquid Ca-K-NO_3, Rossler et al fit data for temperatures below $T = 381$ K, while T_o for this material is 444 K. This percentage difference is similar for all the liquids considered by Rossler et al. The onset-like temperatures for the fits reported by Fischer [59] and by Sticklel et al [60] are somewhat closer to T_o than that of Rossler et al, but here too, the boundaries for fitted data are lower than T_o. Kivelson and co-workers [61, 62] have proposed another collapse to a non-singular function, but one with one more adjustable parameter than I consider.

Table 2.1 collects the parameters obtained in the fitting data to Eq. 2.4 with $T_o > T > T_x$. For each liquid considered, the data set for this regime contained five or more data points, and most contained ten or more data points. This is the data shown in Figure 2.3. Some of the data refer to viscosity measurements, others refer to relaxation time measurements. For each liquid, the three fitting parameters are determined by minimizing the mean square deviation, σ^2, between the data and the quadratic form for temperatures that exceed a preliminary estimate of the onset temperature. The standard deviations obtained by this fitting are noted in Table 2.1.

The reference time, τ_o, is the time for relaxing a microscopic region of liquid at the onset temperature. We expect these times to be no smaller than 1 ps. Similarly, I expect the reference viscosity, η_o, to be not much smaller than 1 Poise. A much smaller value can be an indication of treating a strong material as if it were fragile. For example, fitting available data for liquid 3-phenyl-1-propanol (3Ph1P) [54, 63, 64] with Eq. 2.4 yields a seemingly acceptable standard deviation of $\sigma = 0.16$, but the energy scale compared to the reference temperature is curiously low, $J/T_o \approx 1.2$, and the reference time is unreasonably short, $\tau_o \approx 10^{-16}$ s. Instead, by fitting to the Arrhenius form with $\log(\tau_R/\mathrm{s}) = -2.4$ at $T = T_R = 200$K, the activation energy E and standard deviation σ have reasonable values of $40T_R$ and 0.57, respectively. Another similar case is the liquid triphenyl-ethylene (TPE) [65]. Again, while the standard deviation $\sigma = 0.0086$ is small, the time is unreasonably short, $\tau_o \approx 10^{-14}$ s. An Arrhenius fit for these data yields $\log(\tau_R/\mathrm{s}) = -3.1$, $T_R = 274$K, $E/T_R = 58$ and $\sigma = 0.058$. The available data therefore suggests that these supercooled liquids are strong. That is, the crossover temperature is larger than any temperature for which the data is available: $T_x > T_R$. Perhaps for these liquids, or others like them, relaxation could be studied at higher temperatures to find evidence for a crossover temperature.

There is one outlying data point on the graphs of Figure 2.3 for so called NS 66 [66]. This occurs at a state point far separated from all the other state points for which other data points exist. We suspect this point might be erroneous.

2.4 Fitting Numerical Data

Figure 2.4 shows quadratic data collapse for data from six numerical simulations of fragile glassfomers. Here, the fitting was done using the same methods used to collapse the data

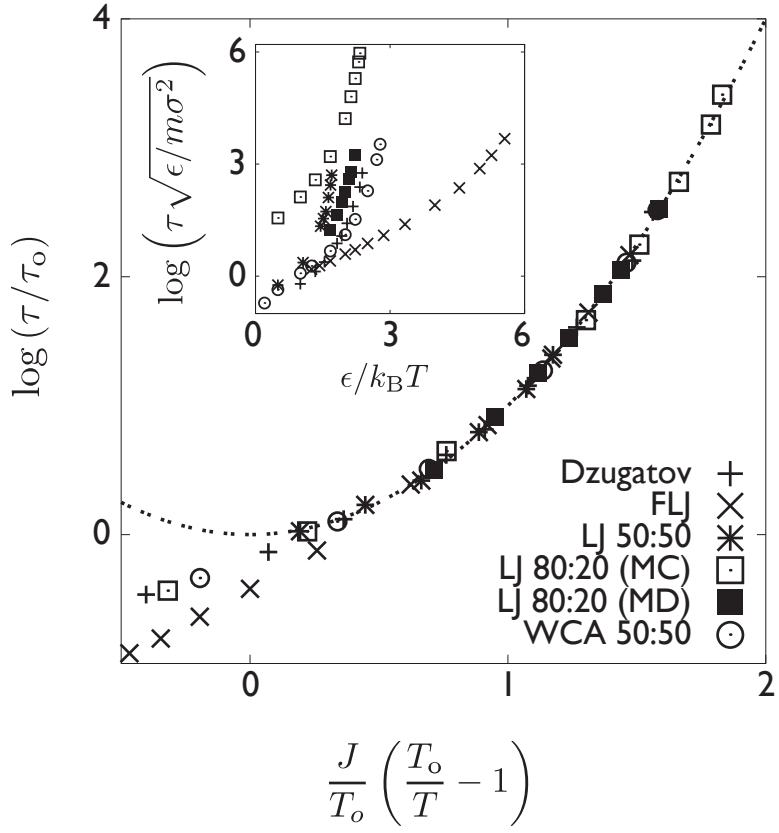

Figure 2.4: Collapse to a parabolic form of the structural relaxation times, τ, as functions of temperature T for simulations of models of fragile glass forming liquids. Parameters τ_o, T_o and J are listed in Table 2.2. Inset shows the same data when graphed as $\log\tau$ vs $1/T$. T is given in units of ϵ/k_B and τ in units of $\sqrt{m\sigma^2/\epsilon}$. Here, m is a particle mass, σ is a particle diameter, and ϵ is an energy parameter that characterizes interparticle interactions. See Refs. [7, 8, 9, 10, 11, 12] for the precise meaning in each particular case. The meaning of each acronym is given in Table 2.2.

in Figure 2.3(a). Table 2.2 shows the parameters used for the data collapse. J/T_o for the numerical simulation data is comparable in magnitude to the values obtained for many of the experimental liquids. The simulation data extends over three or four orders of magnitude while the experimental data extends over more than ten orders of magnitude.

2.5 Comparison with VFT

Also noted in Table 2.1 are the standard deviations obtained by fitting the VFT form to the same data. Both the quadratic form and the VFT form have three independent parameters. Considering all 67 liquid data sets, the mean standard deviation for the parabolic form is 0.073 ± 0.073 and for the VFT form is 0.088 ± 0.14. While the standard deviations are similar, there are at least two reasons to favor the quadratic form over the VFT form. The first [54] is that the quadratic form does not require the introduction of a metaphysical Kauzmann temperature – an implausible thermodynamic state point that by definition is unobservable [67]. The second is that, for approximately half the liquids fitted, the VFT form achieves small standard deviations with a pre-factor time that is less than 10 fs, which is too short to coincide with structural relaxation at any reference state of a molecular liquid.

Table 2.1: Fit Parameters for Fragile Glass Formers Data

System[Ref.]	Full Name	T_o/K[a]	J/T_o[b]	$\log \tau_o$/s[c]	$\log \eta_o$/P[d]	$\sigma(\sigma_{VFT})$[e]	T_m/K[f]	T_g/K[g]	Range/K[h]
3BRP[68]	3-bromopentane	192	4.3	-9.4		0.13 (0.13)	147	108	107-289
3Sty[69]	3-styrene	314	8.5	-6.5		0.024 (0.025)	242	237	235-280
5-PPE[65]	5-polyphenyl-ether	398	6.2	-12.4		0.0044 (0.058)		248	248-264
AFEH[54]	2-phenyl-5-acetomethyl-5-ethyl-1,3-dioxocylohexane	285	9.4	-6.1		0.0038 (0.0096)		219	220-240
B2O3[15]	boron oxide (B_2O_3)	1066	3.3		3.0	0.095 (1.0)	723	541	533-1665
BePh[70]	benzophenone	328	6.3	-11.0		0.05 (0.052)	321	208	215-240
BN[71]	butyronitrile	135	6.6	-4.8		0.025 (0.021)	116	97	97-116
BP2IB[54]	biphenyl-2yl-isobutylate	313	6.7	-9.4		0.0063 (0.0084)		209	210-232
BPC[72]	3,3,4,4,-benzphenonetetra-carboxylicdianhydride	432	9.9	-6.8		0.014 (0.007)		333	334-362
BSC[15]	Borosilicate Crown glass	2002	2.3		1.9	0.075 (0.15)		825	800-1594
CaKNO3[73]	Ca-K-NO_3^-	444	10.8		0.3	0.37 (0.22)		338	341-668
CN60.0[66]	soda lime silicate glass.0	1702	5.2		1.2	0.046 (0.061)		1030	1012-1809
CN60.2[66]	soda lime silicate glass.2	1668	3.2		1.8	0.086 (0.019)		820	803-1563
CN60.4[66]	soda lime silicate glass.4	1929	1.9		1.6	0.19 (0.045)		700	684-1563
Cum-1[54]	isopropyl-benzene	174	8.6	-6.9		0.028 (0.018)	177	129	130-149
Cum-2[15]	isopropylbenzene	194	6.8		-0.6	0.21 (0.32)	177	129	129-306
dBAF[74]	dibutyl-ammonium formate	220	6.6	-5.9		0.097 (0.031)		155	156-200
DBP-1[16]	dibutyl-phtalate	241	8.3	-6.2		0.052 (0.026)	238	179	180-224
DBP-2[15]	di-n-butylphtalate	320	4.1		-0.9	0.2 (0.36)		168	178-369
DC704[65]	tetraphenyl-tetramethyl-trisiloxane	306	7.9	-9.8		0.0097 (0.019)		213	211-240
DCHMMS [75]	dichyclohexyl-methyl-2-methylsuccinate	275	10.9	-5.4		0.0072 (0.0089)		221	220-240
DEP[54, 63, 64]	diethyl-phtalate	262	7.3	-7.6		0.024 (0.0098)	270	185	186-222
DHIQ[65]	decahydroisoquinoline	197	25.8	-4.3		0.042 (0.077)		180	180-192
dIBP[54]	di-iso-butyl-phtalate	247	9.7	-5.4		0.0028 (0.02)		194	195-221
DMP[54, 63, 64]	dimethyl-phtalate	261	8.5	-6.4		0.017 (0.0077)	275	195	196-220
DOP[54]	dioctyl-phtalate	251	7.8	-5.1		0.023 (0.0036)	223	187	188-220
DPG[54, 63, 64]	dipropylene-glycol	268	7.8	-5.9		0.043 (0.021)	<234	196	196-240
DPGDME[54]	dipropyle-glycol-dimethyl-ether	177	9.9	-6.0		0.015 (0.022)		136	139-155
EH[76]	ether-2-ethyl-hexylamine	183	9.1	-5.6		0.028 (0.011)	197	140	142-166

Table 2.1 – Continued

System[Ref.]	Full Name	T_o/K[a]	J/T_o[b]	$\log \tau_o$/s[c]	$\log \eta_o$/P[d]	$\sigma(\sigma_{VFT})$[e]	T_m/K[f]	T_g/K[g]	Range/K[h]
ER[77]	diglycidyl-ether-of-bisphenol A (epoxy-resin)	309	14.0	-6.7		0.014 (0.035)	325	255	259-291
FAN[78]	3-fluoro-aniline	225	10.3	-7.2		0.16 (0.16)		173	173-198
Gly[16]	glycerol	338	4.1	-7.7		0.033 (0.0053)	293	191	192-252
KDE[79]	cresolphthalein-dimethylether	461	7.1	-8.0		0.0095 (0.025)	387	318	315-383
mTCP[80]	*m*-tricresyl-phosphate	270	9.2	-5.6		0.018 (0.0095)	299	208	209-233
MTHF-1[54]	2-methyltetrahydrofuran	119	9.8	-6.9		0.022 (0.026)	137	92	91-108
MTHF-2[81]	2-methyltetrahydrofuran	126	8.5	-8.8		0.049 (0.11)	137	91	94-179
mTol [54, 63, 64]	*m*-toluidine	237	10.6	-6.6		0.01 (0.0051)		185	184-200
NBB[15]	*n*-butylbenzene	202	5.9		2.0	0.25 (0.16)	185	129	135-306
NBS[15]	NBS-711 standard	2780	1.1		1.5	0.1 (0.062)		705	665-1614
NBS 710[66]		2483	1.7		1.5	0.097 (0.018)		830	827-1776
nProp-1[81]	*n*-propanol	350	1.4	-10.7		0.12 (0.17)	147	99	100-300
nProp-2[15]	*n*-propanol	398	1.2		-2	0.21 (0.27)	147	99	104-370
NS 66[66]		2489	1.4		1.2	0.28 (0.19)		726	719-1805
NS 80[66]		2435	1.5		1.7	0.10 (0.065)		758	718-1759
OTP-1[82]	*o*-terphenyl	341	8.5	-8.9		0.038 (0.035)	329	243	252-282
OTP-2[83]	*o*-terphenyl	340	8.6		0.0	0.066 (0.064)	329	240	239-267
OTP-3[81]	*o*-terphenyl	357	7.7	-9.9		0.16 (0.18)	329	246	248-311
PDE[84]	phenolphthalein-dimethylether	397	9.3	-7.7		0.022 (0.031)	373	294	299-333
PG[54]	1,2-propandiol (propylene-glycol)	321	3.4	-7.7		0.0062 (0.0046)	214	164	180-211
PHIQ[54]	perhydroisoquinoline	208	18.5	-5.8		0.14 (0.055)		181	182-206
PP [85]	polypropylene	399	5.7		4.5	0.19(0.38)	??TM	264	266-343
PPG[16]	polypropylene-glycol	263	8.7	-6.1		0.049 (0.0063)	215	199	200-240
PS1[86]	titania-bearing sodium silicate melt #1	2395	1.7		1.5	0.078 (0.042)		796	837-1591
PS2[86]	titania-bearing sodium silicate melt #2	2688	1.3		1.3	0.074 (0.038)		746	784-1679
PS3[86]	titania-bearing sodium silicate melt #3	2109	1.9		1.9	0.081 (0.06)		765	815-1676
PT[16]	pyridine-toluene	146	17.5	-5.5		0.019 (0.023)		126	125-131
Sal-1[87]	salol	309	8.1	-8.5		0.05 (0.12)	315	221	218-382

Table 2.1 – Continued

System[Ref.]	Full Name	T_o/K[a]	J/T_o[b]	$\log \tau_o$/s[c]	$\log \eta_o$/P[d]	$\sigma(\sigma_{VFT})$[e]	T_m/K[f]	T_g/K[g]	Range/K[h]
Sal-2[88]	salol	299	9.1	-8.3		0.066 (0.048)	315	222	223-253
Sal-3[81]	salol	308	8.3	-8.5		0.069 (0.24)	315	221	220-309
SB[89]	sucrose-benzonate	421	11.2	-5.8		0.04 (0.019)	373	340	341-400
Sqa[65]	squalane	224	8.3	-5.3		0.092 (0.053)	235	170	170-210
TANAB-1[90]	tri-α-naphtylbenzene	519	6.8		-0.9	0.082 (0.34)		335	332-584
TANAB-2[15]	tri-α-naphtylbenzene	520	6.4		-0.8	0.1 (0.21)		335	333-588
TCP[54, 63, 64]	tricresyl-phosphate	280	8.8	-6.3		0.012 (0.013)	240	209	216-248
tNB[91]	trisnaphthylbenzene	510	7.1	-9.2		0.019 (0.023)		342	357-405
Tol[92]	toluene	152	9.8	-8.4		0.096 (0.093)	???	114	116-297
TPG[16]	tripropylene-glycol	251	8.9	-5.5		0.041 (0.0055)	232	192	192-228
TPP[93]	triphenyl phosphite	286	7.7		-0.5	0.08 (0.18)	296	204	203-291
Xyl[54]	xylitol	311	11.1	-5.8		0.026 (0.0057)	367	250	254-284

[a] T_o is the fitted onset temperature in K.
[b] J is the fitted energy scale over k_B.
[c] τ_o is the fitted onset relaxation time in seconds.
[d] η_o is the fitted onset viscosity in Poise.
[e] σ is the standard deviation of the quadratic form given by: $\left(1/(N-n)\sum_i \left(\log_{10}\tau_{\mathrm{fit},i} - \log_{10}\tau_{\mathrm{data},i}\right)^2\right)^{1/2}$. N is the number of fitted data points, $n = 3$ is the number of degrees of freedom for all reported fits. $i = \{1, N\}$ indexes the fitted points. σ_{VFT} is the standard deviation for fitting the parameters τ_o^{VFT}, A and T_K of the VFT form: $\tau = \tau_o^{VFT} \exp\left(A/\left(T - T_K\right)\right)$.
[f] T_m is the melting temperature.
[g] T_g is the glass transition temperature i.e., where $\eta = 10^{13}$ P or $\tau = 10^2$ s.
[h] The range of temperature for data reported in K. Only data for $T < T_o$ is fitted.

Table 2.2: Fit Parameters for Fragile Glass Former Simulations Data

System	Description	$T_o k_B/\epsilon$[a]	J/T_o[b]	$\log\left(\tau_o/\sqrt{m\sigma^2/\epsilon}\right)$[c]	σ[d]	Range/(k_B/ϵ)[e]	Ref.
Dzugutov	Dzugatov 50:50 Mixture	0.8	1.8	0.3	0.053	0.42-1	[7]
FLJ	Frustrated Lennard-Jones	0.3	1.6	1.5	0.0015	0.18-0.8	[8]
LJ 50:50	Lennard-Jones 50:50 Mixture	0.7	5.6	1.3	0.027	0.59-2	[9]
LJ 80:20 (MC)	Lennard-Jones 80:20 Mixture (Monte Carlo)	0.8	1.9	2.6	0.054	0.43-2	[10]
LJ 80:20 (MD)	Lennard-Jones 80:20 Mixture (Molecular Dynamics)	0.8	1.9	0.7	0.013	0.45-0.6	[11]
WCA 50:50	Weeks-Chandler-Andersen 50:50 Mixture	0.6	2.9	1	0.035	0.36-5	[12]

[a] T_o is the fitted onset temperature in k_B/ϵ

[b] J is the fitted energy scale over k_B.

[c] τ_o is the fitted onset relaxation time in $\sqrt{m\sigma^2/\epsilon}$.

[d] σ is the standard deviation of the quadratic form given by: $\left(1/(N-n)\sum_i \left(\log_{10}\tau_{\mathrm{fit},i} - \log_{10}\tau_{\mathrm{data},i}\right)^2\right)^{1/2}$. N is the number of fitted data points, $n = 3$ is the number of degrees of freedom. $i = \{1, N\}$ indexes the fitted points.

[e] The range of temperature for data reported in units of k_B/ϵ. Only data for $T < T_o$ is fitted.

2.6 Case Studies of Supercooled Liquid Theories

2.6.1 Introduction

In Chapter 1, I introduced several supercooled liquid theories and their predictions for the temperature dependence of transport properties such as the relaxation time, τ, and viscosity, η. In the previous sections, I showed that transport properties for over 50 liquids could be collapsed to a single, parabolic, form given in Eq. 2.4.

Here, I will directly compare the predictions of some of these theories to the parabolic form of Eq. 2.4. First, I will consider the connection between the VFT temperature, $T_{\rm VFT}$, and the Kauzmann temperature, $T_{\rm K}$. Following, I will compare the fits predicted by Adam-Gibbs theory presented in Section 1.3.2 as well as some of the empirical fits presented in Section 1.3.4. My goal is to distinguish fitting forms whose parameters are *material properties* from those whose parameters are dependent on the temperature range fit and do not converge. I will use the same procedure as outlined in Section 2.2. Then, I will examine the role of attractive forces in the dynamics of supercooled liquids. Finally, I will investigate the recent purported finding of a fragile-to-strong crossover in supercooled liquid transport data.

2.6.2 $T_{\rm VFT}$ vs $T_{\rm K}$

The VFT formula for transport property τ is

$$\log(\tau/\tau_{\rm VFT}^{(\infty)}) = \frac{A}{T - T_{\rm VFT}}, \tag{2.5}$$

where $\tau_{\rm VFT}^{(\infty)}$, A, and $T_{\rm VFT}$ are fitting parameters. It is possibly the most common of all expressions used in glass physics, often referred to as a law [94]. This formula is often invoked to attribute slowing dynamics in a supercooled liquids to a thermodynamic transition at the temperature $T_{\rm VFT}$. Adam-Gibbs theory [38] (Section 1.3.2) and random-first-order theory [41] (Section 1.3.3) connect this transition to an entropy crisis, where $T_{\rm VFT}$ is a recorder of a Kauzmann temperature as introduced in Section 1.2.4. The latter, $T_{\rm K}$, is an extrapolated temperature at which the entropy of the supercooled liquid equals that of the ordered solid. (A formula analogous to Eq. 2.5 is an exact result for a class of stochastic models [95].)

It is often asserted that $T_{\rm VFT} \approx T_{\rm K}$ is a good approximation [41], but it has been observed that experimental evidence is mixed [96]. To analyze the issue quantitatively, note that both $T_{\rm VFT}$ and $T_{\rm K}$ are constrained to lie below the glass transition temperature, $T_{\rm g}$, and the relative difference from that reference temperature is the pertinent measure. According to the tabulated temperatures for 33 different liquids [13], the quantities $(T_{\rm g}/T_{\rm VFT} - 1)$ and $(T_{\rm g}/T_{\rm K} - 1)$ are typically a few tenths. Their ratio, $R = (T_{\rm g}/T_{\rm VFT} - 1) \,/\, (T_{\rm g}/T_{\rm K} - 1)$, often differs significantly from unity. In particular, averaging over the 33 different liquids yields a mean value of $\langle R \rangle = 1.15$ and a root-mean-square deviation $\langle (R - \langle R \rangle)^2 \rangle^{1/2} = 0.613$. In other words, it is just as likely that $T_{\rm VFT}$ and $T_{\rm K}$ will differ significantly as it is that they

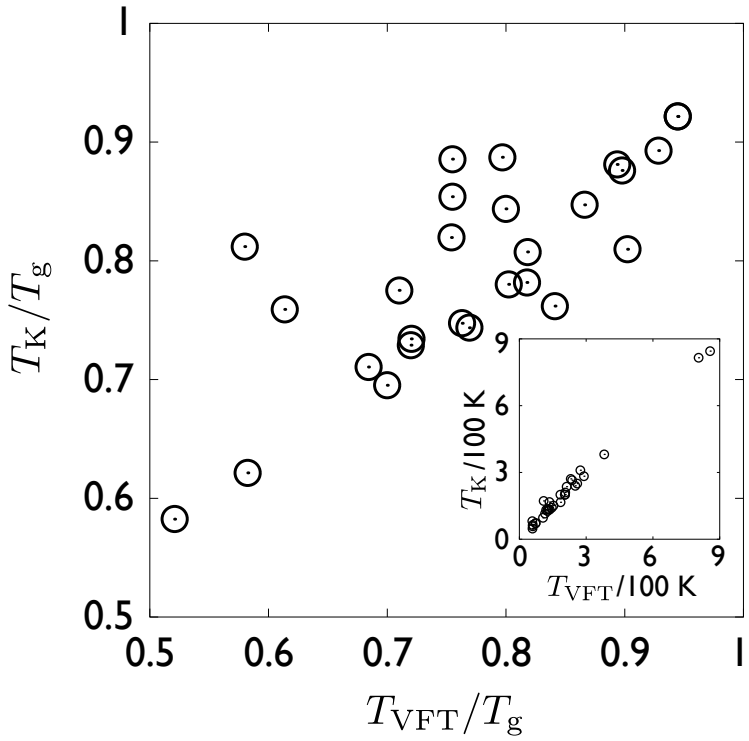

Figure 2.5: Comparison of $T_{\rm K}$ and $T_{\rm VFT}$. The main plot does so in units of $T_{\rm g}$ while the inset does so in units of 100 K. The circles represent 33 liquids compiled by Angell [13].

will be similar. Figure 2.5 illustrates this point. Notice that the commonly used comparison, shown in the inset to Figure 2.5, uses arbitrary units to plot $T_{\rm K}$ and $T_{\rm VFT}$, which gives the false impression that the two temperatures reliably track one-another. This impression results from the fact that $T_{\rm K}$ and $T_{\rm VFT}$ are never very far from $T_{\rm g}$, and $T_{\rm g}$ varies significantly from one system to another.

2.6.3 Comparison of Fits with Parabolic Fit

The VFT Fit vs. the Parabolic Fit

Independent of an alleged connection to thermodynamics, the utility of the VFT formula can be tested by examining whether its parameters are material properties. I do so for one typical fragile liquid, *o*-terphenyl (OTP). What I illustrate with this system is representative of what I generally find for a wide selection of supercooled liquids.

The onset temperature for OTP is about 350 K, and the glass transition temperature is 239 K. Data exists over this entire range [97]. I omit the normal liquid range $T > T_{\rm o}$, and only remark that the deficiencies of VFT I am about to demonstrate are more severe

when the temperature range is extended to include the normal liquid regime. With this range of data, I have fit the parameters for the VFT formula and those for the parabolic formula in three different ways: by including data from only the range of higher supercooled temperatures (267 K $< T <$ 350 K), by including data from only the range of lower supercooled temperatures (239 K $< T <$ 267 K), and by including data from the entire range of supercooled temperatures (239 K $< T <$ 350 K). The fitting parameters obtained in these ways are given in Table 2.3.

The entries to this table show a significant difference between parameters found from fitting the full range of data and those found from fitting only the higher temperature data. The VFT parameters found from fitting only the lower temperature data agree well with those found from fitting all supercooled data at the expense of a larger fitting error. For these cases, the error in reproducing the full range of supercooled liquid data is reasonably small, but at the expense of an unphysical value for the reference viscosity, $\eta_{\rm VFT}^{(\infty)}$. Figure 2.6 shows poor agreement between experiment and the VFT formula for high temperature data when only low temperature data is included in fitting (and vice versa). In the latter case, when only the higher temperature range of supercooled data is used to fit VFT parameters, the value of $T_{\rm VFT}$ is close to $T_{\rm g}$, causing the huge error reported in the second row of 2.3. In contrast, the parameters and quality of fits found with the parabolic form change little between the full set of data or either of the subsets of data.

Thus, parameters of the parabolic form appear to represent properties of the system, and those determined over one range of temperatures can be used to reliably predict properties over another range of temperatures at the same pressure. The parameters of the VFT form, however, depend upon both the properties of the system and the range of data considered, and as such the VFT form cannot predict properties outside the range over which it has been fit.

Table 2.3: Comparison between VFT and parabolic fits for supercooled liquid OTP

	VFT[1]				Parabolic[1]			
Fitted range	$\log \eta_{\rm VFT}^{(\infty)}$/P	A/K	$T_{\rm VFT}$/K	Err[2]	J/K	$T_{\rm o}$/K	$\log \eta_{\rm o}$/P	Err[2]
239 K - 350 K	-8.98	$1.03 \cdot 10^3$	191	0.20	$2.79 \cdot 10^3$	352	-1.88	0.064
267 K - 350 K	-4.30	254	238	51	$2.82 \cdot 10^3$	351	-1.86	0.087
239 K - 265 K	-8.38	999	191	0.29	$2.82 \cdot 10^3$	349	-1.60	0.13

[1]listed fitting parameters are determined by minimizing the mean square deviation between the fitting function and experiment for the specified range of data.

[2]Root-mean-square deviation between fitted function and experiment over entire set of supercooled data. That is, with the full set of data points, η_i at the respective temperature T_i, $i = 1, 2, ..., N$, where N is the total number of supercooled liquid data points determined by locating $T_{\rm o}$, ${\rm Err}^2 = (1/N) \sum_{i=1}^{N} [\log \eta(T_i) - \log \eta_i]^2$, where $\eta(T)$ is the fitting function at temperature T with parameters determined by minimizing the mean square deviation of the fitting function from experiment in the indicated range of experimental data.

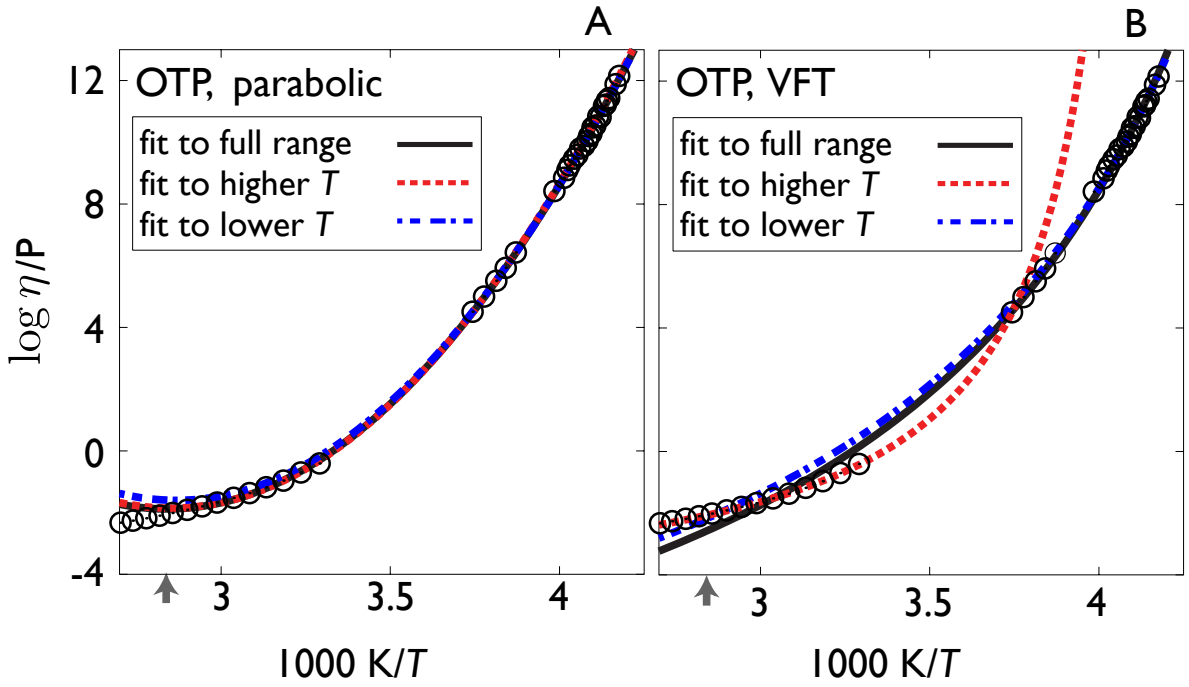

Figure 2.6: Examples of using Eq. 2.4 (A) or Eq. 2.5 (B) to fit viscosity, η, of a supercooled liquid as a function of reciprocal temperature, $1/T$. The circles are experimental data [14]. Three fits are shown for both equations. For one fit, parameters are determined by minimizing the mean square deviation between functional form and experiment for the full range of supercooled data, for the other two, parameters are found by minimizing the mean square deviation between the functional form and a subset of that data, the subset being either the higher temperature range of data or the lower temperature range of data. See Table 2.3 for specified ranges and parameters. The arrow indicates the value of $1/T_o$, marking the crossover between normal and supercooled liquid behaviors.

The Double Exponential Fit vs. The Parabolic Fit

The double-exponential formula for transport property τ is

$$\log(\tau/\tau_{dx}^{(\infty)}) = (K/T)\exp(C/T) \tag{2.6}$$

where $\tau_{dx}^{(\infty)}$, K, and C are fitting parameters. A special case, where K and C are of the same order, is the behavior of two-spin (or two-particle) facilitated lattice models [98]. Over the lower half of the temperature range between T_o and T_g, the double exponential has been used to successfully collapse transport data [43]. Mauro and co-workers [14] and others [99] have applied it to a broader range and report that Eq. 2.6 is superior to both the VFT form, Eq. 2.5, and the parabolic form, Eq. 2.4. In fact, the double-exponential form suffers from the same malady as the VFT form when applied to fit data over the full range of supercooled

Table 2.4: Comparison between double exponential and parabolic fit for supercooled liquid B_2O_3

	Double Exponential[1]				Parabolic[1]			
Fitted range	$\log \eta_{\rm dx}^{(\infty)}$/P	K/K	C/K	Err[2]	J/K	$T_{\rm o}$/K	$\log \eta_{\rm o}$/P	Err[2]
533 K - 970 K	0.524	511	$1.41 \cdot 10^3$	0.13	$3.51 \cdot 10^3$	$1.07 \cdot 10^3$	2.96	0.087
675 K - 820 K	1.61	169	$2.01 \cdot 10^3$	0.46	$3.46 \cdot 10^3$	$1.05 \cdot 10^3$	3.14	0.20
533 K - 675 K	-0.940	974	$1.12 \cdot 10^3$	0.25	$3.74 \cdot 10^3$	$1.01 \cdot 10^3$	3.14	0.14

[1]Listed fitting parameters are determined by minimizing the mean square deviation between the fitting function and experiment for the specified range of data.
[2]As defined in Table 2.3.

temperatures. As a data set is enlarged, its parameters fail to converge, implying these parameters are not material properties and the formula cannot be used to predict data not yet measured. The problem is not as severe as it is for the VFT form, owing to the fact that the double exponential is not singular while the VFT expression is singular. But the deficiency of the double-exponential form is nonetheless significant, as illustrated in Figure 2.7 and Table 2.4.

My illustration considers the inorganic glass forming liquid B_2O_3 [15]. The behaviors found for this system are typical of what I find for several other systems. For this particular system, the onset temperature for this liquid is close to 1000K, and the glass transition temperature for this liquid is about 500K. Fitting data over this entire range, the double-exponential form proves reasonably accurate, but its parameters change markedly as the range of fitted data changes. Fitting only higher temperature data, 675 K $\leqslant T \leqslant$ 820 K, yields a function that inaccurately describes the lower temperature data, and fitting only lower temperature data, 533 K $\leqslant T \leqslant$ 675 K, yields a function that inaccurately describes the higher temperature data. In contrast, the parameters and excellent quality fits of the parabolic form change little as the range of fitted supercooled data changes.

Thus, for the purpose of employing a particular functional form to predict low temperature properties from measured properties at higher supercooled temperatures (or vice versa), Eq. 2.6 is superior to the VFT expression, but this double exponential form advocated by Mauro and coworkers [14] is inferior to the parabolic form, Eq. 2.4.

The Fractional Exponential Fit vs. The Parabolic Fit

In both the VFT and double-exponential forms, temperature variations are more rapid than in the parabolic form. What if temperature variation is taken to be less rapid? An alternative of this type is the specific fractional-exponent form suggested by numerical solutions to Saltzmann and Schweizer's theory for structural relaxation in polymer melts [44],

$$\log(\tau/\tau_{\rm c}) = X\,(T_{\rm c}/T - 1)^{1.57}\ . \tag{2.7}$$

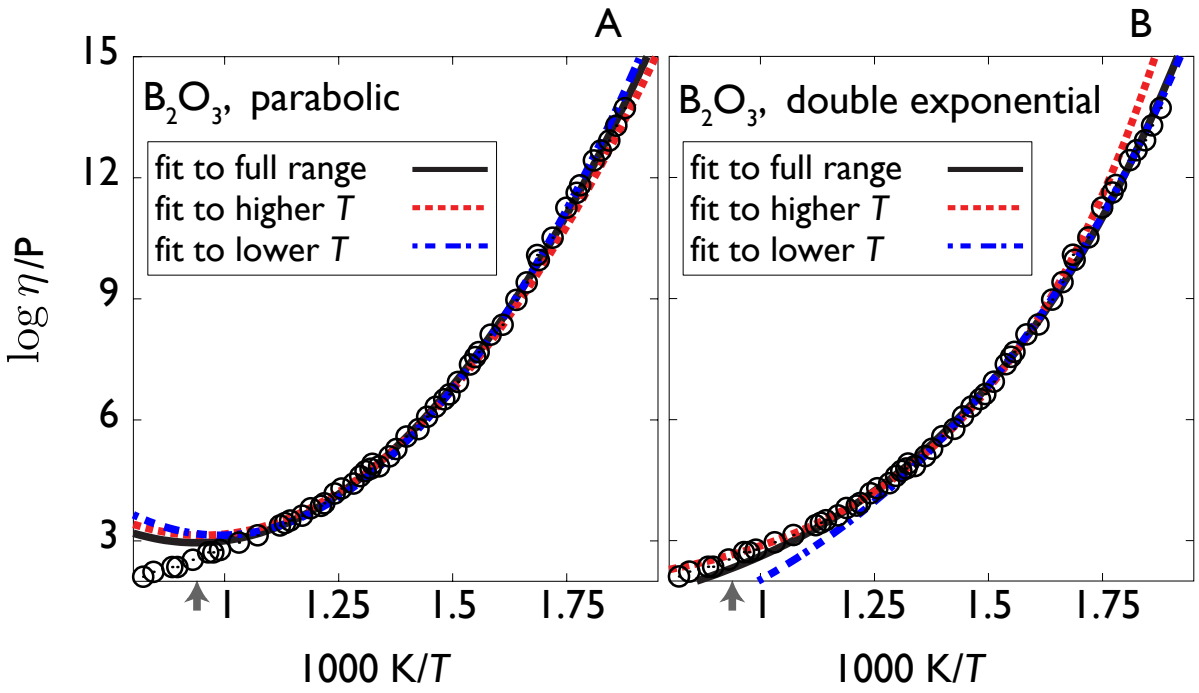

Figure 2.7: Examples of using Eq. 2.4 (A) or Eq. 2.6 (B) to fit viscosity, η, of a supercooled liquid as a function of reciprocal temperature, $1/T$. The circles are experimental data [15]. Three fits are shown for both equations. For one fit, parameters are determined by minimizing the mean square deviation between functional form and experiment for the full range of supercooled data, for the other two, parameters are found by minimizing the mean square deviation between the functional form and a subset of that data, the subset being either the higher temperature range of data or the lower temperature range of data. See Table 2.4 for specified ranges and parameters. The arrow indicates the value of $1/T_o$, marking the crossover between normal and supercooled liquid behaviors.

I illustrate the performance of this expression in Figure 2.8 and Table 2.5. I do so with data for the glass forming polymer melt polypropylene glycol (PPG) [16]. The onset temperature for this liquid is about 264 K, and its glass temperature is about 199 K [1]. The data covers most of this supercooled region, but not all the way up to the onset. As in the previous two case studies, I consider three ranges of the existing data: the entire data set, which extends up to about 10% of the onset temperature, T_o, a lower temperature subset of that data, and a higher temperature subset of that data. As with the VFT and double-exponential forms, I find that the fitting parameters for this fractional-exponential form depend upon the range of data considered. My illustration of this fact is typical of what I find when treating other materials with the same analysis.

Due to the nature of the fractional exponent, this functional form can be used to fit data

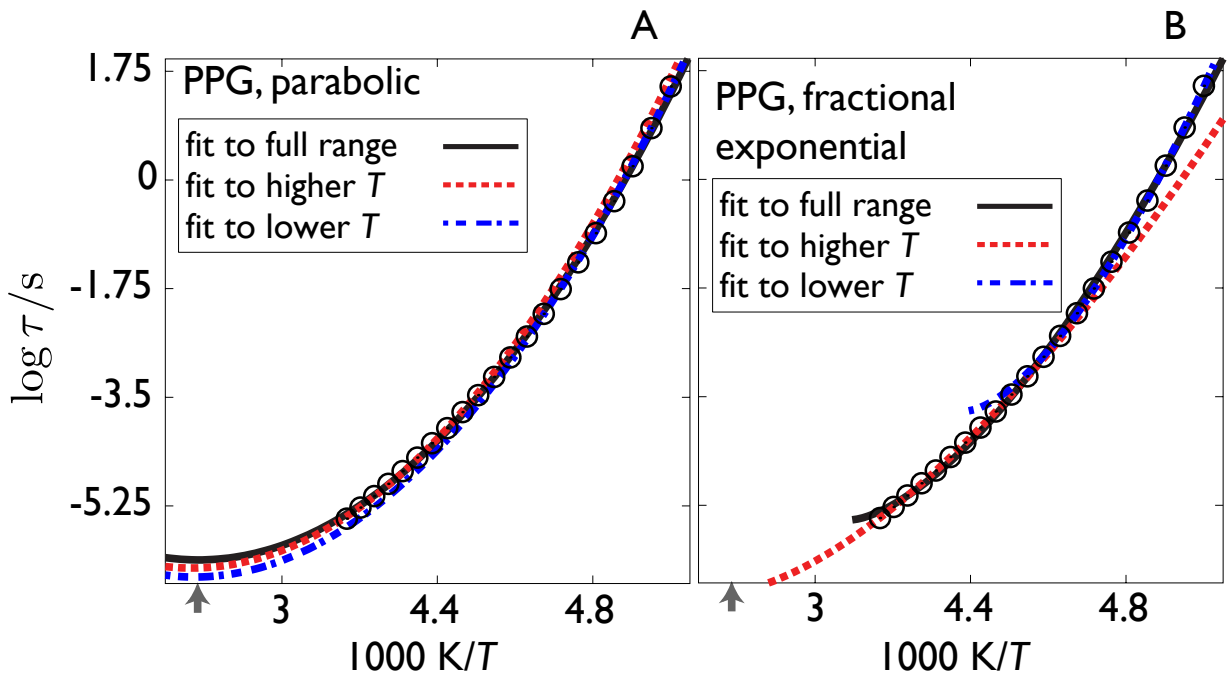

Figure 2.8: Examples of using Eq. 2.4 (A) or Eq. 2.7 (B) to fit relaxation time, τ, of a supercooled liquid as a function of reciprocal temperature, $1/T$. The circles are experimental data [16]. Three fits are shown for both equations. For one fit, parameters are determined by minimizing the mean square deviation between functional form and experiment for the full range of supercooled data, for the other two, parameters are found by minimizing the mean square deviation between the functional form and a subset of that data, the subset being either the higher temperature range of data or the lower temperature range of data. See Table 2.5 for specified ranges and parameters. The arrow indicates the value of $1/T_o$, marking the crossover between normal and supercooled liquid behaviors. The leftmost endpoints of the fit lines in figure (B) indicate the upper-temperature end point for applying Eq. 2.7. This temperature changes depending upon the range of data considered, and data for $T > T_c$ must be excluded from fits using Eq. 2.7.

for $T > T_c$. If the exponent were 2, rather than 1.57, this temperature would be the onset temperature. When using an exponent of 1.57 with subsets of the data where temperatures are all much smaller than T_o often one obtains $T_c < T_o$, so that less than the complete set of supercooled data can be covered. Further, unlike the parabolic form with parameters that vary little with changing data sets, the best fits of Eq. 2.7 produce parameters T_c and X that vary widely from one subset of data to another. Moreover, the function obtained fitting parameters to the higher temperature range of data, 222 K $\leqslant T \leqslant$ 240 K, provides an inaccurate representation of the data at the lower temperatures, and the function obtained

fitting parameters to the lower temperature range of data, 200 K $\leqslant T \leqslant$ 218 K, provides an inaccurate representation of the data at the higher temperatures. In contrast, the excellent quality of fits obtained with the parabolic form, Eq. 2.4, change little as the range of fitted data change.

Thus, the fractional exponent 1.57 proves to be less satisfactory than that of the parabolic form, Eq. 2.4.

2.6.4 The Role of Attractive Forces in Supercooled Liquids

The prior sections present evidence in support of Eq. 2.4 as a universal form for transport properties of fragile supercooled liquids. In this section, I show that by accepting the validity of this form I sensibly organize recent simulation results that might appear puzzling in the absence of this organization. In particular, Berthier and Tarjus [17] have shown that at some supercooled temperatures and densities relaxation in the Kob-Andersen Lennard-Jones (LJ) mixture [100] is orders of magnitude slower than that in the corresponding Weeks-Chandler-Andersen [101, 12] (WCA) mixture. The difference between the WCA and the LJ potential reflects the significance of attractive forces, which are present in the LJ mixture and absent in the WCA mixture. Does the Berthier-Tarjus finding reveal a new mechanism for glassy physics, one that does not follow from constraints and local rigidity imposed by repulsive forces?

The effects of attractive interactions uncovered by Berthier and Tarjus appear in dynam-

Table 2.5: Comparison of Fractional Exponential and Parabolic fit for PPG

	Fractional Exponential[1]				Parabolic[1]			
Fitted range	$\log \tau_c^{(\infty)}$/s	X	T_c/K	Err[2]	J/K	T_o/K	$\log \tau_o$/s	Err[2]
200 K - 240 K	-5.49	72.4	244	0.068	$2.26 \cdot 10^3$	264	-6.12	0.042
222 K - 240 K	-6.66	41.8	265	0.33	$2.27 \cdot 10^3$	265	-6.25	0.13
200 K - 218 K	-3.73	116	227	0.11[3]	$2.29 \cdot 10^3$	265	-6.39	0.088[3,4]

[1]Listed fitting parameters are determined by minimizing the mean square deviation between the fitting function and experiment for the specified range of data.
[2]As defined in Table 2.3.
[3]When the fit range is restricted to the lowest temperatures, T_c is lower than the lowest data point available for PPG. Therefore, the Err is calculated only for $T <$ 227 K for both the fractional exponential and the parabolic fit for sake of comparison. This requires that the seven highest temperature points be excluded from consideration. If those points are included, the Err for the fractional exponent over the entire range considered would become undefined.
[4]Over the entire range for which $T < T_o =$ 264 K, the Error for the the parabolic fit using the parameters for this range becomes 0.13.

ics, but not structure. They show that the pair distribution functions of the two mixtures differ little. Dynamics is associated with fluctuations away from mean local structure. Repulsive forces dominate the most likely equilibrium arrangements. They also constrain motions of particles, so that any spatial reorganization is rare and requires the coordinated displacements of several particles. As such, potential energy barriers to reorganization will have contributions from the attractive interactions between several pairs of particles. The sums of small attractive force contributions from these many particles can then become significant.

To pursue this idea, I have examined the effects of attractive forces on supercooled fluid transport through the behaviors of J and T_o because these parameters characterize the energetics of these collective displacements [35]. I have fit the simulation data [17] reported to determine the values of these parameters as functions of the liquid-mixture density. These results are shown in Figures 2.9 and 2.10 along with the reference time scale τ_o. While the values of J, T_o, and $\log \tau_\mathrm{o}$ do vary slightly between the two types of mixtures at the same density, their overall trends as functions of density are the same. Both liquid mixtures therefore seem to behave as similar supercooled liquids.

One interesting feature revealed in Figure 2.10 is that increasing density causes both T_o and J to increase. For the LJ mixture, they do so proportionally to within 15% of $J/k_\mathrm{B}T_\mathrm{o} \approx 2.75$ for all densities. This proportionality is expected for systems, like the supercooled LJ mixture, that have behavior consistent with that of an inverse-power repulsion [102, 103]. This proportionality does not hold, however, for the WCA mixture, where $J/k_\mathrm{B}T_\mathrm{o}$ changes monotonically from about 1.5 at low density end of the graphs to about 3 at high density ends. Thus, combinations of J and T_o seem to be system dependent.

Berthier and Tarjus remark on the "enormous" factor of $10^{3.2}$ by which τ for the LJ mixture differs from that for the WCA mixture at $\rho\sigma_\mathrm{AA}^3 = 1.2$ and $k_\mathrm{B}T/\epsilon_\mathrm{AA} = 0.41$. This effect reflects differences in J/ϵ_AA and $k_\mathrm{B}T_\mathrm{o}/\epsilon_\mathrm{AA}$, which are 1.8 and 0.73 for the LJ mixture, and 0.92 and 0.60 for the WCA mixture, respectively. The onsets to supercooled behavior thus appear at similar temperatures, and the activation energies for dynamics differ by less than one intermolecular attractive energy. Moreover, as the density increases the characteristic parameters for the two systems seem to converge to the same respective values. These findings are consistent with empirically established fact that the basic principles of supercooled liquids are well captured by models without attractive intermolecular forces [102, 103].

Thus, while dynamical effects of attractive forces are notable in a supercooled liquid, temperature dependence of transport obeys the parabolic law with or without attractive forces as would be expected for a universal underlying hierarchical dynamics. By considering the numerical results of Berthier and Tarjus by using the picture of glassy physics as a class of phenomena caused by local constraints rigidity I take a result which at first appears to contradict my previous results and reorganize it in a way that shows that no contradiction is actually present.

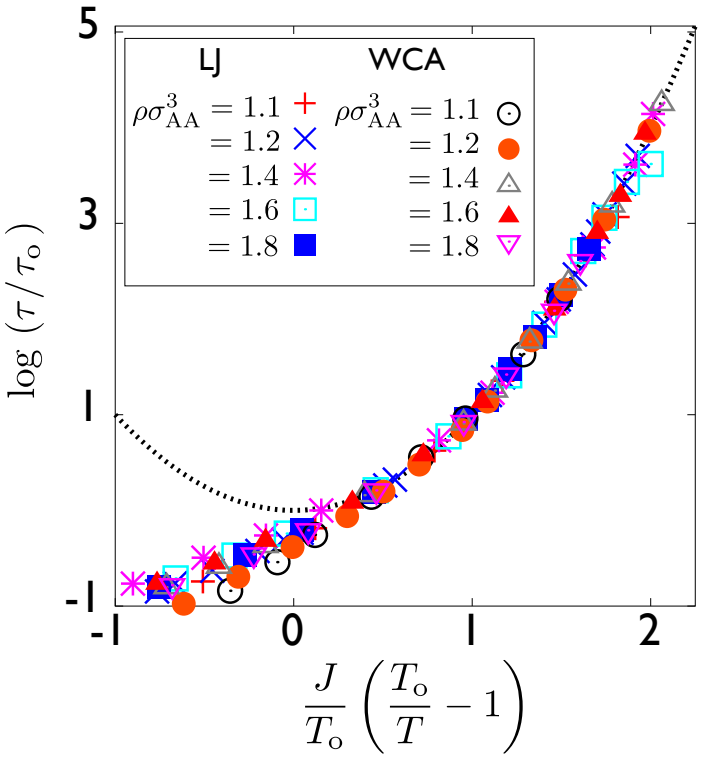

Figure 2.9: Parabolic collapse for WCA & LJ binary mixture simulation data [17] for various densities, ρ. Parameters of fit are described in Eq. 2.4. Dotted line is the universal parabolic form.

2.7 Fragile-to-Strong Crossover in Supercooled Liquids

Garrahan-Chandler theory predicts that transport properties of fragile glass-formers which follow the parabolic form of Eq. 2.4 to an Arrhenius form $\log \tau \sim A/T$ at a crossover temperature $T_x < T_o$ as presented in Section 1.3.5. The observation of this crossover is apparent in studies of the crossover model described in Section 1.3.5 [49]. But this so-called "fragile-to-strong" (FS) crossover at a temperature $T_x < T_o$ has proved difficult to observe because most bulk fluids fall out of equilibrium at a glass transition temperature T_g that is higher than T_x. Certain systems seem to exhibit this phenomenon [104, 105]. In these cases, the systems considered are confined nano-scale systems that may or may not reflect the behaviors of macroscopic materials. More recently, Mallamace et al [18] report the observation of T_x for a large number of bulk supercooled liquids. In truth, they observe the onset to supercooled behavior, and the reported values of T_x are poor lower-bound estimates to onset temperatures T_o. This fact is consistent with transport decoupling appearing only

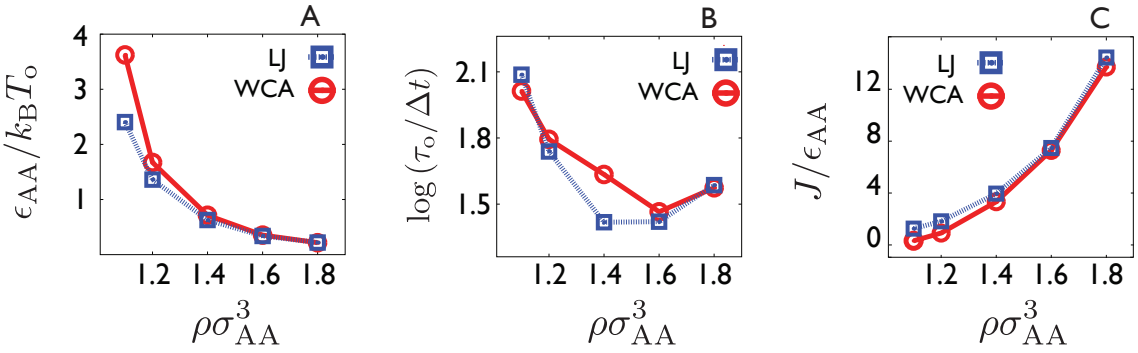

Figure 2.10: Fitting parameter trends using Eq. 2.4 for the Kob-Andersen LJ and corresponding WCA binary mixtures from [17] for various net particle densities, ρ. (A) The inverse onset temperature, $1/T_o$, as a function of density ρ. (B) Logarithm of relaxation time at the onset temperature, $\log \tau_o$, as a function of ρ. (C) Transport energy parameter, J, as a function of ρ. Lines connecting points in (A), (B) and (C) are guides to the eye. Error estimates are the size of the symbols. The unit of time is $\Delta t = (m\sigma^2_{AA}/48\epsilon_{AA})^{1/2}$.

below temperatures identified with the crossover in Ref. [18].

To illustrate this understanding about Ref. [18], I graph data in Figure 2.11 for two typical supercooled liquids. The data is compared with the parabolic form for transport property τ (denoting either relaxation time or viscosity) and with the straight-line fit that would be associated with the Arrhenius temperature dependence. I consider data for liquid salol in Figure 2.11*A*. This is the same liquid and the same temperature range considered in Figure 1*A* of Ref. [18]. The two figures are strikingly different, due in part to Ref. [18] showing an outlying data set [83] that is discredited by subsequent studies on the same liquid [87, 88, 106, 82]. Unlike Figure 1*A* of Ref. [18], my graph shows excellent agreement between reproducible experimental data and the parabolic form.

Figure 2.11*B* considers a second liquid to illustrate that the behavior for salol is consistent with that of other systems. Indeed, the parabolic form, with its three material properties τ_o, J and T_o, has been used to collapse data for more than 50 supercooled liquids (Figure 2.3 and Table 2.1) over the entire supercooled temperature range, $T_o > T > T_g$, and this form appears to be universal for all fragile glass formers. Here, I have chosen to show two specific examples to contrast with the obscuring clutter of data analyzed with six-parameter fits in Figure 1*C* and 2 of Ref. [18].

The two graphs in Figure 2.11 here and those presented in Figures 2.3, 2.6, 2.7, and 2.8 indicate that all reliable reversible transport data for bulk supercooled liquids appear to be smooth, with no compelling feature suggesting a change from parabolic to linear behavior. Rather, it seems that the FS crossover reported in [18] results from confusing T_o with T_x, and how, over a limited range, a parabola looks like a straight line. The search for the FS crossover in bulk materials therefore remains elusive.

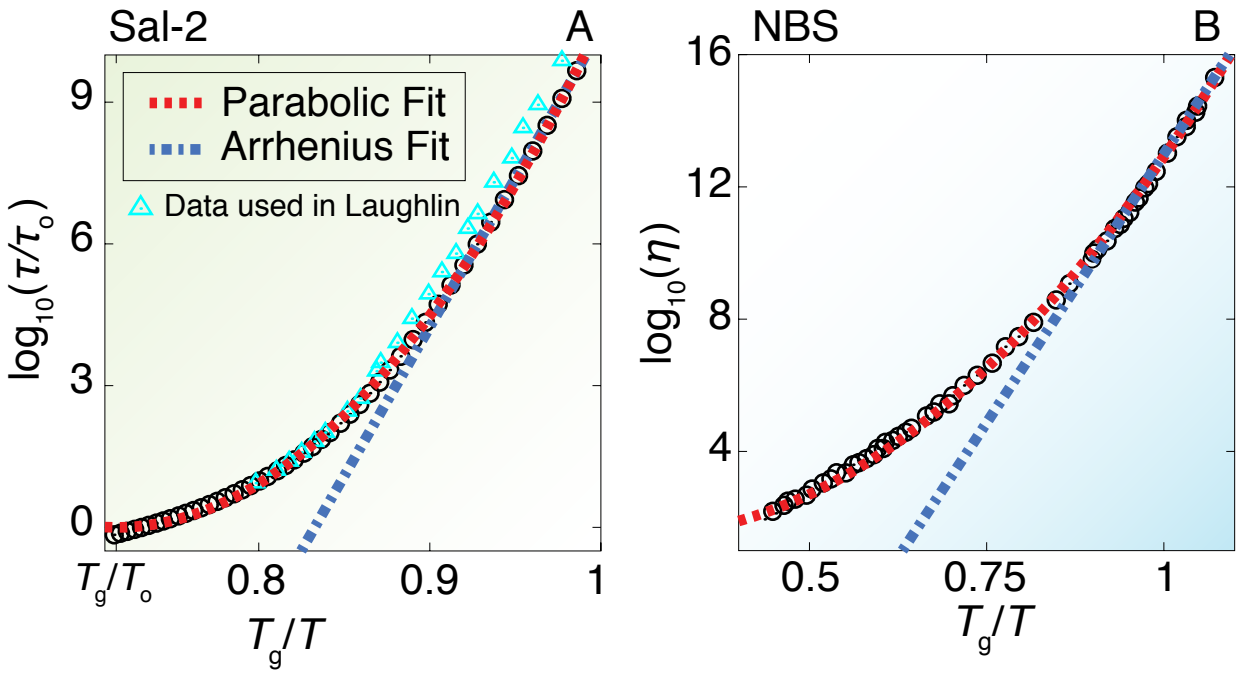

Figure 2.11: Transport properties as a function of T_g/T for two typical supercooled liquids. Black circles in (A) and (B) represent experimental data considered in Section 2. Labeling here is consistent with Table 2.1 - that is to say that Sal-2 and NBS refer to the same experimental measurements and fit parameters as in the table. Red dashed line is the fit parabolic form for $T < T_o$, as in [1]. Blue dashed line represents Arrhenius fit for lowest T points [18]. (A) Relaxation time, τ, of Salol where $T_g = 221$ K is the glass transition temperature where $\log(\tau_g/\text{s}) = 2$. (B) Viscosity, η (given in units of Poise, labeled P), of NBS where $T_g = 708$ K is the glass transition temperature where $\log(\eta_g/\text{Poise}) = 13$. It is generally assumed that $\tau \propto \eta$, and, with this assumption, (A) includes data used in Ref. [18] (triangles).

Chapter 3

Dynamical Phase Transitions in KCMs

3.1 Introduction

In Chapter 2 I explored the validity of the parabolic form which can be used to collapse transport properties of supercooled liquids onto a single curve [1] - a result predicted by Garrahan-Chandler theory and is based on the idea of dynamic facilitation introduced in Chapter 1. Furthermore, in Chapter 1 I introduced two of the most basic kinetically constrained models: The FA and east models. In this chapter, I will present a study of altered versions of these models known as the *soft* FA and *soft* east models. They are known as softened models because the kinetic constraints are not rigid. Moreover, I will investigate the behavior of these softened models in space and time including the emergence of a nontrivial space-time critical point and its implications to"real" glass formers.

3.2 Phase Transitions

Before I introduce dynamical phase transitions, it is important to have a reference point to ordinary thermodynamic phase transitions. Dynamical phase transitions have much in common with their thermodynamic counterparts. Thermodynamic first order phase transitions are characterized by discontinuous jumps in a thermodynamic observable as a function of an intensive field [25]. Common examples of such a phase transition are the abrupt change in density of water as it boils off into gas and the spontaneous ordering of a paramagnet in the presence of a magnetic field [25]. Moreover, at a first order phase transition the susceptibility, χ, of a system which is related to the derivative of an observable A with respect to an intensive field h diverges at a particular value of $h = h^*$. At h^* the first order phase transition occurs. In the example of boiling water at 1 atm of pressure, h^* would be the the boiling temperature $T_\mathrm{b} = 100K$ [107].

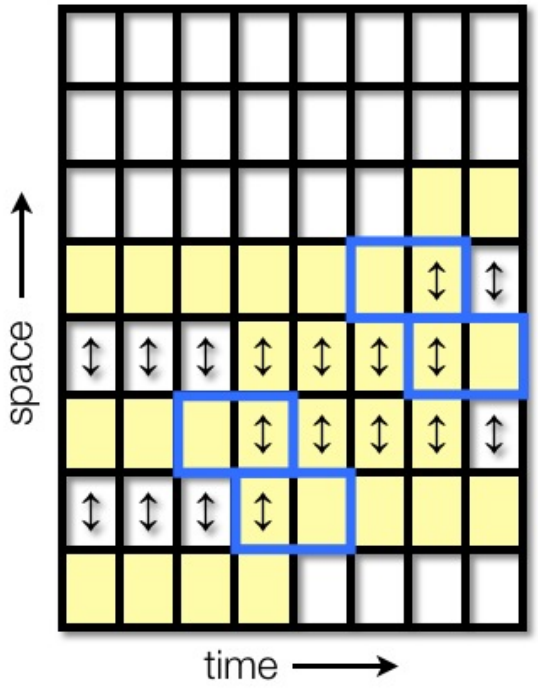

Figure 3.1: Schematic of a trajectory for the hard FA model. Vertical axis represents space where $N = 8$ lattice sites. Horizontal axis represents time where $t_{\text{obs}} = 8$ Monte Carlo time steps. Arrows indicate occupied sites and direction of dynamical facilitation. Yellow sites indicate sites which are facilitated at that time slice. Blue boxes highlight locations where there has been a configurational change between some time $t - \delta t$ and the time t. For this trajectory, the activity $K = 4$ as there have been 4 configurational changes.

At h^* the two phases (say, the high and low density phases of liquid and vapor) are in equilibrium and both phases are equally probable. This occurs at the point at which the free energy of the two phases are equal [25].

In principle these behaviors - the instantaneous jump in an extensive observable and the divergence of the susceptibility - only occur in the thermodynamic limit of infinite system size. In finite systems, the change in the observable, while large, is still continuous. Therefore, the susceptibility cannot diverge. Unfortunately, the nature of computer simulations is finite causing the distinction between a true first order phase transition and a continuous crossover to not always be evident. Fortunately, there is a signature of a first order phase transition in the scaling of the susceptibility as a function of system size. For a system of size N the susceptibility scales linearly with N [108], Though the two phase are in coexistence at h^*, a large surface tension between the phases means that if a large system is prepared in one of the two phases, transitions to the other phase are rare because the free energy barrier to nucleating the other phase is large. While methods have long existed for understanding the

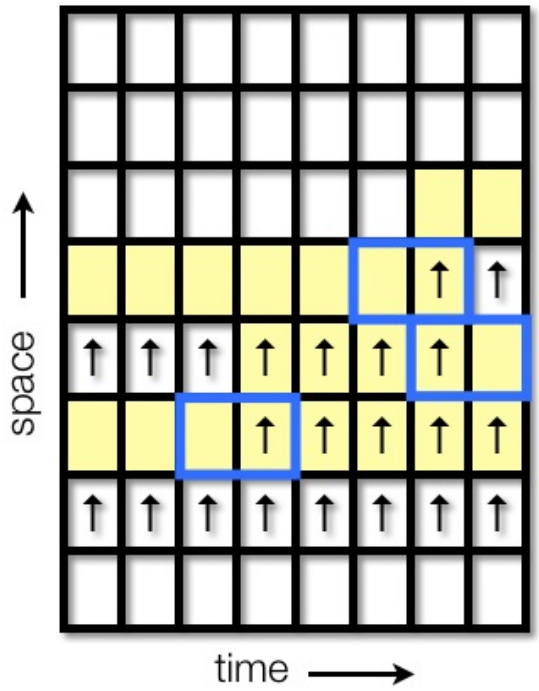

Figure 3.2: Schematic of a trajectory for the hard east model. Vertical axis represents space where $N = 8$ lattice sites. Horizontal axis represents time where $t_{\text{obs}} = 8$ Monte Carlo time steps. Arrows indicate occupied sites and direction of dynamical facilitation. Yellow sites indicate sites which are facilitated at that time slice. Blue boxes highlight locations where there has been a configurational change between some time $t - \delta t$ and the time t. For this trajectory, the activity $K = 3$ as there have been 3 configurational changes.

thermodynamics of such systems (such as umbrella sampling [25]) methods for learning about the kinetic aspects of these processes have only recently been developed. These methods introduced to circumvent this problem are known as rare-event sampling techniques. This has become a cottage industry among statistical physicists [109, 110]. The method I employ in my simulations is a particular flavor of transition path sampling [111].

Thermodynamic critical points are another type of phase transition. Unlike first order transitions, these higher order phase transitions (often called "second order" phase transitions) have no discontinuities in extensive order parameters as functions of an intensive field [25]. Nevertheless, there are interesting emergent properties that occur at critical points. While first order transitions are usually categorized by two distinct, degenerate free-energy basins separated by a large energetic barrier, a critical point is characterized by the first disappearance of that barrier such that the surface tension between the two phases has vanished. Thus, critical points are often thought of as ends to first order phase transitions lines (though a line of critical points can in fact terminate a plane of first order transitions and so

on). One common such critical point is the liquid-vapor critical point of water at 647 K and 218 atm of pressure [107]. At this point, the density based distinction between liquid and vapor disappears and there is only one fluid phase. This point is characterized by critical opalescence due to the large, macroscopic fluctuations caused by the lack of surface tension between the two once-distinct phases. The appearance of a critical point at the end of a first order transition line also indicates that the two phases must have the same symmetry (such as rotational or translational symmetries in liquid and vapor) because there can be a continuous path that takes you from one phase to the other without ever undergoing the symmetry breaking associated with a first order transition. In the context of renormalization group theory, critical points are fixed points and self-similar such that there is length-scale invariance [25] and the system is fractal-like.

For all the above thermodynamic phase transitions one typically considers an ensemble of configurations. For an Ising ferromagnet that would be the instantaneous configuration. In order to study phase transitions one must be able to study ensembles of such configurations and their relative probability. For dynamical phase transitions, I will consider the dynamical analog to configurations: Trajectories [53, 19, 20, 112, 113, 114].

3.3 Dynamical Phase Transitions

Observing a dynamical phase transition requires defining a space-time observable. Once such observable is the activity K [53, 20, 112, 113, 115, 116]. K records the number of configurational changes in a trajectory of size N and length t_{obs}. I will define K mathematically in the coming sections. Unlike a thermodynamic observable, such as the density or energy, K is only defined as a function of a space-time trajectory. The trajectory has thus replaced the configuration as the elements of the ensemble. At a first order dynamical transition in K, one can expect a discontinuous jump in the value of K as well as diverging dynamic susceptibility. The existence of dynamical phase transitions in glass forming models has been explored previously for several different models. Among these are kinetically constrained lattice models such as the (hard) FA and east models [19, 20] as well as atomistic models such as binary mixtures [117]. The existence of a first order phase transition between an active trajectory phase with high K and an inactive one with low K has been shown analytically and numerically for lattice models. The phase diagram of these models is given in Figure 3.4(A). The line of first order transitions is infinite, never ending in a critical point. One possible explanation for the lack of a critical point is that the two phases do not have the same symmetry. For example, the active phase is ergodic whereas the inactive phase might be non-ergodic. Moreover, as I will introduce in Section 3.5 if one couples an intensive, conjugate field s to K one finds that in the thermodynamic limit the transition value, s^*, is exactly at $s = 0$ (corresponding to dynamics in our physical world).

For atomistic models such as WCA binary mixture and the Kob-Andersen binary mixture [117, 118] qualitative evidence exists to suggest that a first order dynamical phase transition

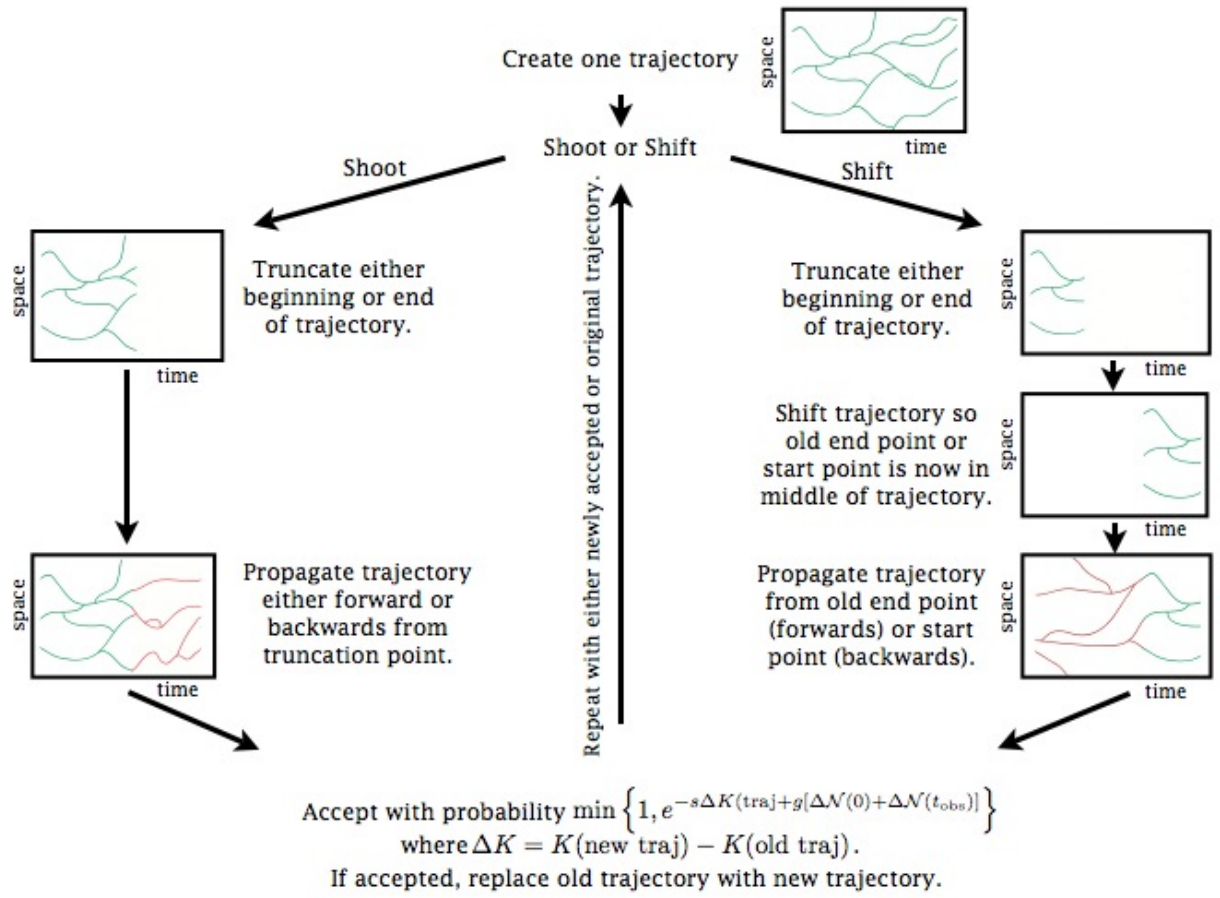

Figure 3.3: Flow diagram for s-ensemble TPS. At the top, one trajectory is generated. Next, a shifting or shooting move is chosen with equal probability, as is a direction (forward or backward). Green lines indicate the original configuration of the trajectory in space-and-time. These lines have replaced the arrows in Figures 3.1 and 3.2. On the left, a forward shooting move is shown where the initial trajectory is truncated and the remainder is regenerated (red). For backward shooting moves (not shown), the beginning of the trajectory is removed and regenerated by running the simulation backward from the shooting point. The new trajectory is accepted with the probability $\min\left\{1, e^{-s\Delta K(\text{traj}+g[\Delta\mathcal{N}(0)+\Delta\mathcal{N}(t_{\text{obs}})]}\right\}$. Here Δ represents the difference in the quantity between the new trajectory and the initial trajectory. If the new trajectory is accepted, the new trajectory replaces the old trajectory and the procedure is restarted. If the new trajectory is rejected, I revert to the old trajectory and start again. On the right side, a backward shooting move is shown. First, as in the shooting move, the trajectory is truncated. Then, the beginning of the trajectory is moved to the end of the trajectory and the beginning of the trajectory is regenerated by simulating the system "backward". For forward shooting moves, the beginning of the trajectory is removed and the end is shifted to become the new beginning and the system is regenerated until t_{obs} from the former endpoint of the old trajectory. The acceptance criterion for moves generated by shifting is identical to that for shooting moves.

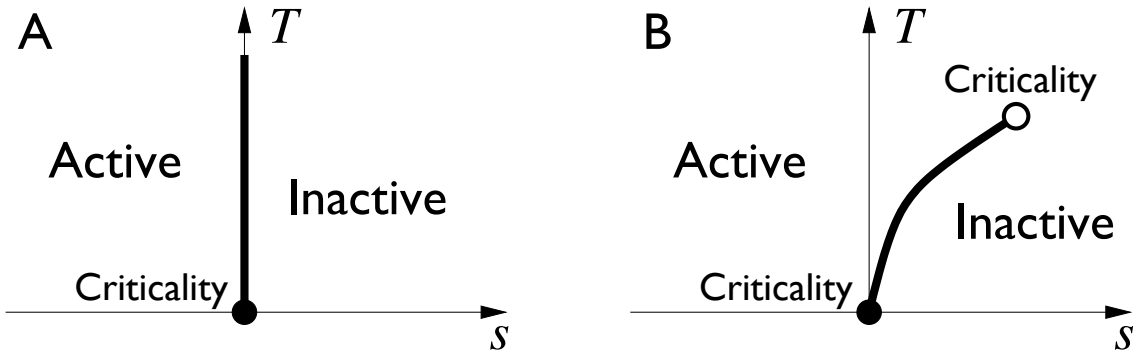

Figure 3.4: Space-time phase diagrams for KCMs. (A) shows the generic phase diagram for standard, hard KCMs such as the FA and the east models introduced in Chapter 1. The bold line indicates the first order phase boundary between the active phase, which has large K and requires $s < 0$, and the inactive phase, which has small K and requires $s > 0$. $s = T = 0$ is indicated with a filled circle and is the trivial "critical" point where $\langle K \rangle_s$ no longer distinguishes between the two phases and $K = 0$ for both phases. For hard systems the first order line extends to infinite temperature [19, 20]. (B) Sketch of phase diagram for softened system. The transition between the active and inactive phase no longer occurs at $s = 0$ but rather at $s > 0$ for $T > 0$. Here, the first order line terminates at a non-trivial finite-temperature critical point indicated by an open circle. This critical point is distinct from the trivial critical point at $s = T = 0$ and is analogous in scaling behavior near a liquid-vapor transition.

persists in these more complicated models. This qualitative evidence is corroborated with some finite size scaling, however data are limited since simulating an ensemble of trajectories for atomistic systems remains a challenging computational task.

My work seeks to bridge the gap between the lattice-based FA and east model simulations and the continuous, atomistic simulations to determine if a first order phase transition survives in models which are not fully kinetically constrained. If only completely constrained models support two distinct phases, this suggests that "real" models - which are inherently soft - cannot truly exhibit this behavior. However, if softened facilitated models support two phases, this suggests that such a phenomenon could exist in real glass formers. Moreover, if softened models show dynamical phase transitions, it is likely that a dynamical critical point will exist for these models as the limit of infinite softness returns an unconstrained model which is known to support only one dynamical phase.

3.4 Models

The two models that I will consider in this chapter are the softened FA and the softened east models. The so-called "hard" versions of these models were presented in Section 1.3.5.

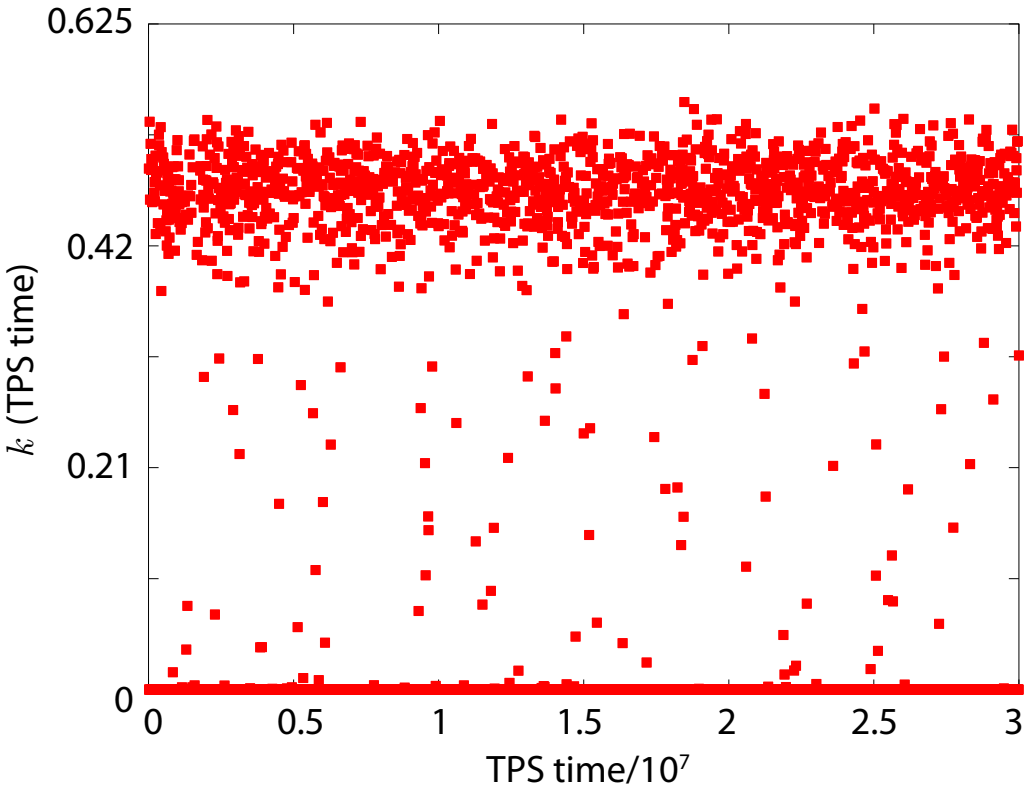

Figure 3.5: Values of $k = K/t_{\text{obs}}$ for a simulation along a TPS simulation in TPS time spanning $3 \cdot 10^7$ attempted new trajectories. Simulations spend the majority of computation time in one of two basins, an active basin with large k and an inactive basin where k is small. Many barrier crossings with intermediate values of k suggest good equilibration and ability of this data to produce a high quality $P(k)_s$.

In the hard models, the kinetic constraint function C only contained terms involving nearest neighbors. In this chapter I will change the kinetics of the model by introducing a softness parameter, ϵ, into C. The motivation behind softening KCMs is to better simulate "real" systems and to investigate if the behavior of softened KCMs describes real glass formers.

3.4.1 1 Dimensional Soft FA Model

The 1 dimensional soft FA model retains the same thermodynamics as the lattice gas introduced in Section 1.3.5. The only distinction is in the constraint function. Here, the kinetic constraint at site n_i is

$$C_{i,\text{FA}} = n_{i+1} + n_{i-1} + \epsilon \tag{3.1}$$

where ϵ represents a large activation barrier, U, such that $\epsilon \propto (-\beta U)$.

Moreover, for the soft FA model I also allow diffusive hops of an occupied site where $n_i = 1$ to an unoccupied site $n_{i\pm1} = 0$ with rate D. This does not change the behavior of our model, however, this will be required to perform an analytical mapping to a quantum phase transition to be introduced later on.

To recover the normal FA model of Section 1.3.5 one needs only to set $\epsilon = D = 0$. In the other limit, as ϵ becomes large, an unconstrained model is recovered.

3.4.2 1 Dimensional Soft East Model

The 1 dimensional soft east model retains the same thermodynamics as the lattice gas introduced in Section 1.3.5. Again, the only distinction is in the constraint function. Here, the kinetic constraint at site n_i is

$$C_{i,\text{East}} = n_{i-1} + \epsilon \tag{3.2}$$

where ϵ represents a large activation barrier, U, such that $\epsilon \propto (-\beta U)$.

To recover the normal east model introduced in Section 1.3.5 one needs only to set $\epsilon = 0$. In the other limit, as ϵ becomes large an unconstrained model is recovered.

3.4.3 Continuous Time Monte Carlo

Models which are meant to mimic supercooled liquids are usually labeled "slow". When simulating such systems using Metropolis Monte Carlo [108] one chooses any random site, i, with equal probability, and then decides whether or not to change its state with probability $C_i \cdot \min\{1, e^{-\beta\Delta E}\}$ where C_i is the constraint function at site i and $\Delta E = E_{\text{attempt}} - E_{\text{initial}}$ is the energy difference between the new, attempted configuration and the initial configuration. However, for kinetically constrained systems, $C_i e^{-\beta\Delta E}$ is often a small number – especially for "unfaciliated" moves. Therefore, many moves are rejected before a single move is accepted. To circumvent this problem, I employ continuous time Monte Carlo [108]. Instead of choosing a site with equal probability and then determining whether or not to accept the move, continuous time Monte Carlo chooses sites with probability $C_i \cdot \min\{1, e^{-\beta\Delta E}\}$ and always execute this state change. This selects sites that are more likely to have their next move be accepted with a higher probability than those most likely to have their attempt rejected. This works well for systems such as lattice models where the amount of possible subsequent states is enumerable [108]. Computationally, this requires one to keep lists of each type of move and their probabilities - which is tractable as my simulations consist of less than 10 distinct rate processes. While this adds a small amount of computational overhead, it is negligible when compared to the computation cost of rejecting many moves.

Instead of increasing the time a time step δt for every attempted move, in continuous time Monte Carlo time is advanced by randomly selecting a waiting time τ from a Poisson

distribution whose average is given by

$$\langle \tau(t) \rangle = \frac{1}{\sum_{i=1}^{N} C_i(t) \left(n_i(t) + (1 - n_i(t)) e^{-\beta} \right)} \tag{3.3}$$

where the denominator is the sum over the rates of the system, $n_i(t)$ is the current value of n_i at time t, and $\langle \tau(t) \rangle$ is the average waiting time to leave the state $\{n_i(t)\}$. Once a time is selected, it is added to the current time such that the new time becomes $t + \tau$ [108]. Time is thus continuous and "exact" as no finite time discretization is required.

3.5 The s-ensemble

In order to study the dynamical ensemble of trajectories, I define a kink κ at site i as

$$\kappa_i(t) = \left[1 - n_i(t - \delta t) \right] n_i(t) + n_i(t - \delta t) \left[1 - n_i(t) \right] \tag{3.4}$$

here, $n_i(t)$ is the occupancy $\{0, 1\}$ of site i at time t and δt is an elementary time step. Thus κ_i records whether or not a change in configuration has occured at site i at time t.

The extensive observable activity, K is simply the sum of these values of κ for the entire system over an observation time t_{obs}.

$$K = \sum_{t=0}^{t_{\text{obs}}} \sum_{i=1}^{N} \kappa_i(t) \tag{3.5}$$

here, K is an extensive dynamical order parameter. For comparison, I will often consider the intensive version of this order parameter, $k = K/(t_{\text{obs}} N)$, which is the activity per space time volume unit (where $t_{\text{obs}} \cdot N$ defines the space time volume, also known as the system size).

In this chapter I will focus on two phases defined by their average values of k. A trajectory is considered "active" for large values of k, whereas it is considered inactive when k is low. Figures 3.1 and 3.2 show cartoon versions of a trajectory for an FA and an east model respectively as well as the values of K for these examples. Examples of simulated trajectories for the FA and east models are shown in Figures 1.8 and 1.9 respectively.

In order to investigate the dynamical phase behavior of these two models, it is convenient to introduce a field s which is conjugate to K [19]. This field biases K such that as s grows K is biased to lower values, or into an "inactive" state. As s becomes negative K is biased toward larger values of K, or into an "active" state. Setting $s = 0$ recovers normal dynamics. While the field s has no known physical interpretations, it is still a useful tool in simulations to understand the behavior of the FA and east models. Moreover, it defines the equivalence of ensembles between those with fixed K and those with fixed s. For some observable A,

$\langle A \rangle_s$ is the average value of A at some value of s. The equilibrium value is given by $\langle A \rangle_0$. These expectation values are related through:

$$\langle A \rangle_s = \langle A e^{-sK} \rangle_0 \frac{1}{Z(s, t_{\text{obs}})} \tag{3.6}$$

where $Z(s, t_{\text{obs}}) = \langle \exp(-sK) \rangle_0$ is the partition function for the s ensemble. The dynamical free energy per unit time $\psi(s)$ is defined as

$$\psi(s) = \lim_{t \to \infty} \frac{1}{t_{\text{obs}}} \log Z(s, t_{\text{obs}}) \tag{3.7}$$

3.5.1 Transition Path Sampling

To sample the s-ensemble numerially, I use transition path sampling (TPS). TPS was initially developed as a method for harvesting trajectories of rare events such as barrier crossings in multi state systems [111]. The two basic moves of TPS are shooting and shifting in both the forward and backward direction. After an initial trajectory of system size N and length t_{obs} is calculated, a new trajectory is created using the procedure described in Figure 3.3. New trajectories are accepted with probability proportional to $\exp(-sK)$ – analogous to accepting and rejecting configurations with probability proportional to $\exp(-\beta E)$ where $\beta = 1/k_{\text{B}}T$ is the inverse temperature in units of Boltzmann's constant k_{B} and E is the energy in standard Monte Carlo dynamics of configurations [25].

3.6 Case Study: 1 Dimensional Soft FA Model

3.6.1 Analyzing the Soft FA Model via Master Equation

The soft FA model is a simple lattice model which can be studied analytically. To do so, I start with the master equation for the soft FA model

$$\partial_t P(\mathcal{C}, t) = -r(\mathcal{C}) P(\mathcal{C}, t) + \sum_{\mathcal{C}'} W(\mathcal{C}' \to \mathcal{C}) P(\mathcal{C}', t) \tag{3.8}$$

here, $P(\mathcal{C}, t)$ is the probability of observing a configuration $\mathcal{C}$ of the soft FA system at time t, $r(\mathcal{C}) = \sum_{\mathcal{C}'} W(\mathcal{C} \to \mathcal{C}')$ is the exit rate to leave the current configuration $\mathcal{C}$. $\mathcal{C}'$ represents all other possible configurations of the soft FA model, and $W(\mathcal{C}' \to \mathcal{C})$ is the rate to enter $\mathcal{C}$ from one of the other configurations $\mathcal{C}'$.

The soft FA model can also be represented using a spin-half representation of the master equation. I denote the ground state (where all sites $n_i = 0$) by the state $|\Omega\rangle$ where sites $\{n_i\}$ are now represented by N quantum spins. By doing so, I can represent any possible configuration $\{n_i\}$ via Pauli matrices $\sigma_i^{x,y,z}$ [119] with the raising σ_i^+ and lowering σ_i^- operators are

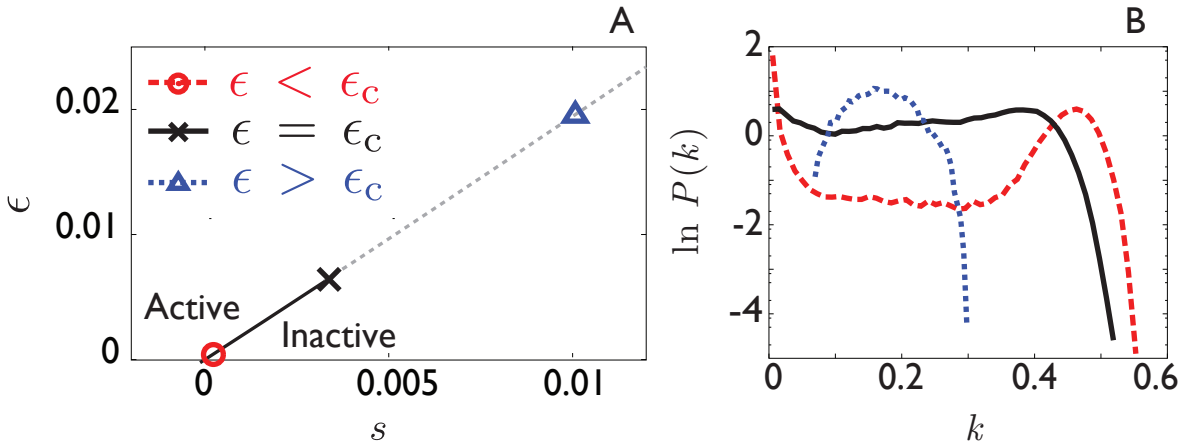

Figure 3.6: (A) Phase diagram for the $1d$ soft FA model. Here, I show the (s, ϵ) plane - varying the value of D but keeping β constant as described in the text. The solid line is the phase boundary between the active and inactive phase. The dashed line is continuation of symmetry line of Eq. 3.49 into 1 phase region beyond the critical point. The red circle indicates the point simulated with $\epsilon = 1.9 \cdot 10^{-4} < \epsilon_c$ along the coexistence line in the two phase region. The blue triangle indicates a simulation point where $\epsilon = 1.9 \cdot 10^{-2} > \epsilon_c$. The black X indicates the critical point where $\epsilon = 6.3 \cdot 10^{-3} = \epsilon_c$. (B) Coexistence histograms of the intensive activity $k = K/(Nt_{\text{obs}})$ simulations for points in (A) where colors and line styles are the same as in (A).

defined as $\sigma_i^{\pm} = \frac{1}{2}(\sigma_i^x \pm \sigma_i^y)$. Thus, a configuration in the soft FA model can be represented as

$$|\{n_i\}\rangle = \sum_{i=1}^{N} (\sigma_i^+)^{n_i} |\Omega\rangle \quad . \tag{3.9}$$

Note, that as usual I take $\sigma_i^- |\Omega\rangle = 0$. I can now construct a ket state

$$|P(t)\rangle = \sum_{\mathcal{C}} P(\mathcal{C}, t) |\mathcal{C}\rangle \tag{3.10}$$

here, $|P(t)\rangle$ represents the probability distribution of all configurations of the soft FA system occurring at time t. This allows us to rewrite the master equation given in Eq. 3.8

$$\frac{\partial}{\partial t} |P(t)\rangle = \mathbb{W} |P(t)\rangle \tag{3.11}$$

where $\mathbb{W}$ is a linear operator whose matrix elements represent the transitions rates, W, in the soft FA model. I define an operator $\mathbb{W}(s)$ whose largest eigenvalue value returns the

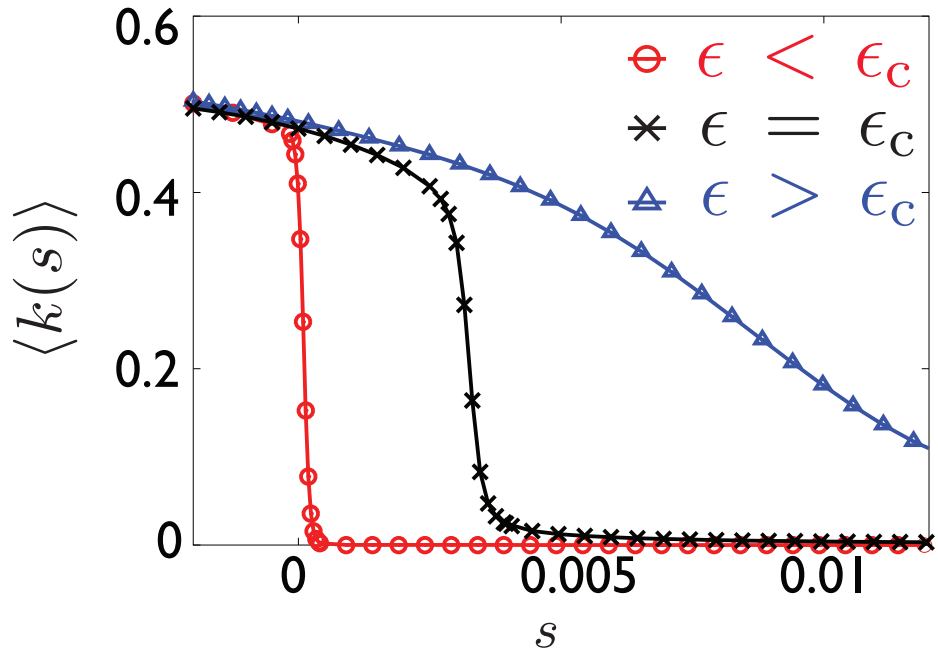

Figure 3.7: Plots of average intensive activity $\langle k \rangle = \langle K \rangle / (N t_{\rm obs})$ as a function of field s for soft FA model for various values of ϵ in the vicinity of points given in Figure 3.6 (A) for the same values of ϵ given in Figure 3.6.

dynamical free energy $\psi(s)$ as defined in Eq. 3.7. At $s = 0$, $\mathbb{W}(0)$ equals the standard linear operator $\mathbb{W}$ defined as:

$$\mathbb{W} = \sum_{\langle ij \rangle} \left\{ (\hat{n}_j + \epsilon/2)[(1 - \sigma_i^+)\sigma_i^- + e^{-\beta}(1 - \sigma_i^-)\sigma_i^+] + D[\sigma_i^+ \sigma_j^- - (1 - \hat{n}_i)\hat{n}_j] \right\} + (i \leftrightarrow j) \tag{3.12}$$

with $\langle ij \rangle$ representing a sum over distinct nearest neighbor pairs, $\hat{n}_i = \sigma_i^+ \sigma_i^-$, and $(i \leftrightarrow j)$ meaning that the previous expression needs to be symmetrized with respect to sites i and j.

In order to include the s-ensemble representation of the soft FA model I follow [120]. I write $P(\mathcal{C}, K, t)$ as the probability of being in configuration $\mathcal{C}$ at time t having already accumulated an activity K in the time between time 0 and t. I can then write the probability to be in configuration $\mathcal{C}$ at time t at a field strength s, $P(\mathcal{C}, s, t)$ as a reweighted sum over over all possible accumulated K values

$$P(\mathcal{C}, s, t) = \sum_K P(\mathcal{C}, K, t) e^{-sK} \quad . \tag{3.13}$$

The equation of motion for $|P(s,t)\rangle = \sum_{\mathcal{C}} P(\mathcal{C}, s, t)|\mathcal{C}\rangle$ becomes

$$\frac{\partial}{\partial t}|P(s,t)\rangle = \mathbb{W}(s)|P(s,t)\rangle \tag{3.14}$$

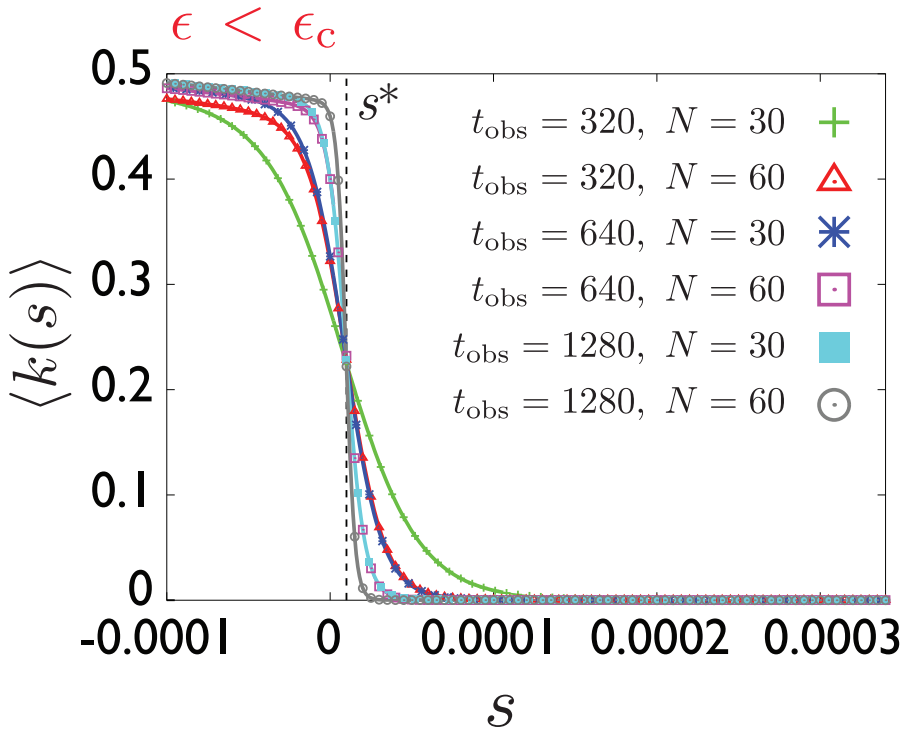

Figure 3.8: Finite size scaling of average intensive activity $\langle k \rangle = \langle K \rangle / (N t_{\text{obs}})$ as a function of field strength s for soft FA model for $\epsilon = 1.9 \cdot 10^{-4} < \epsilon_c$ for 6 different system sizes.

where now the matrix elements of $\mathbb{W}$ include the biasing field s such that

$$\mathbb{W} = \sum_{\langle ij \rangle} \{(\hat{n}_j + \epsilon/2)[(e^{-s} - \sigma_i^+)\sigma_i^- + e^{-\beta}(e^{-s} - \sigma_i^-)\sigma_i^+] + D[e^{-s}\sigma_i^+\sigma_j^- - (1 - \hat{n}_i)\hat{n}_j]\} + (i \leftrightarrow j) \tag{3.15}$$

here, the notation is the same as in Eq. 3.12 with the addition of e^{-s} modifying the rate of changes of state. Note that for the purpose of activity K, a diffusive move is treated as a single change even though diffusive moves change the state of two sites rather than one. Because the energetics of the soft FA model obey detailed balance I can write an energy function $E = \sum_i n_i$. I define an energy operator $\mathbb{E} = \sum_i \hat{n}_i$. Using this I can represent a symmetrized operator version of $\mathbb{W}$ which will be denoted $\mathbb{H}$.

$$\mathbb{H}(s) = e^{\mathbb{E}/2T} \mathbb{W} e^{-\mathbb{E}/2T} \tag{3.16}$$

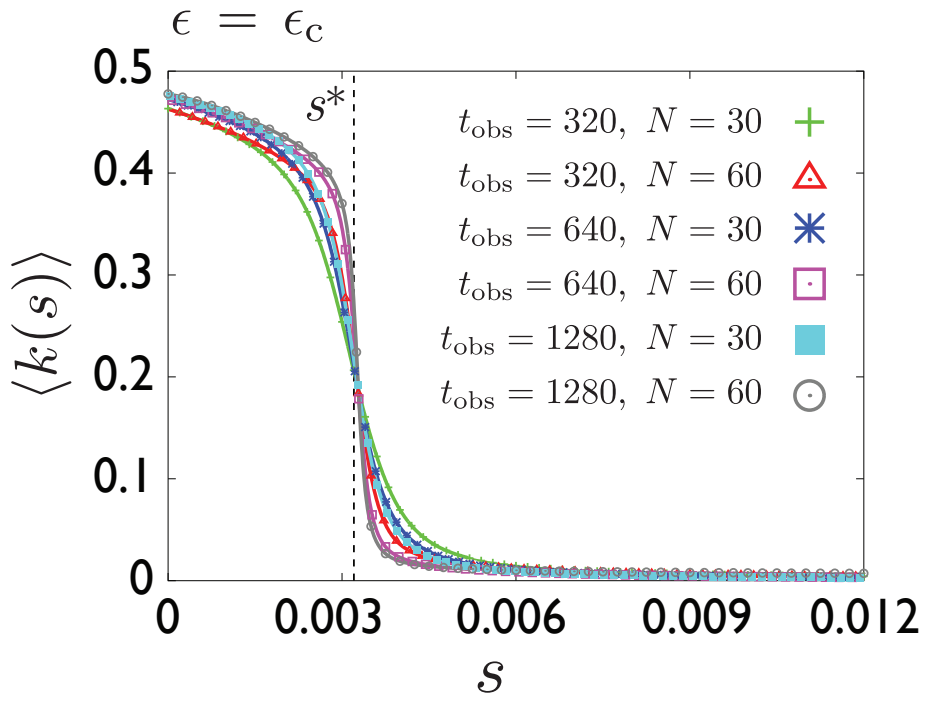

Figure 3.9: Finite size scaling of average intensive activity $\langle k \rangle = \langle K \rangle / (N t_{obs})$ as a function of field strength s for soft FA model for $\epsilon = 6.3 \cdot 10^{-3} = \epsilon_c$ for 6 different system sizes.

$$\mathbb{H}(s) = \sum_{\langle ij \rangle} \Big\{ (\hat{n}_j + \epsilon/2)[(\sqrt{e^{-1/T}} e^{-s} - \sigma_i^+)\sigma_i^- + (\sqrt{e^{-1/T}} e^{-s} - e^{-1/T}\sigma_i^-)\sigma_i^+ + D[e^{-s}\sigma_i^+\sigma_j^- - (1-\hat{n}_i)\hat{n}_j] \Big\} + (i \leftrightarrow j) \quad . \tag{3.17}$$

This new operator, $\mathbb{H}$, is now Hermitian such that

$$\langle \mathcal{C} | \mathbb{H}(s) | \mathcal{C}' \rangle = \langle \mathcal{C}' | \mathbb{H}(s) | \mathcal{C} \rangle \quad . \tag{3.18}$$

I now rewrite $\mathbb{H}$ in terms of Pauli matrices, $\sigma^{x,y,z}$ to find

$$\mathbb{H}(s) = -NC + \sum_i (h_x \sigma_i^x - h_z \sigma_i^z) + \sum_{\langle ij \rangle} \sum_{\mu\nu} \sigma_i^\mu M^{\mu\nu} \sigma_j^\mu \tag{3.19}$$

where N is the system size and

$$C = [D + (1 + e^{-1/T})(1 + \epsilon)]d/2 \tag{3.20}$$

where d is dimensionality and

$$h_x = d_z(1+\epsilon)\sqrt{e^{-1/T}} \tag{3.21}$$

$$h_z = d[2 + \epsilon - e^{-1/T}\epsilon]/2 \tag{3.22}$$

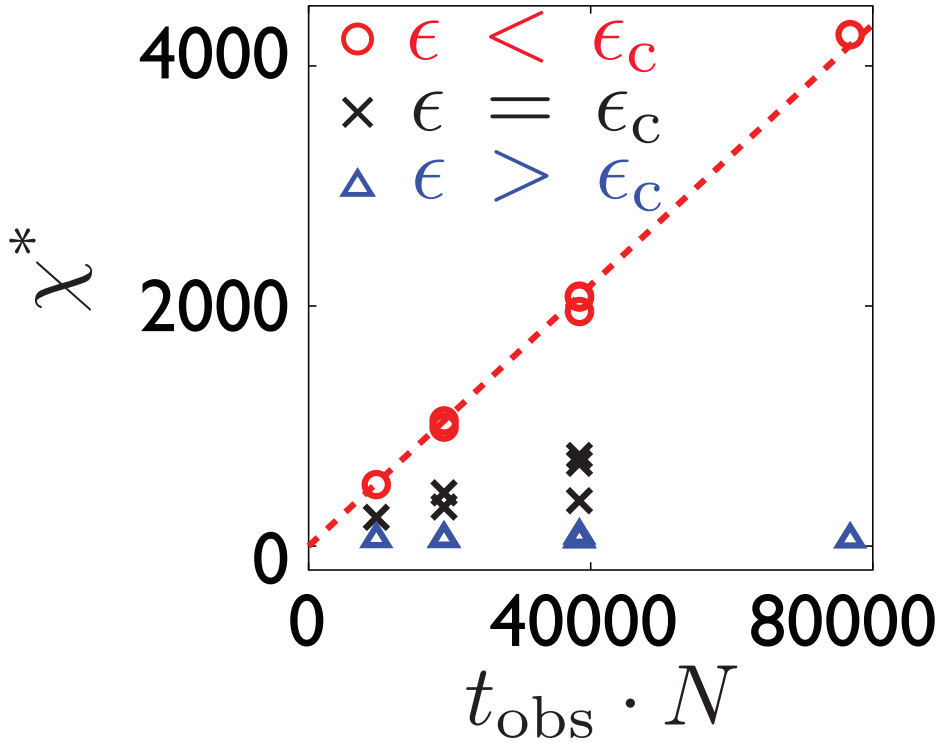

Figure 3.10: Scaling of the derivative of the activity, susceptibility, $\chi^* = -d\langle k \rangle / ds\big|_{s^*}$ for various system sizes $t_{\rm obs} \cdot N$ for $1d$ soft FA model. Labeling refers to same ϵ values as those given in 3.6. Red dashed line indicates linear scaling associated with a first order phase transition. Red circles indicate several system sizes for $\epsilon < \epsilon_c$. Black Xs indicate several system sizes for $\epsilon = \epsilon_c$. Blue triangles indicate several system sizes for $\epsilon > \epsilon_c$.

with

$$M = \frac{1}{2} \begin{pmatrix} zD & 0 & z\sqrt{e^{-1/T}} \\ 0 & zD & 0 \\ z\sqrt{e^{-1/T}} & 0 & D + e^{-1/T} - 1 \end{pmatrix}. \tag{3.23}$$

where I have used the shorthand notation $z = e^{-s}$. Then, I make a rotation of the spins with

$$R(\alpha) = e^{i\alpha \sum_j \sigma_j^y / 2} \tag{3.24}$$

such that

$$R(-\alpha) \begin{pmatrix} \sigma_i^x \\ \sigma_i^y \\ \sigma_i^z \end{pmatrix} R(\alpha) = \begin{pmatrix} \sigma_i^x \cos\alpha - \sigma_i^z \sin\alpha \\ \sigma_i^y \\ \sigma_i^z \cos\alpha + \sigma_i^x \sin\alpha \end{pmatrix} \quad . \tag{3.25}$$

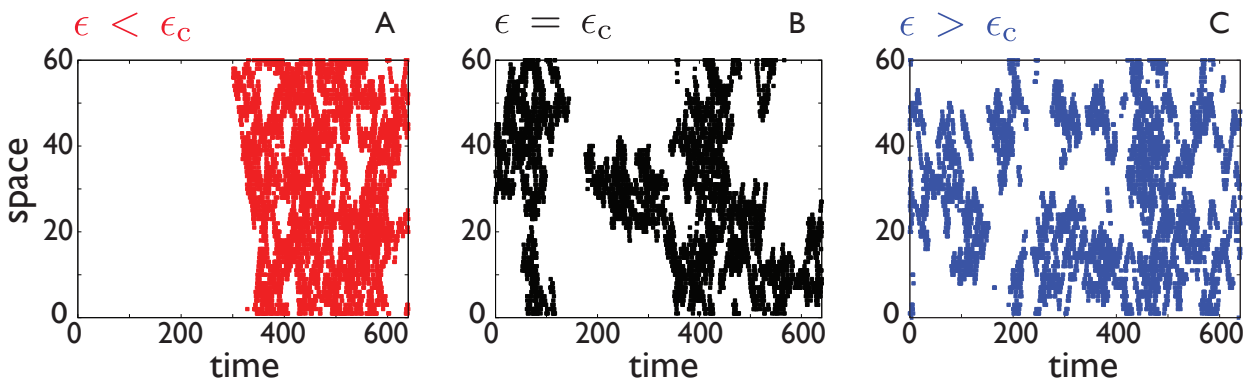

Figure 3.11: Sample trajectories for the $1d$ soft FA model taken from the same state points as in 3.6(A) from the middle of the distribution of 3.6(B). Thus, for $\epsilon \leq \epsilon_c$ these trajectories represent "transition states" between basins. Active sites are colored ($n_i = 1$) and inactive sites are white ($n_i = 0$). (A) Trajectory where $\epsilon < \epsilon_c$ with space-time phase separation. (B) Trajectory at $\epsilon = \epsilon_c$ where the phases are still identifiable but the clusters no longer have a sharp interface. (C) Trajectory at $\epsilon > \epsilon_c$ where the two phases have merged into one homogeneous phase.

I choose α

$$\tan 2\alpha = \frac{2z\sqrt{e^{-1/T}}}{1 - e^{-1/T} - D(1-z)} \tag{3.26}$$

so as to diagnolize M where

$$\mathbb{H}' \equiv R(-\alpha)\mathbb{H}R(\alpha) \tag{3.27}$$

$$= -NC + \sum_i (B\sigma_i^x - h\sigma_i^z) + \sum_{\langle ij \rangle} \sum_\mu J_\mu \sigma_i^\mu \sigma_j^\mu \quad . \tag{3.28}$$

Now,

$$B = h_x \cos\alpha - h_z \sin\alpha \tag{3.29}$$

$$h = h_z \cos\alpha + h_x \sin\alpha \tag{3.30}$$

and $J_{x,y,z}$ are the eigenvalues of the matrix M.

Note, this diagonalization makes space and time symmetric. I use this expression to avoid the symmetry breaking of the temporal boundaries described in Section 3.6.4.

3.6.2 Interpretation as Quantum Transfer Matrices

I can analyze Eq. 3.19 using a mean-field approximation, as in Ref. [53]. First, I replace the operators in 3.19 by their averages such that

$$\sigma_i^z \to 2\rho - 1 \tag{3.31}$$
$$\sigma_i^x \to 2\sqrt{\rho} \tag{3.32}$$

here, $\rho \ll 1$ is the mean density of excitations. For ease of computation, I take $D = 0$ and $e^{-1/T} \ll 1$. The result of this change gives a Landau free energy [20, 112]:

$$\mathcal{F}(\rho) = dN(2\rho + \epsilon)\left(\rho + e^{-1/T} - 2e^{-s}\sqrt{\rho e^{-1/T}}\right) \tag{3.33}$$

where $\psi(s) \geq -\min_\rho \mathcal{F}(\rho)$ is a bound to $\psi(s)$ [53, 19]. This equation, which is fourth order in $\sqrt{\rho}$, may have one or two minima. The point at which the equation transitions from having a single solution to two is the critical point. Places where there are two degenerate minima correspond to space-time coexistance along the symmetry line, Eq. 3.49. For a fixed temperature I find that the critical point $(\epsilon, s) = (2e^{-1/T}/5, \log(\sqrt{5}/2))$. with a corresponding Landau free energy

$$\mathcal{F}(\rho) = 2dN\left[\left(\sqrt{\rho} - \sqrt{e^{-1/T}/5}\right)^4 + (2e^{-1/T}/5)^2\right] \quad . \tag{3.34}$$

I can interpret $[-\mathbb{H}(s)]$ as a quantum hamiltonian. I diagonalize the matrix M via the rotation described in Eq. 3.24 and the equations that follow. I can now interpret h and B as magnetic field terms where $h > 0$, but B can have any sign. When $B = 0$, h aligns spins in the $-\sigma^z$ direction, while the ferromagnetic coupling J_x promotes ferromagnetic ordering in the $\pm\sigma^x$ directions. When $B = 0$ and J_x/h is small there is only one ground state whose average value of σ^x is 0. Contrastingly, when $B = 0$ but J_x/h is large there are two degenerate states and the symmetry between $\sigma^x \to -\sigma_x$ of $\mathbb{H}'$ is broken spontaneously. It is these two regimes which are separated by a quantum phase transition [121, 122].

There is an exact mapping [123, 124, 125] between a quantum spin system in d dimensions to a classical spin system (such as the soft FA model) in $d + 1$ dimensions [46]. First, I discretize time using small increments δt. Then, I analyze the sequence of d dimensional configurations at times $0, \delta t, 2\delta t \ldots$. Here, I interpret each configuration as a plane in the $(d + 1)$ dimensional space-time trajectory. This can be done by considering the operators $e^{\mathbb{H}(s)\delta t}$ and $e^{\mathbb{H}'(s)\delta t}$. These operators act as transfer matrices and they generate ensembles of configurations for $(d + 1)$ dimensional Ising systems. $\langle\mathcal{C}|e^{\mathbb{H}(s)\delta t}|\mathcal{C}'\rangle$ is proportional to the probability of finding the system in configuration $\mathcal{C}$ in the last time plane given that the previous plane was $\mathcal{C}'$. In order to construct the ensemble S, I take the σ^z components of the spins in $\mathcal{C}$. This gives the classical Ising spins, as in the soft FA model.

However, for the symmetrized ensemble, S' (formed via $e^{\mathbb{H}'(s)\delta t}$), I use a different mapping. Instead, I associate up (down) spins in S' with spins in $|\mathcal{C}\rangle$ that are aligned along the positive (negative) σ^x direction thus ensuring that S' retains its symmetry when the σ^x component of the $\mathbb{H}'(s)$ are inverted. Therefore, S' does not have a straightforward relationship with trajectories in the soft FA model. However, I will relate expectation values in these two ensembles using Dirac brackets in the coming sections.

Lastly, I consider the associated boundary conditions of the S' ensemble. In the d spatial dimensions of the soft FA model there are periodic boundaries, just as one would have in S'. However, in the $(d+1)^{\text{th}}$ dimension in S' the boundary conditions depend on the initial and final conditions ("planes") of the s-ensemble. These conditions are given by the initial condition of the unbiased ensemble where averages are given by $\langle . \rangle_0$ at $s = 0$. The consequences of this are described in the following section. Note that in my interpretation, I have taken the limit of large t_{obs} before that of large N which has not generally been the case [126].

In order to construct the symmetrized s-ensemble we consider an observable $F(t)$ such that the expectation value $F(t)$ is distinguishable between distinct phases. As s is changed through its coexistence value at s^* the observable goes through a sharp jump. I will now cast $F(t)$ in the S' ensemble (the symmetrized s-ensemble) and demonstrate its superiority to the unsymmetrized s-ensemble near coexistence. The expectation value of $F(t)$ can be expressed using Dirac brackets

$$\langle F(t) \rangle_s = \frac{\langle -| e^{\mathbb{W}(s)(t_{\text{obs}}-t)} \hat{F} e^{\mathbb{W}(s)t} |\text{eq}\rangle}{\langle -| e^{\mathbb{W}(s)t_{\text{obs}}} |\text{eq}\rangle} \tag{3.35}$$

here $\hat{F}$ is the operator that measures F. $\langle -|$ is a projection state such that $\langle -| = \langle \Omega | R(-\pi/2)$ and $|\text{eq}\rangle = R(2\tan^{-1} e^{-\beta})|\Omega\rangle$ is the equilibrium state.

Now, we transform the $\mathbb{W}$ operator into the $\mathbb{H}'$ operator by applying

$$\mathbb{H}' = R(-\alpha) e^{\mathbb{E}/2T} \mathbb{W}(s) e^{-\mathbb{E}/2T} R(\alpha) \tag{3.36}$$

such that $\langle F(t) \rangle_s$ becomes:

$$\langle F(t) \rangle_s = \frac{\langle \Psi | e^{\mathbb{H}'(s)(t_{\text{obs}}-t)} \hat{F}' e^{\mathbb{H}(s)t} | \Psi \rangle}{\langle \Psi | e^{\mathbb{H}'(s)t_{\text{obs}}} | \Psi \rangle} \tag{3.37}$$

where now the ket state $|\Psi\rangle = R(2\theta - \alpha)|\Omega\rangle$, $\langle \Psi|$ is now its Hermitian conjugate and $\tan\theta = \sqrt{e^{-1/T}}$

Another interpretation of this equation is that it is a transfer matrix representation of an expectation value in the S' ensemble. Thus, I can also write the numerator of equation 3.37 as

$$\sum_{\mathcal{C}_0 \ldots \mathcal{C}_M} h(\mathcal{C}_m) \left[\prod_{i=m+1}^{M-1} U(\mathcal{C}_{i+1}, \mathcal{C}_i) \right] U(\mathcal{C}_{m+1}, \mathcal{C}_m) F'(\mathcal{C}_{m+1}, \mathcal{C}_m) \left[\prod_{i=0}^{m-1} U(\mathcal{C}_{i+1}, C_i) \right] h(\mathcal{C}_0) \tag{3.38}$$

here, $\mathcal{C}_i$ are the configurations of the "planes" of the system. $M+1$ is the total number of planes where $M = t_{\rm obs}/\delta t$ and m is the current plane's index at time t where $m = t/\delta t$. $h(\mathcal{C}), U(\mathcal{C},\mathcal{C}')$, and $\hat{F}'(\mathcal{C},\mathcal{C}')$ are matrix elements of $|\Psi\rangle, e^{\mathbb{H}'(s)\delta t}$, and $\hat{F}'$. $\hat{F}'$ defines a new operator $\hat{F}' = R(-\alpha)e^{\mathbb{E}/2T}\hat{F}e^{-\mathbb{E}/2T}R(\alpha)$ corresponding to a new observable F'.

Exactly at coexistence in the soft FA model the S' ensemble is also in coexistence. Thus, $\mathbb{H}'(s)$ should be invariant under inversion of σ^x. In order for this to happen S' must be invariant under a single spin flip as well as with respect to the boundary condition along the transfer direction to ensure they do not break the symmetry in favor of one phase or another. However, for the standard s-ensemble there is a definite boundary bias. Therefore, $|\Psi\rangle$ is not invariant under inversion of σ^x since, generally, $\theta \neq 2\alpha$. This means that in this ensemble, one phase is preferred over the other for conditions at which the phases should be in coexistence.

To correct this, I define a new state that replaces $|\Psi\rangle$ and is symmetric. Thus I return to $|\Omega\rangle$ and the symmetrization is complete and takes the form:

$$\langle F(t)\rangle_{s,\rm symm} = \frac{\langle -|e^{g\sum_i \hat{n}_i}e^{\mathbb{W}(s)(t_{\rm obs}-t)}\hat{F}e^{\mathbb{W}(s)t}e^{g\sum_i \hat{n}_i}|{\rm eq}\rangle}{\langle -|e^{g\sum_i \hat{n}_i}e^{\mathbb{W}(s)t_{\rm obs}}e^{g\sum_i \hat{n}_i}|{\rm eq}\rangle} \tag{3.39}$$

where g is defined as

$$e^g = \tan(\alpha/2)/\sqrt{e^{-1/T}} \quad . \tag{3.40}$$

This now defines the expectation value of $F(t)$ in the symmerized s-ensemble. This ensemble allows more accurate characterization of phase coexistence as it removes the boundary bias otherwise imposed by the standard s-ensemble.

Moreover, for $d = 1$ there is a special case. This occurs on the *free fermion line* where $B = J_z = 0$. We use the so-called free fermion line because it is a particular mapping which allows us to solve for the critical point exactly [124] At this point, the only remaining couplings in $\mathbb{H}'(s)$ are (h, J_x, J_y). I then solve the model using a Jordan-Wigner [46, 115] transformation. I find that symmetry is broken at $h < J_x + J_y$ and the critical point occurring when $h = J_x + J_y$. This allows me to calculate the exact location of the critical point along this line by taking the determinant of M. This shows that J_z must be equal to 0. and that

$$D(D + e^{-1/T} - 1) = ze^{-1/T} \quad . \tag{3.41}$$

Solving for D returns the expression

$$D = \frac{1}{2}\left[1 - e^{-1/T} + \sqrt{(1-e^{-1/T})^2 + 4e^{-s}e^{-1/T}}\right] \quad . \tag{3.42}$$

This equation, when combined with the symmetry line (given in Section 3.6.5) can be used to solve for s^* given a value of ϵ, D, and T. This establishes the phase diagram which is shown in Figure 3.6.

3.6.3 Construction of the Field Theory

As discussed earlier, phase transitions in the soft FA model are related to symmetry breaking in Ising-like models in $d+1$ dimensions. One way to show this is to generalize the model to allow multiple occupancy, thus creating a bosonic model. This change from a fermionic to a bosonic model allows me use a Doi-Peliti [123, 125] representation. This approximation holds for smaller T because multiple occupancy in the bosonic model is energetically suppressed. See for example Ref. [120]. I write

$$\begin{aligned} W_b(s) = &\sum_{\langle ij \rangle} \Big\{ (a_i^\dagger a_i + \epsilon/2)[(z - a_j^\dagger)a_j + e^{-1/T}(a_j^\dagger - z)] + (i \leftrightarrow j) \Big\} \\ &+ D[z(a_i^\dagger a_j + a_j^\dagger a_i) - (a_i^\dagger a_i + a_j^\dagger a_j)] \end{aligned} \tag{3.43}$$

where, a_i and $a_i^\dagger$ are the bosonic operators such that $[a_i, a_j^\dagger] = \sigma_{ij}$. (D, T, ϵ) have the same interpretation as the standard, fermionic model. The density of excitations is now determined by the density of bosons given by $a_i^\dagger a^i$.

I then use the coherent state path integral to represent the average value [120]. Arriving at

$$Z(s, t_{\text{obs}}) = \int \mathcal{D}(\phi, \bar{\phi}) \exp\left(- \int \mathrm{d}^d x \mathrm{d}t L[\phi, \bar{\phi}] \right) \tag{3.44}$$

where $\phi(x,t)$ and $\bar{\phi}(x,t)$ are complex conjugate fields and

$$\begin{aligned} L(\phi, \bar{\phi}) = &\bar{\phi}\frac{\partial \phi}{\partial t} - zD\ell_0^2 \bar{\phi}\nabla^2\phi + 2dD(1-z)\bar{\phi}\phi \\ &- d(2\bar{\phi}\phi + \epsilon\ell_0^{-d})[z(\phi + e^{-1/T}\bar{\phi})\ell_0^{d/2} - (e^{-1/T} + \bar{\phi}\phi\ell_0^d)] \end{aligned} \tag{3.45}$$

here ℓ_0 is the lattice spacing in the soft FA model. Now the bosonic operators a^i and $a_i^\dagger$ have become the fields ϕ and $\bar{\phi}$ and now $\phi\bar{\phi}$ gives the density of excitations in the soft FA model. Putting this all together, I may now analyze the resulting field theory by locating the saddle points in $L[\phi, \bar{\phi}]$ or by using the variational analysis that leads to a free energy $\mathcal{F}(\phi)$, as introduced in Eq. 3.33. This allows one to identify the phase properties of the system as well as to determine the surface tensions between phases. The free energy further allows us to obtain spinodal conditions [126].

3.6.4 Boundary Biasing Condition

For the soft FA model, time and space are not symmetric in the standard s-ensemble. This is because periodic boundaries in time are not feasible. This forces a large boundary effect which causes activity to tend toward the temporal ends of the trajectory. To counteract

this boundary effect I constrain the boundary in order to symmetrize the trajectory as per Section 3.6.1. For convenience, I define a quantity α

$$\tan 2\alpha = \frac{2e^{-s}\sqrt{e^{-\beta}}}{1 - e^{-\beta} - D(1 - e^{-s})} \quad . \tag{3.46}$$

This then allows us to define the boundary term for the soft FA model:

$$g_{\text{sFA}}\left[\mathcal{N}(0) + \mathcal{N}(t_{\text{obs}})\right] = e^{\beta/2}\tan(\alpha/2)^{\mathcal{N}(0)+\mathcal{N}(t_{\text{obs}})} \tag{3.47}$$

here, $\mathcal{N}(t) = \sum_{i=1}^{N} n_i(t)$ is the number of excited sites at time t. This symmetrizes the ensembles and now the computed averages are not $\langle A\rangle_s$ as in Eq. 3.6 but rather:

$$\langle A\rangle_{s,\text{symm}} = \frac{\langle Ae^{-sK+g_{\text{sFA}}[\mathcal{N}(0)+\mathcal{N}(t_{\text{obs}})]}\rangle_0}{Z_{\text{sym}}(s, t_{\text{obs}})} \quad . \tag{3.48}$$

In the limit where the observation time t_{obs} is infinite the symmetrized boundary ensemble is equivalent to the ensemble without boundary constraints. That is, $\langle A\rangle_{s,\text{symm}} = \langle A\rangle_s$ as $t \to \infty$.

This boundary biasing condition amends the transition path sampling technique described in Section 3.5.1 as well as in Figure 3.3.

3.6.5 Symmetry Line

The soft FA model includes a symmetry line. When present, phase transitions between inactive and active phases must occur along this symmetry line. This allows us to constrain our simulations to the symmetry line because along the symmetry line the probability of observing an inactive state equals the probability of observing an active state; ie $P(\text{active}) = P(\text{inactive}) = 0.5$. This allows adequate sampling of both basins. The symmetry line is

$$\frac{1 + e^{-\beta}}{1 + \epsilon} = \sqrt{[1 - e^{-\beta} - D(1 - e^{-s})]^2 + 4e^{-\beta}e^{-2s}} - (1 - e^{-s})D \quad . \tag{3.49}$$

Given values of β, ϵ, and D this equation defines $s = s^*$, the value of the field at which the two phases have the same symmetry. In the two phase region, s^* is the field at which a phase transition occurs.

I derive this equation by noting that $\mathbb{H}'(s)$ is invariant under $\sigma_i^x \to -\sigma_i^x$ and that for J_z/h sufficiently large there is a spontaneous broken symmetry at

$$\tan\alpha = \frac{2\sqrt{e^{-1/T}}z(1 + \epsilon)}{2 + \epsilon - \epsilon e^{-1/T}} \quad . \tag{3.50}$$

Combining this equation with 3.26 I arrive at 3.49.

3.6.6 Simulation Details

To simulate the dynamics within a given trajectory in the soft FA model I use continuous time Monte Carlo [108]. Since the majority of the lattice of the soft FA model at any given time is "not facilitated", the probability of accepting moves is very low and thus simulation is slow to evolve. Continuous time Monte Carlo increases efficiency tremendously and is explained in Section 3.4.3. In order to harvest representative trajectories at a specified value of s, I use TPS as introduced in Section 3.5.1 and in Figure 3.3 with the additional boundary constraint introduced in Section 3.6.4. For ease of sampling, I constrain myself to simulations at $s = s^*$ as defined in Eq. 3.49 to collect an ensemble of trajectories to compute $P(k)_{s^*}$. Averages $\langle k(s) \rangle$ for arbitrary values of s are defined by reweighting the distribution at s^* such that

$$\int_0^{\langle k(s) \rangle} P(k')_{s^*} e^{-(s-s^*)\cdot k'} dk' = \int_{\langle k(s) \rangle}^{\infty} P(k')_{s^*} e^{-(s-s^*)\cdot k'} dk' \quad . \tag{3.51}$$

This equation is numerically valid to the extent that a wide range of k values are sampled and that s is not far from s^* such that the overlap of $P(k)_{s^*}$ and $P(k)_s$ is large.

In the two phase region, simulations are checked to ensure that there are many barrier crossings in TPS "time". TPS time is defined as the number of attempted new trajectories from the first attempted trajectory. This is analogous to normal Monte Carlo time. Trajectories close in TPS time are more correlated than those far apart in TPS time. See, for example, Figure 3.5 which shows one such ensemble of TPS trajectories. Each data point represents the $k = K/t_{\text{obs}}N$ value at the trajectory indexed by the current value of TPS time which equals the current number of attempted moves in trajectory space.

Since the critical point can be analytically computed along the free fermion line. I constrain my simulations to this line (Eq. 3.42) and choose appropriate values of D and ϵ to do so given a particular choice of temperature $\beta = 1.386$ ($e^{-\beta} = 0.25$). Under these conditions, I can determine the phase diagram exactly and use the phase diagram to inform my choice of simulation parameters to avoid sampling far from phase coexistence.

3.6.7 Numerical Results

In Figure 3.6(A), I show the phase diagram in the (ϵ, s) plane at a particular value of T with corresponding values of D chosen to follow Eq. 3.42. This is analogous to Figure 3.4(B), however I simulate at fixed T rather than fixed ϵ. The symbols represent the three simulation points demonstrated in the figures. The red circle sits on the symmetry-breaking phase boundary, the black cross indicates the critical point, and the blue triangle indicates a point that is on the symmetry line but exhibits no phase transition. In Figure 3.6(B) I show the histograms, $P(k)$ where k is the intensive kinks per space time volume $k = K/t_{\text{obs}}N$ for the points indicated in Figure 3.6(A). The red histogram ($\epsilon < \epsilon_c$) is clearly bimodal, indicating the presence of a phase transition. The black histogram ($\epsilon = \epsilon_c$) indicates the

distribution at the critical point. This distribution is broad and flat due to the diminishing surface tension. The blue histogram ($\epsilon > \epsilon_c$) shows only one phase and has an average k value in between the k values of the inactive and active phases for $\epsilon > \epsilon_c$. The bimodality at s^* for $\epsilon < \epsilon_c$ is analogous to the bimodal distribution of magnetization in a ferromagnetic model where the temperature is below the critical temperature and the magnetic field strength is set to zero.

By reweighting the histograms in 3.6(B) I can plot the value of $\langle k \rangle$ as a function of the field strength s provided that a wide range of k values can be sampled as described in Eq. 3.51. This is shown in Figure 3.7. For $\epsilon < \epsilon_c$ there is a sharp change in the average value of k as a function of s. This is analogous to the jump in magnetization of a ferromagnetic system as the magnetic field strength is varied through zero. At the critical value ϵ_c there is still a precipitous jump, but it has become rounded. For values of ϵ larger than ϵ_c the transition from a high average value of k to a low value becomes a smooth crossover.

To confirm that there is a true first order transition I measure the finite size scaling of the susceptibility at s^*, $\chi^* = -d\langle k(s) \rangle / ds|_{s=s^*}$. First, I compute $\langle k(s) \rangle$ for various system sizes (N, t_{obs}). This is shown in Figure 3.8 for $\epsilon < \epsilon_c$ and in Figure 3.9 for $\epsilon = \epsilon_c$. I plot the value of χ^* as a function of $N \cdot t_{\text{obs}}$ for $\epsilon < \epsilon_c, \epsilon = \epsilon_c$, and $\epsilon > \epsilon_c$. This is shown in Figure 3.10. For $\epsilon \leq \epsilon_c$ the scaling is linear with system size. For a first order transition $\chi^* = (\Delta k)^2 N t_{\text{obs}}/2$, where Δk is the size of the discontinuity in $\langle k(s) \rangle$ at the s^*. At $\epsilon = \epsilon_c$ the dependence of the susceptibility on the system size is weaker, but still scales with system size. However, for $\epsilon > \epsilon_c$ the susceptibility χ^* levels out and does not increase with increased system size.

I also show sample trajectories with k values from the middle of the distributions of 3.6(B) in Figure 3.11. Here, the trajectories contain approximately the same number of kinks but they are distributed in varying ways. Figure 3.11(A) shows a trajectory taken from the transition state where $\epsilon < \epsilon_c$. Here, there is a clear minimized surface between the "inactive" part of the trajectory on the left hand side of the plot and the "active" part of the trajectory on the right hand side. This is consistent with the system minimizing surface tension at a first order phase transition. For Figure 3.11(B) a trajectory taken from the middle of the distribution where $\epsilon = \epsilon_c$ is shown. Here, there are still two distinct phases but the surface tension has gone to zero so the cluster of "activity" spans the entire system. Finally, for Figure 3.11(C) a trajectory is shown from the middle of the distribution where ϵ is beyond the critical point. Here in the supercritical regime, the two phases have combined to form one, homogenous phase with no phase separation.

3.7 Case Study: 1 Dimensional Soft East Model

The soft east model is a simple lattice model which can be studied analytically much in the same way as the soft FA model. To do so, I start with the master equation for the soft

east model

$$\partial_t P(\mathcal{C},t) = -r(\mathcal{C})P(\mathcal{C},t) + \sum_{\mathcal{C}'} W(\mathcal{C}' \to \mathcal{C})P(\mathcal{C}',t) \quad . \tag{3.52}$$

Again, $P(\mathcal{C},t)$ is the probability of observing a configuration $\mathcal{C}$ of the soft east system at time t. $r(\mathcal{C}) = \sum_{\mathcal{C}'} W(\mathcal{C} \to \mathcal{C}')$ is the exit rate to leave the current configuration $\mathcal{C}$, $\mathcal{C}'$ represents all other possible configurations of the soft FA model and $W(\mathcal{C}' \to \mathcal{C})$ is the rate to enter $\mathcal{C}$ from one of those other configurations $\mathcal{C}'$.

The soft east model can also be represented using a spin-half representation of the master equation. I denote the ground state (where all sites $n_i = 0$) by the state $|\Omega\rangle$ where sites $\{n_i\}$ are now represented by N quantum spins. By doing so, I can represent any possible configuration $\{n_i\}$ via Pauli matrices $\sigma_i^{x,y,z}$ [119] with the raising σ_i^+ and lowering σ_i^- operators are defined as $\sigma_i^{\pm} = \frac{1}{2}(\sigma_i^x \pm \sigma_i^y)$ Thus, a configuration in the soft east model can be represented as

$$|\{n_i\}\rangle = \sum_{i=1}^{N} (\sigma_i^+)^{n_i} |\Omega\rangle \quad . \tag{3.53}$$

Note that as usual I take $\sigma_i^-|\Omega\rangle = 0$. I can now construct a ket state

$$|P(t)\rangle = \sum_{\mathcal{C}} P(\mathcal{C},t)|\mathcal{C}\rangle \tag{3.54}$$

here, $|P(t)\rangle$ represents the probability distribution of all configurations of the soft east system occurring at time t. This allows us to rewrite the master equation given in Eq. 3.52

$$\frac{\partial}{\partial t}|P(t)\rangle = \mathbb{W}|P(t)\rangle \tag{3.55}$$

where $\mathbb{W}$ is a linear operator whose matrix elements represent the transitions rates, W, in the soft east model. I define an operator $\mathbb{W}(s)$ whose largest eigenvalue value returns the dynamical free energy $\psi(s)$ as defined in Eq. 3.7. At $s = 0$, $\mathbb{W}(0)$ equals the bare linear operator $\mathbb{W}$ defined as:

$$\mathbb{W} = \sum_i (\hat{n}_{i-1} + \epsilon)[(1 - \sigma_i^+)\sigma_i^- + e^{-\beta}(1 - \sigma_i^-)\sigma_i^+] \quad . \tag{3.56}$$

This equation bears much resemblance to Eq. 3.12, however it does not contain the symmetrized portion ($i \leftrightarrow j$) – as the east model is inherently asymmetric - nor the diffusive portion of the equation because there is no convenient mean field mapping that would require such a form. Furthermore, the diffusive moves would destroy the hierarchical barriers of the east model.

In order to include the s-ensemble representation of the soft east model I follow [120]. I write $P(\mathcal{C},K,t)$ as the probability of being in configuration $\mathcal{C}$ at time t having already accumulated an activity K in the time between time 0 and t. I can then write the probability

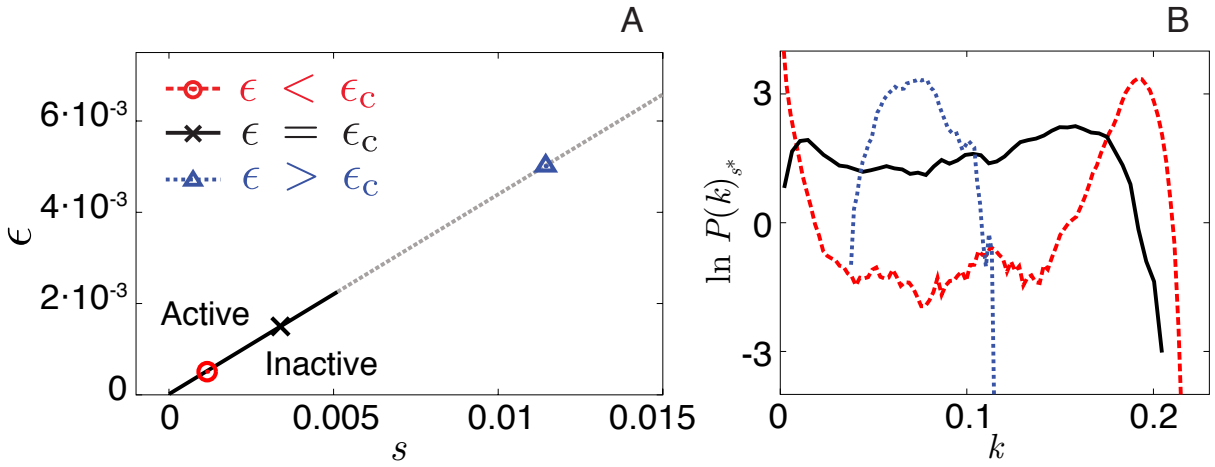

Figure 3.12: (A) Phase diagram for the $1d$ soft east model. Here, I show the (s, ϵ) plane - varying the value of D but keeping β constant as described in the text. The solid line is the phase boundary between the active and inactive phase. The dashed line is continuation of symmetry line of Eq. 3.73 into 1 phase region beyond the critical point. The red circle indicates a point simulated with $\epsilon = 5 \cdot 10^{-4} < \epsilon_c$ along the coexistence line in the two phase region. The blue triangle indicates a simulation point where $\epsilon = 5 \cdot 10^{-3} > \epsilon_c$. The black X indicates a point near the critical point where $\epsilon = 1.5 \cdot 10^{-3} \approx \epsilon_c$. Analytical mapping of the soft east model is not available as in the FA model, and thus the exact location of the critical point along the symmetry line is estimated here but is not exactly known. (B) Coexistence histograms of the intensive activity $k = K/(Nt_{\text{obs}})$ simulations for points in (A) where colors and line styles are the same as in (A).

to be in configuration $\mathcal{C}$ at time t at a field strength s, $P(\mathcal{C}, s, t)$ as a reweighted sum over over all possible accumulated K values

$$P(\mathcal{C}, s, t) = \sum_K P(\mathcal{C}, K, t) e^{-sK} \quad . \tag{3.57}$$

The equation of motion for $|P(s,t)\rangle = \sum_{\mathcal{C}} P(\mathcal{C}, s, t)|\mathcal{C}\rangle$ becomes

$$\frac{\partial}{\partial t}|P(s,t)\rangle = \mathbb{W}(s)|P(s,t)\rangle \tag{3.58}$$

where now the matrix elements of $\mathbb{W}$ include the biasing field s such that

$$\mathbb{W} = \sum_i (\hat{n}_{i-1} + \epsilon)[(e^{-s} - \sigma_i^+)\sigma_i^- + e^{-\beta}(e^{-s} - \sigma_i^-)\sigma_i^+] \tag{3.59}$$

here, the notation is the same as in Eq. 3.56 with the addition of e^{-s} modifying the rate of changes of state. Because the energetics of the soft east model obey detailed balance I can

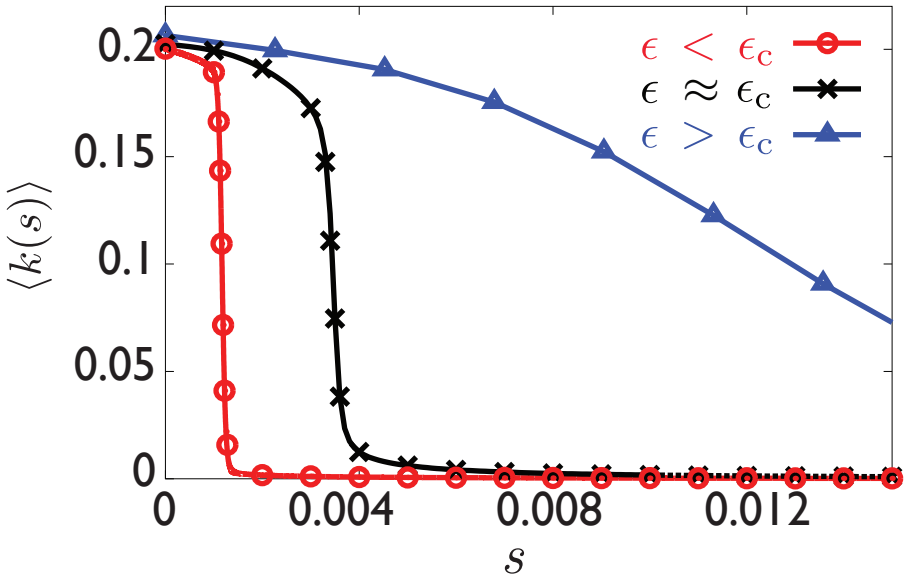

Figure 3.13: Plots of average intensive activity $\langle k \rangle = \langle K \rangle / (N t_{\text{obs}})$ as a function of field s for soft east model for various values of ϵ in the vicinity of points given in Figure 3.12 (A) for the same values of ϵ given in Figure 3.12.

write an energy function $E = \sum_i n_i$. I define an energy operator $\mathbb{E} = \sum_i \hat{n}_i$. Using this I can represent a symmetrized operator version of $\mathbb{W}$ which I denote $\mathbb{H}$.

$$\mathbb{H}(s) = e^{\mathbb{E}/2T} \mathbb{W} e^{-\mathbb{E}/2T} \tag{3.60}$$

$$= \sum_i (\hat{n}_{i-1} + \epsilon)[(\sqrt{e^{-1/T}} e^{-s} - \sigma_i^+)\sigma_i^- + (\sqrt{e^{-1/T}} e^{-s} - e^{-1/T}\sigma_i^-)\sigma_i^+] \tag{3.61}$$

This new operator, $\mathbb{H}$, is now Hermitian such that

$$\langle \mathcal{C} | \mathbb{H}(s) | \mathcal{C}' \rangle = \langle \mathcal{C}' | \mathbb{H}(s) | \mathcal{C} \rangle \quad . \tag{3.62}$$

I now rewrite $\mathbb{H}$ in terms of Pauli matrices, $\sigma^{x,y,z}$ to find

$$\mathbb{H}(s) = -NC + \sum_i (h_x \sigma_i^x - h_z \sigma_i^z) + \sum_{\langle ij \rangle} \sum_{\mu\nu} \sigma_i^\mu M^{\mu\nu} \sigma_j^\mu \tag{3.63}$$

where N is the system size and

$$C = (1 + e^{-1/T})(1 + 2\epsilon)d/2 \tag{3.64}$$

where d is dimensionality and

$$h_x = d_z(1 + 2\epsilon)\sqrt{e^{-1/T}} \tag{3.65}$$

$$h_z = d[2 + \epsilon - e^{-1/T} 2\epsilon]/2 \tag{3.66}$$

with

$$M = \frac{1}{2}\begin{pmatrix} 0 & 0 & z\sqrt{e^{-1/T}} \\ 0 & 0 & 0 \\ z\sqrt{e^{-1/T}} & 0 & e^{-1/T}-1 \end{pmatrix}. \tag{3.67}$$

where I have used the shorthand notation $z = e^{-s}$. Next, I make a rotation of the spins with

$$R(\alpha) = e^{i\alpha}\sum_j \sigma_j^y/2 \tag{3.68}$$

such that

$$R(-\alpha)\begin{pmatrix} \sigma_i^x \\ \sigma_i^y \\ \sigma_i^z \end{pmatrix} R(\alpha) = \begin{pmatrix} \sigma_i^x\cos\alpha - \sigma_i^z\sin\alpha \\ \sigma_i^y \\ \sigma_i^z\cos\alpha + \sigma_i^x\sin\alpha \end{pmatrix} \quad . \tag{3.69}$$

I choose α

$$\tan 2\alpha = \frac{2z\sqrt{e^{-1/T}}}{1-e^{-1/T}} \quad . \tag{3.70}$$

This expression diagnolizes M such that

$$\mathbb{H}' \equiv R(-\alpha)\mathbb{H}R(\alpha) \tag{3.71}$$

$$= -NC + \sum_i (B\sigma_i^x - h\sigma_i^z) + \sum_{\langle ij\rangle}\sum_\mu J_\mu \sigma_i^\mu \sigma_j^\mu \tag{3.72}$$

where now,

$$B = h_x\cos\alpha - h_z\sin\alpha$$
$$h = h_z\cos\alpha + h_x\sin\alpha$$

and $J_{x,y,z}$ are the eigenvalues of the matrix M.

Note, this diagonalization makes space and time symmetric. I use this expression to avoid the symmetry breaking of the temporal boundaries described in Section 3.7.2.

3.7.1 Symmetry Line

As in the soft FA model there is a hidden symmetry in the soft east model where the probabilities of being in either the inactive or active phases are equal. In other words, that $P(\text{active}) = P(\text{inactive}) = 0.5$. The line is given by

$$\frac{1+e^{-\beta}}{2\epsilon+1} = \sqrt{(1-e^{-\beta})^2 + 4e^{-\beta}e^{-2s^*}} \quad . \tag{3.73}$$

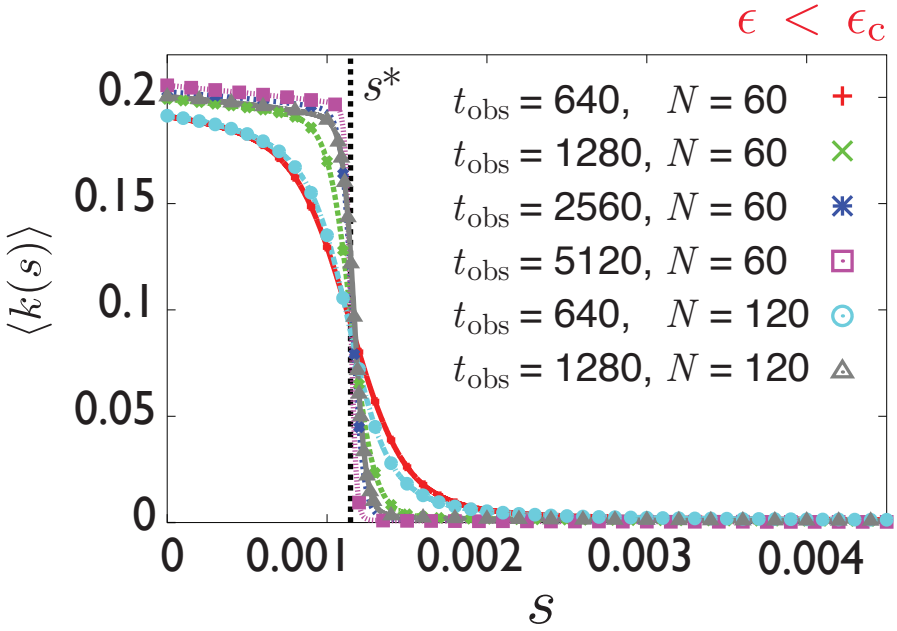

Figure 3.14: Finite size scaling of average intensive activity $\langle k \rangle = \langle K \rangle / (N t_{\text{obs}})$ as a function of field strength s for soft east model for $\epsilon = 5 \cdot 10^{-4} < \epsilon_c$ for 6 different system sizes.

I derive in this equation by noting that $\mathbb{H}'(s)$ is invariant under $\sigma_i^x \to -\sigma_i^x$, therefore, if symmetry is broken it must occur when

$$\tan \alpha = \frac{\sqrt{e^{-1/T}} z (1 + 2\epsilon)}{1 + \epsilon - \epsilon e^{-1/T}} \quad . \tag{3.74}$$

Combining this equation with 3.70, I arrive at 3.73.

3.7.2 Boundary Biasing Condition

As in the soft FA model, time and space are not symmetric in the standard s-ensemble for the soft east model. This is because periodic boundaries in time are not feasible. This causes a large boundary effect which forces activity to tend toward the temporal ends of the trajectory. To counteract this boundary effect I constrain the boundary in order to symmetrize the two dimensions as per the previous section. For convenience, I define a quantity ϑ

$$\sin \vartheta = 2 e^{-2s} \sqrt{\frac{e^{-\beta}}{(1 + e^{-\beta})^2} + 4 (e^{-2s} - 1) e^{-\beta}} \quad . \tag{3.75}$$

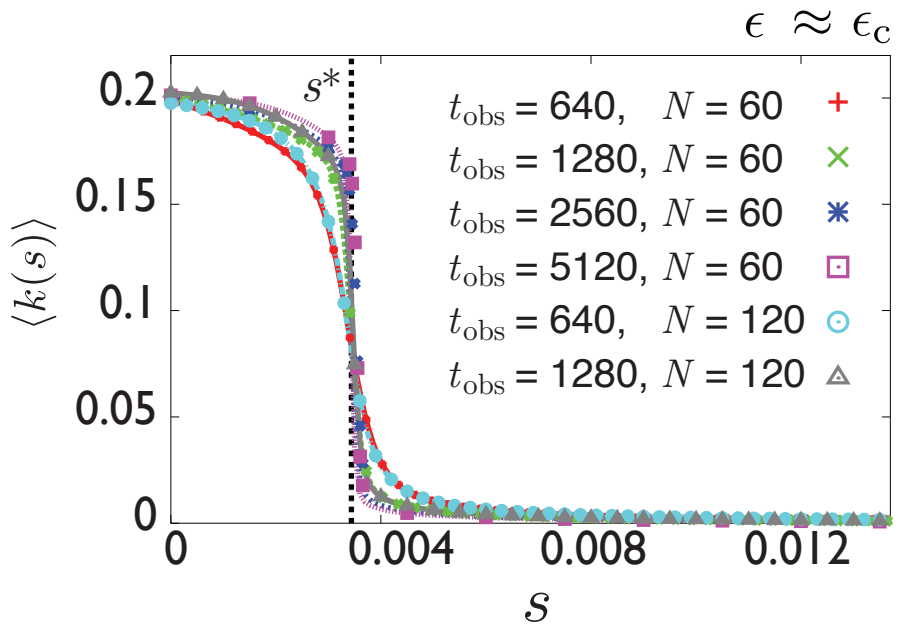

Figure 3.15: Finite size scaling of average intensive activity $\langle k \rangle = \langle K \rangle / (N t_{\text{obs}})$ as a function of field strength s for soft FA model for $\epsilon = 1.5 \cdot 10^{-3} \approx \epsilon_c$ for 6 different system sizes.

This then allows us to define the boundary term for the soft east model:

$$g_{\text{sEast}}(\mathcal{N}(0) + \mathcal{N}(t_{\text{obs}})) = e^{\beta/2} \tan(\vartheta/4)^{\mathcal{N}(0)+\mathcal{N}(t_{\text{obs}})} \tag{3.76}$$

here, $\mathcal{N}(t) = \sum_{i=1}^{N} n_i(t)$ is the number of excited sites at time t. This symmetrizes the ensembles and now the computed averages are not $\langle A \rangle_s$ as in Eq. 3.6 but rather:

$$\langle A \rangle_{s,\text{symm}} = \frac{\langle A e^{-sK + g_{\text{sEast}}[\mathcal{N}(0)+\mathcal{N}(t_{\text{obs}})]} \rangle_0}{Z_{\text{sym}}(s, t_{\text{obs}})} \quad . \tag{3.77}$$

In the limit where the observation time t_{obs} is infinite, the symmetrized boundary ensemble is equivalent to the ensemble without boundary constraints. That is, $\langle A \rangle_{s,\text{symm}} = \langle A \rangle_s$ as $t \to \infty$.

This boundary biasing condition amends the transition path sampling technique described in Section 3.5.1 and in Figure 3.3.

3.7.3 Simulation Details

To simulate the dynamics within a given trajectory in the soft east model I use continuous time Monte Carlo [108]. Since the majority of the lattice of the soft FA model at any given

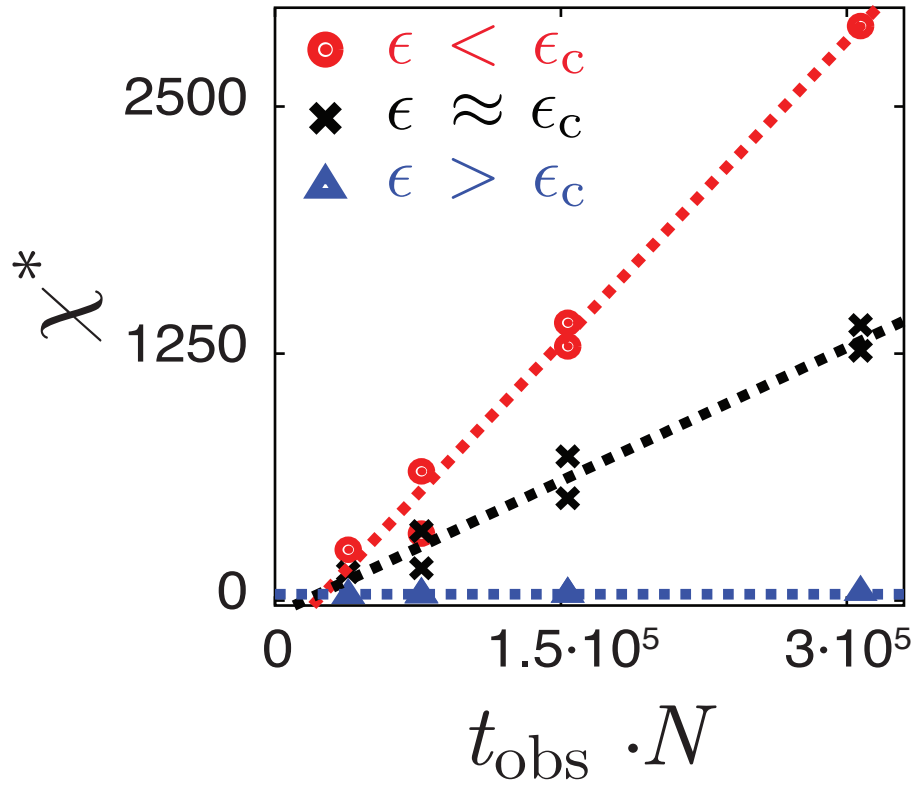

Figure 3.16: Scaling of the derivative of the activity, susceptibility, $\chi^* = -d\langle k \rangle / ds\big|_{s^*}$ for various system sizes $t_{\text{obs}} \cdot N$ for $1d$ soft east model. Labeling refers to same ϵ values as those given in 3.12. Red dashed line indicates linear scaling associated with a first order phase transition. Similarly, black dashed line represents linear scaling near the critical point. Blue dashed line indicates constant value of susceptibility across all values of system size for $\epsilon > \epsilon_c$. Red circles indicate several system sizes for $\epsilon < \epsilon_c$. Black Xs indicate several system sizes for $\epsilon \approx \epsilon_c$. Blue triangles indicate several system sizes for $\epsilon > \epsilon_c$.

time is "not facilitated", the probability of accepting moves is very low and thus simulation is slow to evolve. Continuous time Monte Carlo increases efficiency tremendously and is explained in Section 3.4.3. In order to harvest representative trajectories at a value of s I use transition path sampling (TPS) as introduced in Section 3.5.1 and in Figure 3.3 with the additional boundary constraint introduced in Section 3.7.2. For ease of sampling, I constrain myself to simulations at $s = s^*$ as defined in Eq. 3.73, thus computing $P(k)_{s^*}$. Averages, $\langle k(s) \rangle$ for arbitrary values of s are defined by reweighting the distribution at s^* such that

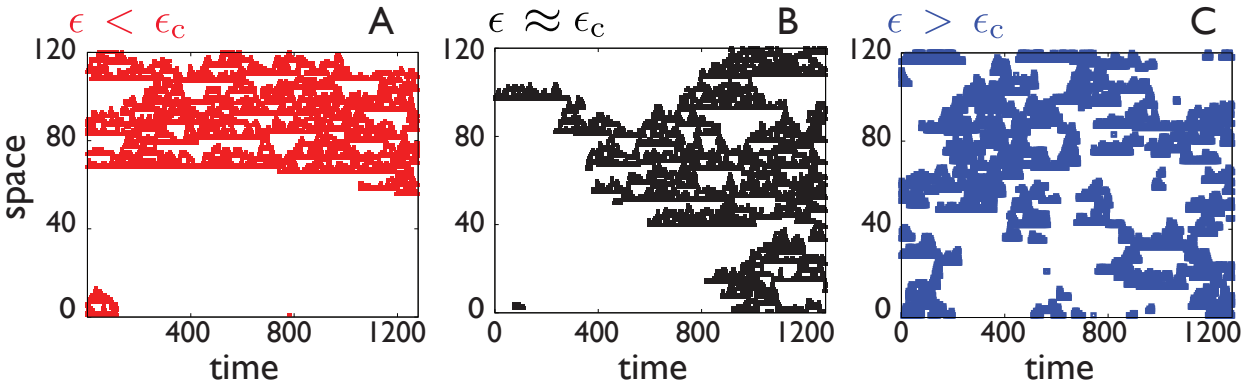

Figure 3.17: Sample trajectories for the $1d$ soft east model taken from the same state points as in 3.12(A) from the middle of the distribution of 3.12(B). Thus, for $\epsilon \leq \epsilon_c$ these trajectories represent "transition states" between basins. Active sites are colored ($n_i = 1$) and inactive sites are white ($n_i = 0$). (A) Trajectory where $\epsilon < \epsilon_c$ with space-time phase separation. (B) Trajectory at $\epsilon \approx \epsilon_c$ where the phases are still identifiable but the clusters no longer have a sharp interface. (C) Trajectory at $\epsilon > \epsilon_c$ where the two phases have merged into one homogeneous phase.

$$\int_0^{\langle k(s)\rangle} P(k')_{s^*} e^{-(s-s^*)\cdot k'} dk' = \int_{\langle k(s)\rangle}^{\infty} P(k')_{s^*} e^{-(s-s^*)\cdot k'} dk' \quad . \tag{3.78}$$

This equation is numerically valid to the extent that a wide range of k values are sampled and that s is not far from s^* such that the overlap of $P(k)_{s^*}$ and $P(k)_s$ is large.

As in the FA model, in the two phase region, simulations are checked to ensure there are many barrier crossings in TPS time. See for example Figure 3.5 which shows one such TPS simulation and Section 3.6.6 which goes into further detail regarding TPS time.

Unlike in the soft FA model, the soft east model cannot be mapped onto a quantum phase transition via a convenient mean field theory. Therefore, although the symmetry line can still be computed, the exact location of the critical point along the symmetry line cannot be determined analytically and is only estimated here. I simulate the soft east model at constant inverse temperature, $\beta = 0.75$.

3.7.4 Numerical Results

In Figure 3.12(A), I show the phase diagram in the (ϵ, s) plane at fixed T and corresponding values of D to follow Eq. 3.42. This is analogous to Figure 3.4(B), however, I simulate at fixed T rather than fixed ϵ. The symbols represent the three simulation points demonstrated in the figures. The red circle sits ($\epsilon < \epsilon_c$) on the symmetry-breaking phase boundary, the black cross when $\epsilon \approx \epsilon_c$ indicates a point near the critical point, and the blue triangle when

$\epsilon > \epsilon_c$ indicates a point that is on the symmetry line but exhibits no phase transition. In Figure 3.12(B) I show the histograms, $P(k)$ where k is the intensive kinks per space time volume $k = K/t_{\text{obs}}N$ for the points indicated in Figure 3.12(A). Note that the red histogram ($\epsilon < \epsilon_c$) is clearly bimodal indicating the presence of phase transition. The black histogram ($\epsilon \approx \epsilon_c$) indicates the histogram at the critical point. This distribution is broad and flat due to the diminishing surface tension. The blue histogram ($\epsilon > \epsilon_c$) indicates only one phase which has an average k value in between the k values of the inactive and active phases. The bimodality at s^* for $\epsilon < \epsilon_c$ is analogous to the bimodal distribution of magnetization in a ferromagnetic model where the temperature is below the critical temperature and the magnetic field strength is set to zero.

By reweighting the histograms in 3.12(B) I can plot the value of $\langle k \rangle$ as a function of the field strength s provided that a wide range of k values can be sampled as described in Eq. 3.78. This is shown in Figure 3.13. For $\epsilon < \epsilon_c$ there is a sharp change in the average value of k as a function of s. This is analogous to the jump in magnetization of a ferromagnetic system as the magnetic field strength is varied through zero. At the critical value of ϵ, ϵ_c, there is still a precipitous jump, but it has become rounded. For values of ϵ larger than ϵ_c the transition from a high average value of k to a low becomes a smooth crossover.

To confirm that there is a true first over transition I measure the finite size scaling of the susceptibility at s^* $\chi^* = -d\langle k(s) \rangle / ds|_{s=s^*}$. First, I compute $\langle k(s) \rangle$ for various system sizes (N, t_{obs}). This is shown in Figure 3.14 for $\epsilon < \epsilon_c$ and in Figure 3.15 for $\epsilon \approx \epsilon_c$. I plot the value of χ^* as a function of $N \cdot t_{\text{obs}}$ for $\epsilon < \epsilon_c, \epsilon \approx \epsilon_c$, and $\epsilon > \epsilon_c$. This is shown in Figure 3.16. For $\epsilon \leq \epsilon_c$ the scaling is linear with system size. For a first order transition, $\chi^* = (\Delta k)^2 N t_{\text{obs}}/2$ where Δk is the jump in $\langle k(s) \rangle$ at the phase transition. At $\epsilon \approx \epsilon_c$ I expect that the dependence of the susceptibility on the system size is weaker, but still scales with system size. However, for $\epsilon > \epsilon_c$ the susceptibility χ^* levels out and does not increase with increased system size.

I also show sample trajectories with k values from the middle of the distributions of 3.12(B) in Figure 3.17. Here, they contain approximately the same number of kinks but they are distributed in varying ways. Figure 3.17(A) shows a trajectory taken from the transition state where $\epsilon < \epsilon_c$. Here, there is a clear minimized surface between the "inactive" part of the trajectory on the bottom half of the plot and the "active" part of the trajectory in the upper half. This is consistent with the minimization of the surface tension indicative of a first order phase transition. For Figure 3.17(B) a trajectory taken from the middle of the distribution where $\epsilon \approx \epsilon_c$ is shown. Here, there are still two distinct phases but the surface tension has decreased so that the cluster of "activity" spans the entire system. Finally, for Figure 3.17(C) a trajectory is shown from the middle of the distribution where ϵ is beyond the critical point. Here in the supercritical regime, the two phases have combined to form one, homogenous phase with no phase separation.

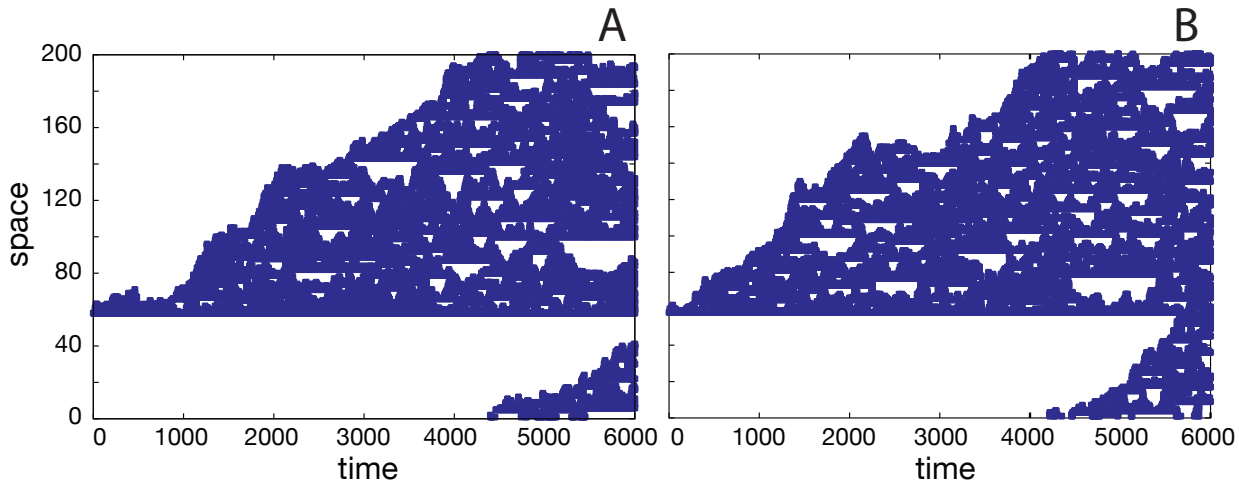

Figure 3.18: Two examples of trajectories nucleating the active phase from the inactive phase in an east model with $\beta = 1$ and $N = 200$. Initial conditions are set such that there is only one initial excitation $\sum_{i=1}^{N} n_i = 1$ at time $t = 0$ corresponding to the equilibrium phase for s larger than 0. The system is then allowed to evolve under $s = 0$. Blue squares indicate structure where $n_i = 1$.

3.8 Nucleating Activity from the Inactive Phase

We watch a system - prepared in an inactive state at $s > s^*$ - nucleate the active phase at $s = 0$. In Figure 3.18 I show the east model (with $\epsilon = 0$) at $T = 1$ nucleating from an inactive state with only one excitation in the entire trajectory. Figure 3.18(A) shows a trajectory whose growth towards the active state seems at first gradual, but then takes off precipiticously at about $t = 1000$, whereas Figure 3.18(B) shows a trajectory whose growth is more immediately but goes through an apparent plateau around $t = 2000$. I define two waiting times. First, is the time from the beginning of the trajectory to first arrive at 5 excitations, that is $\sum_i n_i = 5$ denoted t_5. I also define a second waiting time which is the time it takes to arrive at $\sum_i n_i = cN$ where N is the system size and $c = \langle n_i \rangle_{\beta, s=0}$ the average concentration of excitations at $s = 0$ at a given value of inverse temperature, β. I denote this waiting time as t_{w} - the waiting time to arrive at the active state.

I have fit these distributions of waiting times using a Γ distribution of the form:

$$P(t_a) = t_a^{k_a - 1} \frac{e^{-t_a/\theta}}{\Gamma(k_a)\theta_a^k} \tag{3.79}$$

here, t_a is the waiting time to arrive at some condition "a" – for example a certain number of excitations or to arrive at an equilibrium concentration. Where, k_a and θ_a are fit parameters and $\Gamma(n) = (n-1)!$ is the gamma function. The Γ distribution is often used to model

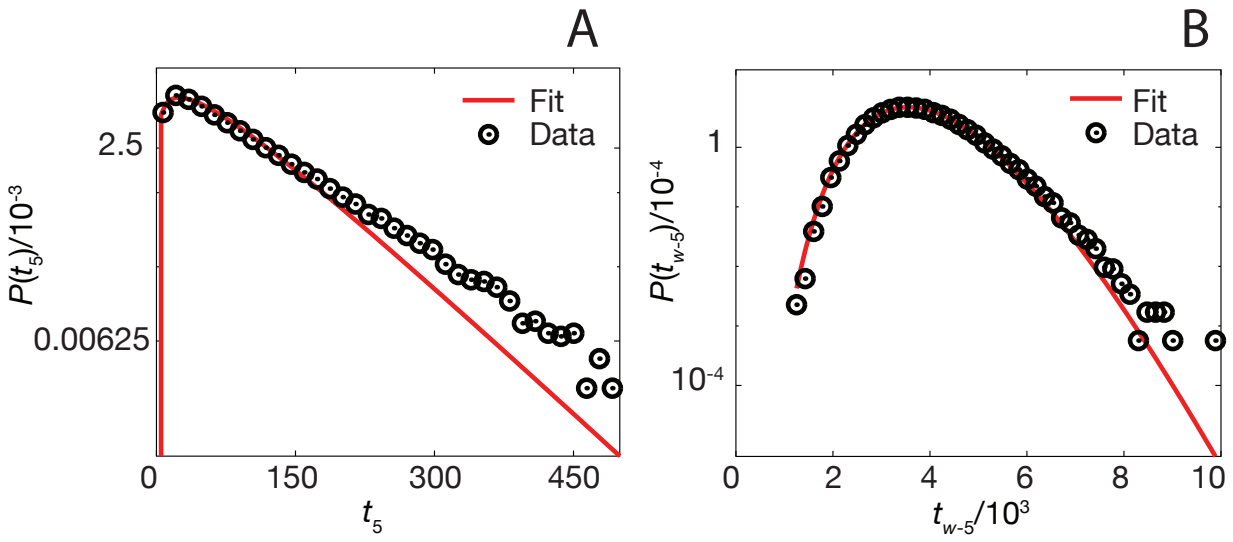

Figure 3.19: Gamma distributions $\Gamma(x)$ for t_5 (A) and $t_{\mathrm{w}-5}$ (B) for an east model with $\beta = 1$ and $N = 200$. Black circles are computed distribution from data, red line is fit using equation 3.79. Fit parameters for (A) are $k_5 = 1.67$ and $\theta_5 = 36.1$. Fit parameters for (B) are $k_{\mathrm{w}-5} = 18.7$ and $\theta_{\mathrm{w}-5} = 200$.

waiting times with the interpretation that k is the number of independent events and θ is the average time between these events (assuming the random variables are equally spaced in time, on average) [127]. Figure 3.19 shows the distributions and resultant Γ distribution fits to data for t_5 as well as $t_{\mathrm{w}-5} = t_{\mathrm{w}} - t_5$ for a system with $N = 200$ and $\beta = 1$.

While the Γ distribution appears to capture dynamics near the peak of the distribution, there is a significant fat tail which appears exponential towards the long time end of the distribution as seen in Figure 3.19. This suggests that the assumption of independent events with equally spaced waiting times breaks down for these long times. More work needs to be done to further explore this break down from independent, Poisson statistics.

Figure 3.20 shows fit parameter trends for the fitted Γ distributions. I find that t_5 (whose fit parameters are k_5 and θ_5) has no system size dependence, only T dependence. k_5 appears to decrease exponentially with increasing β whereas θ_5 increases exponentially with increasing β. This suggests that, while slightly fewer processes are needed to nucleate the first five excitations as temperature is decreased, the average length of these processes is longer. On the other hand, for fits of $P(t_{\mathrm{w}-5})$ the fit parameters $k_{\mathrm{w}-5}$ and $\theta_{\mathrm{w}-5}$ do depend on the system size. Roughly speaking $\theta_{\mathrm{w}-5}$ does not change with system size, but only with temperature whereas $k_{\mathrm{w}-5}$ grows exponentially with increasing N. That suggests that in order to reach a certain absolute number of excitations more events are required which have approximately the same average time between them corresponding with the growing diffusion of the excitation front through the system.

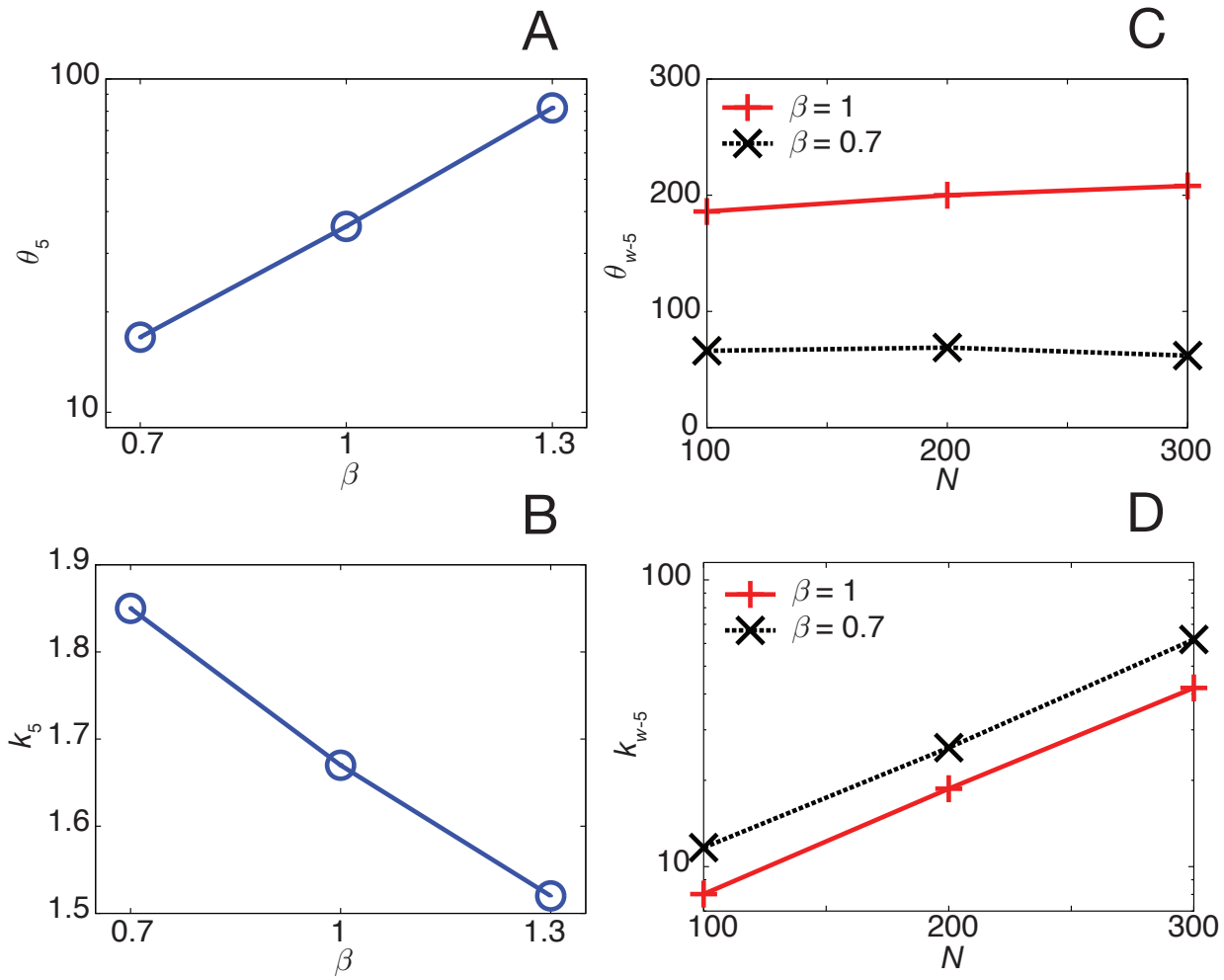

Figure 3.20: Trends for fits of $\Gamma(x)$ with respect to system size and temperature where $\beta = 1/T$ for an east model nucleating from a state with only a single excitation. Symbols indicate computed fit values and lines are guides to the eye. (A) θ_5 as a function of inverse temperature β. (B) k_5 as a function of inverse temperature β. (C) $\theta_{\mathrm{w}-5}$ as a function of system size N for two values of temperature. (D) $k_{\mathrm{w}-5}$ as a function of system size N for two values of temperature.

At $s = 0$ nucleating the active phase from the inactive phase appears to grow relatively unencumbered as the active phase is downhill in free energy from the inactive state. However, as the system approaches the thermodynamic limit the amount of independent processes needed to nucleate the phases grows exponentially. Moreover, as temperature decreases, the time between independent events increases precipitously – from about $\theta_{\mathrm{w}-5} \approx 75$ for $\beta = 0.7$ to $\theta_{\mathrm{w}-5} \approx 200$ for $\beta = 1$.

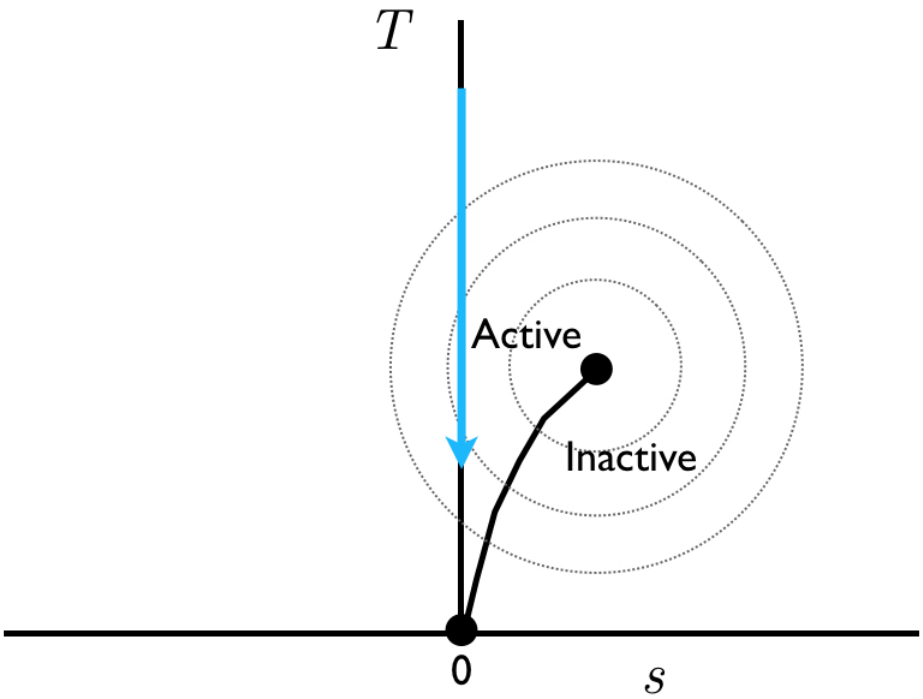

Figure 3.21: Imagined cooling protocol of a glass former in the T and s plane as in 3.4(B). Real-world dynamics occurs along the $s = 0$ line. A material is cooled along the blue arrow. As it approaches the supercooled regime in the vicinity of the critical point and first order lines, fluctuations of the inactive phase within the active phase become larger (indicated by dotted circles).

3.9 Implications to the Glass Transition

The two critical points I have uncovered appear only when the kinetic constraints in the FA and east models are softened. They do not appear in the "hard" versions of these models. Moreover, they occur only for $s > 0$ when $\epsilon > 0$. Despite the lack of experimental methods to access dynamical regions where $s \neq 0$, the critical points still have implications for natural systems. To illustrate this, I will return to the analogy of the ferromagnetic system.

Below its critical temperature, a ferromagnetic spontaneously orders under a small magnetic field. One phase dominates and becomes the "majority phase" (say in an Ising model the "up" phase). However, one observes small fluctuations in the majority phase of the minority phase (the "down" phase). Dynamic heterogeneities may be a consequence of the same fluctuation phenomenon. The dominant fluctuations in the active supercooled liquid state are those of the inactive space-time phase which I have identified herein. If this is true, then the probability of observing inactive behavior in a given region of space-time is prescribed by several factors: The spatiotemporal extent of the region, the surface tension, and

the free energy difference between dynamical phases. In the unbiased equilibrium dynamics, one expects the main contributions to this probability to be of the form [19]

$$P(\ell^d, \tau) \propto \exp(-\Gamma_1 \tau - \Gamma_2 \ell^d - \Delta\Psi \ell^d \tau) \tag{3.80}$$

here, ℓ^d and τ are the spatial and temporal extents of the inactive domains, $\Gamma_{1,2}$ are the surface tensions, and $\Delta\Psi$ is the free energy difference between the active and inactive phases evaluated at $s = 0$.

Previously, it has been shown that for KCMs [128] such as the hard east and hard FA models ($\epsilon = s = 0$), coexistence occurs exactly along the natural dynamics and the phase diagram is consistent with Figure 3.4 such that $\Delta\Psi = 0$ for these hard models at $s = 0$. However, for the soft FA and soft east models, this is not the case. In these models $s^* > 0$ when $\epsilon > 0$ and thus $\Delta\Psi > 0$. Therefore, observing large dynamical heterogeneities in the system is determined by the space-time surface tensions and free energies. In it important to note that by simply defining $P(\ell^d, \tau)$ this assumes the existence of two dynamical phases. On the other hand, one may still use a mean field spinodal condition analogy between the classical spin system to estimate whether the minority (inactive) space-time phase is stable enough to form fluctuation domains within the stable majority active phase, as is the case in an Ising ferromagnet.

Figure 3.21 highlights this point. Imagine a cooling procedure whereby a liquid is cooled slowly toward a supercooled liquid along the real world dynamics at $s = 0$. For high temperatures, there is only a single, active phase – the simple liquid. As the system is cooled, a second phase – the inactive phase – comes into existence for temperatures below the critical temperature at the critical point (where $s > 0$). However, whether one can observe this second phase at $s = 0$ depends on whether or not the majority phase can support significant fluctuations of the inactive phase. In Figure 3.21 this is visualized by the circles which emanate from the critical point and the first order phase line causing large fluctuations of the minority phase in the majority phase.

For my soft models, we can understand these fluctuations via mean-field arguments. Using the theoretical picture presented here, $\Gamma_{1,2}$ and $\Delta\Psi$ are the key numerical values that determine the size of and nature of dynamical heterogeneities in supercooled liquids.

Furthermore, Figure 3.21 makes a connection between this work and other scenarios for the glass transition. If cooling in a supercooled liquid is analogous to reducing both T and ϵ in the soft FA model (I expect the quantity U to be a constant, material dependent property), then I expect the dynamical free-energy difference as well as the surface tension between the two phases to vanish at $T \to 0$. This would correspond to a zero-temperature ideal glass transition for a liquid [129]. These transitions are known to be accompanied by increased dynamic heterogeneity because the probability of large regions of the minority, inactive phase increases as described in Eq. 3.80.

Additionally, if a glass former supports a finite-temperature ideal glass transition similar to those found in spin glasses [130, 131] one expects that the dynamical free-energy difference and surface tension should vanish at this point [132]. Moreover, if glass formers do

support space-time phase transitions in the presence of a nonzero field s (as suggested by several groups [132, 133, 134]), this does not imply the existence of any finite-temperature thermodynamic transition – but it also does not preclude it.

Finally, in the softened models as shown in Figure 3.4(B) the first order phase line terminates in a critical point. Thus, in the soft models the two phases must share the same symmetry - much in the way of a liquid and a gas and unlike the first order line between a fluid and a crystalline solid (for which a critical point is forbidden) [25]. In a molecular system, it is not known whether the inactive phase is a true amorphous solid that spontaneously breaks translational symmetry or rather a yet-to-be-observed liquid phase with an extremely large (but finite) relaxation time. In the first case the critical point shown in 3.4(B) is forbidden by symmetry, and if any line of transitions occurs it must separate the two phases for all conditions in the (s, T) plane. However, in the case of the yet-to-be-observed slow liquid phase the critical point found here could be relevant with the (active)liquid-(inactive)liquid transition [135, 136] being a non-equilibrium transition.

Chapter 4

Future Work

4.1 Decoupling of Transport Properties

As described in Section 1.2.2, the Stokes-Einstein relation breaks down when there are larger and larger dynamic fluctuations. One thing that remains to be checked is to see how well the onset temperature T_o of the parabolic fit correlates to the decoupling of the relaxation time and the self-diffusion constant.

In Ref. [137], Ediger *et al* considered two liquids: OTP and tNB (as defined in Chapter 2). For tNB (shown in Figure 1.4) the onset temperature is about 527 K, whereas the decoupling begins around 425 K. For OTP the onset temperature is around 365 K, whereas decoupling becomes dramatic at 285 K. The anecdotal evidence for these two liquids suggests that decoupling becomes pronounced at temperatures about 20% lower than T_o. The reason for this seems puzzling and requires a more careful examination of glass former data.

Moreover, Chandler-Garrahan theory makes another prediction based on KCMs [49] that $D_s \sim \tau^{-\xi}$. Where ξ is a constant estimated to be between 0.66-0.95 depending on the KCM model and dimensionality [29]. This implies that $\log D_s$ still follows a parabolic form as per Eq. 1.27 but with a prefactor different from J. Moreover it implies that $\log D_s$ as a function of $\log \tau$ or $\log \eta$ should follow a straight line. This has been illustrated by Mallamace *et al* in Ref. [18] for many of the same glass formers I have considered [1] in their Figure 3 with $\xi \approx 0.85$ - well within the range predicted from KCMs. Therefore, since I have shown in Chapter 2 that these fragile glass formers follow a parabolic form, if $\log \tau$ and $\log D_s$ are linearly related then D_s must also follow a parabolic form.

4.2 Measuring Dynamical Facilitation

4.2.1 Introduction

One pertinent question in understanding the microscopic origin of supercooled liquid phenomena is the role of dynamical facilitation. As introduced in Chapter 1, dynamical facilitation refers to the idea that local structural rearrangements or excitations allow for the birth and death of excitations nearby in space [35]. The role of dynamic facilitation in various theoretical scenarios of the glass transition varies widely – in the picture of Garrahan and Chandler (GC), structural relaxation follows entirely from the facilitated motion of excitations and the superposition of such dynamics leads to the formation of excitations on longer length and time scales, resulting in dynamical heterogeneity [138]. Whereas in other theories [139], dynamic facilitation plays an important, although non-central, role. Determining the extent to which dynamic facilitation describes microscopic particle dynamics is therefore an important factor distinguishing between different theories of supercooled liquids and the glass transition and describing dynamical heterogeneity.

Several past studies have attempted to directly measure dynamic facilitation in atomistic supercooled liquids. Glotzer and coworkers [140, 141] provided evidence for dynamical facilitation in the context of string-like motion and demonstrated an increasing effect of facilitation with decreasing temperature, as predicted by GC theory. Candelier, Biroli and coworkers [21, 22] have studied facilitation in the context of simulations, and reported that dynamic facilitation is only present over a small temperature range and disappears with decreasing temperature near the jamming or glass transition. These apparently contradictory results stem from the lack an agreed-upon method for measuring dynamic facilitation in an unequivocal way

Our aim is to determine a measurement of dynamic facilitation that can be applied to both simulations as well as granular and colloidal experiments. In order to do so, we will study kinetically constrained models (KCMs) and compare to recent measurements in atomistic systems [50]. Dynamical facilitation is an inherent component of KCMs, so we can be certain that methods applied to such models can detect dynamic facilitation unambiguously. Furthermore, we will test the avalanche clustering method of Candelier *et al* [22] and likely others [140]. In order to be a valid measurement of dynamic facilitation, the methods must be able to detect an increase in dynamic facilitation with decreasing temperatures in KCMs as they are constructed this way by design. If these methods fail to detect these behaviors, that would suggest that any measurements in atomistic simulations or experiments is too ambiguous to measure dynamic facilitation in any meaningful way.

We propose an alternative method for measuring dynamic facilitation and quantifying its role based on recent attempts to do so in atomistic simulations of binary mixtures [50]. Moreover, we believe that the measurements of Candelier *et al* are simply reworkings of exchange and persistence time distributions (as they are known in KCMs) and do not demonstrate any new measurement [29].

4.2.2 Models & Simulation

In order to test my measurements of dynamic facilitation I will consider two models, the crossover model already introduced in Chapter 1 as well as the arrow model. I will review the crossover model and introduce the arrow model here.

Kinetically constrained models (KCMs) are a set of simple models whose thermodynamics are trivial, but whose dynamical constraints produce interesting supercooled liquid-like behavior. These models are inherently facilitated based on their specific set of rules as all other relaxation processes are forbidden [35, 45].

The two most basic of these models are the one dimensional east model [48] and the one dimensional Fredrickson-Andersen (FA) model [46]. Relaxation in the FA Model is 'diffusive' as there is only one characteristic barrier relaxation – the Arrhenius barrier [35]. The FA model, thus, is a good model for strong glass formers [35]. The east model [48] is similar to the FA model except that the constraint function only contains a term in one direction. Sites facilitate their neighbors to their "east" and the east model relaxing hierarchically – that is to say that there is no single characteristic barrier because the barriers are a function of distance between sites ℓ [35]. The east model is a good model for fragile dynamics [47].

Most glass formers' behavior falls in between that of the east and the FA model. To interpolate between these two extremes, we define the 1 dimensional crossover model as a generalization of the east and FA models [49]. In the crossover model, the underlying thermodynamics is that of a lattice gas [25]. The one dimensional lattice gas is a model with N sites labeled $i = 1, 2, \ldots, N$. Each lattice site can take on one of two values $n_i = \{0, 1\}$. In the context of Chandler-Garrahan theory, the interpretation is that at site i where $n_i = 0$, the glass former is in an unexcited state and cannot facilitate neighboring regions to relax. A region which contains an excitation, where $n_i = 1$, can facilitate neighboring regions to relax. Lattice sites do not interact energetically. The total energy, E, of the system is given by the sum of the lattice occupancy

$$E = \sum_{i=1}^{N} n_i \quad . \tag{4.1}$$

The equilibrium concentration $c = \langle n_i \rangle$ of these excitations at inverse temperature $\beta = 1/k_{\mathrm{B}}T$ is given by:

$$c = \langle n_i \rangle = \frac{1}{1 + e^{\beta}} \quad . \tag{4.2}$$

The crossover model is distinguished from an unconstrained model by its dynamical rules. In an unconstrained model, at some time t any site can change state with some finite rate [25] proportional to the detailed balance condition

$$\frac{k_{0\to1}}{k_{1\to0}} = e^{-\beta} \tag{4.3}$$

here, $k_{0\to1}$ is the rate a site where $n_i = 0$ becomes excited into a state where $n_i = 1$. $k_{1\to0}$ is the reverse process where n_i goes from an excited state to an unexcited state where $n_i = 0$. For an unconstrained model, we will take $k_{0\to1} = e^{-\beta}$ and $k_{1\to0} = 1$, though, as we will see in the crossover model, any rates which preserve the ratio in Eq. 4.3 are acceptable rate choices.

Unlike in an unconstrained model, in KCMs only some sites are capable of changing states at time t. These rules take into account the ideas of facilitation.

In the crossover model, sites where $n_i = 1$ can facilitate relaxation in either adjacent lattice site n_{i-1} or n_{i+1}. This introduces a *constraint* function C_i into the rate expressions. For the crossover model the constraint function is:

$$C_{i,\mathrm{x}} = \varepsilon n_{i+1} + n_{i-1} + \epsilon \tag{4.4}$$

here, we have included a term that allows for a violation of the kinetic constraints, ϵ, where $\epsilon = \exp(-\beta U)$ and U is a large barrier to violating the constraints and β is the inverse temperature in units where Boltzmann's constant (k_B) is set to unity. $\epsilon = 0$ defines the "hard" version of all the following models, whereas $\epsilon > 0$ defines a "softened" version of these models. "Softened" models are meant to mimic the less black-and-white nature of molecular glass formers where it has been suggested that some excitations appear out of the bulk without explicit facilitation [21, 22]. Generally we will take $\epsilon = 0$ or very small. ε (distinct from ϵ) is an interpolating parameter that ranges from 0 to 1. $\varepsilon = 0$ returns the east model [48]. $\varepsilon = 1$ returns the FA model [46]. For the crossover model the rates become

$$k_{0\to1} = e^{-\beta} C_{i,\mathrm{x}} \tag{4.5}$$

$$k_{1\to0} = C_{i,\mathrm{x}} \tag{4.6}$$

Since the detailed balance condition in Eq. 4.3 is preserved, the thermodynamics are unchanged. The difference between the unconstrained model and the crossover model is entirely *dynamical*.

Another simple kinetically constrained model that was considered by Garrahan and Chandler [35] is the 2-dimensional arrow model. The arrow model is the analog of the 1-dimensional crossover model in higher dimensions. The arrow model retains the thermodynamics of a simple lattice gas - that is that there are no energetic neighbor-neighbor interactions - but adds dynamic facilitation in a set of rules similar to those in the crossover model. Unlike the crossover model which is anisotropic for $\varepsilon \neq 1$, the arrow model is isotropic under all conditions.

The motivation for the arrow model comes from considering a fluid where space is divided into square regions whose lengths are comparable to (but no smaller than) bulk correlation lengths. Therefore, equilibrium fluctuations in adjacent cells are uncorrelated. We then discretize time into steps δt such that δt is sufficiently long to discriminate if mobility has occurred in a site in the interval δt. We take an empty cell to be a location at which there can be no activity in time δt, whereas a filled site supports an arrow and is a location where there

is the possibility of rearrangement. The arrow supported by the filled site is antiparallel to the direction of motion and thus indicates the direction of facilitation. The interpretation of arrows as locations where there is a defect in the mobility field is distinct from the original paper [35] where they interpreted a filled site as a location where rearrangement could be detected in a real glass former, rather than a location where there was an underlying defect where rearrangement can (but not certainly) be observed. This distinction will play an important role in the implications for our results in real glass formers and represents a shift in the theory supporting dynamic facilitation - though it does not change the basic findings and predictions of Chandler-Garrahan theory.

Since this type of coarse-graining can be done on any system, in as sense it is an exact course graining with no approximations. In an ordinary fluid, where dynamics is rapid and homogenous we expect a typical configuration of the coarse grain arrow lattice to be completely occupied, whereas in a supercooled liquid with dynamic heterogeneity the occupancy of arrows is low. For such a supercooled liquid, the thermodynamics of the arrow model are that of a lattice gas (as in the crossover model). We take one approximation to the coarse-graining - that the facilitation arrows are constrained to lie on one of the four diagonals of the square lattice site. Using diagonal as opposed to edge based arrows allows for a cone of influence with positive angle, ie that an arrow can facilitate a neighbor site if the dot product between the arrow and the the vector connecting the two neighbor sites is positive.

Mathematically, the arrow model contains N^2 sites where N is the length of each spatial extent. The occupancy and arrow field is described by $\mathbf{n}(\vec{x}) = n(\vec{x})\mathbf{v}(\vec{x})$ where $n(\vec{x}) = 1$ or 0 at location $\vec{x}$ depending on if there is an underlying defect in the mobility field in that cell ($n(\vec{x}) = 1$) or not ($n(\vec{x}) = 0$). $\mathbf{v}(\vec{x})$ is the unit vector pointing in the direction of facilitation of cell $\vec{x}$. For 2 dimensions, $\mathbf{v}(\vec{x})$ can be one of four vectors $(\pm 1, \pm 1)/\sqrt{2}$ where we have set the lattice spacing to unity. As in the crossover model we denote the equilibrium concentration of excitations as $c = \langle n(\vec{x})\rangle$ where $\langle . \rangle$ indicates an equilibrium ensemble average. Since $\langle \mathbf{v}(\vec{x})\rangle = 0$ the system is isotropic (unlike the east model). Furthermore, for $\vec{x} \neq \vec{y}$, $\langle \mathbf{n}(\vec{x})\mathbf{n}(\vec{y})\rangle = 0$ such that there are only trivial equal time correlation functions. The equilibrium distribution for the vector field is $P(\{\mathbf{n}(\vec{x})\}) = \prod_{\vec{x}} \rho(\mathbf{n}(\vec{x}))$ where

$$\rho(\mathbf{n}) = g^{-n}(1-c)^{1-n}c^n \tag{4.7}$$

where g is the number of degeneracy of the equally likely arrow orientations (in 2 dimensions, $g = 4$). Between time step t and $t + \delta t$ the arrow model proceeds via single site Monte Carlo dynamics. Consider a transition at site $\vec{x}$ of the vector field $\mathbf{n}(\vec{x}) = n(\vec{x})\mathbf{v}(\vec{x})$ from being in an unexcited state ($n(\vec{x}) = 0$) to and from an excited state ($n(\vec{x}) = 1, \mathbf{v}(\vec{x}) = \mathbf{w}$) where $\mathbf{w}$ is one of the g possible arrow directions.

$$\mathbf{n}(\vec{x}) = \mathbf{0} \underset{k_{\mathrm{B}}}{\overset{k_{\mathrm{f}}}{\rightleftharpoons}} \mathbf{n}(\vec{x}) = \mathbf{w} \tag{4.8}$$

where $k_{\mathrm{f}} = C_{\vec{x}}[\mathbf{w}]c/g$ and $k_{\mathrm{B}} = C_{\vec{x}}[\mathbf{w}](1-c)$ are the forward and backwards rates. Here, $C_{\vec{x}}$

represents the kinetic constraint given by

$$C_{\vec{x}}[\mathbf{w}] = f\left[1 - \prod_{\langle \vec{y},\vec{x}\rangle}(1 - \delta_{\sqrt{d}(\vec{x}-\vec{y})\cdot\mathbf{n}(\vec{y}),1})\right] + (1-f)\left[1 - \prod_{i-1}^{d}(1 - \delta_{\mathbf{n}(\vec{x}-\sqrt{d}\mathbf{w}_i),\mathbf{w}}\right] + \epsilon \tag{4.9}$$

here, $\mathbf{w}_i$ is the ith Cartesian component of $\mathbf{w}$, and the first product is over nearest neighbor sites denoted by $\langle \vec{y}, \vec{x}\rangle$, d is the dimensionality, and ϵ allows for unfacilitated moves as introduced in the description of the crossover model. $\delta_{a,b}$ is the Kronecker delta function where $\delta_{a,b} = 1$ if $a = b$ and 0 otherwise. $C_{\vec{x}}[\mathbf{w}]$ does not depend on the current state of the site making the transition, only on the state of its nearest neighbors thus preserving the detailed balance condition of Eq. 4.8 with respect to the distribution defined in Eq. 4.7. $f \in [0, 1]$ determines the probability $p(f)$ that the newly created arrow will be parallel to its facilitation arrow such that $p(f) = [1 + f(g - 1)]^{-1}$. When $f = 1$ an excitation pointing in any direction can be created or destroyed if it is facilitated by a neighbor (FA-like). On the other end, if $f = 0$ only arrows parallel to its facilitating neighbors can be created or destroyed (east-like).

The dynamics of the arrow model obey time-reversal symmetry as well as detailed balance. The arrow model is most realistic for small concentrations of excitations, c in the vicinity of dynamical arrest for glass forming materials.

c and f have both energetic and entropic contributions. As described earlier, when c is small excitations are uncorrelated. Therefore, for c small, -ln(c/g) is proportional to β. Similarly, for real systems, $f = ac^b$ where a is an entropic contribution and b defines an energetic contribution [35].

4.2.3 Dynamics of KCMs

Since KCMs are lattice models, their structure is that of the underlying lattice gas and is composed at any particular time, t, of the values of $\{n_i(t)\}$. On the other hand, the dynamics is governed by kinks. Where a kink κ at site i at time t corresponds to a structural change from $0 \leftrightharpoons 1$ is defined as

$$\kappa_i(t) = [1 - n_i(t - \delta t)]\, n_i(t) + n_i(t - \delta t)\, [1 - n_i(t)] \tag{4.10}$$

where δt is an elementary computational time step and the operator $\kappa = 0$ if no kink has occurred at time t and $\kappa = 1$ if a change in configuration has occurred.

Facilitation is mostly propagated through long lived excitations, or sites where $n_i = 1$ for long periods of time as this allows for the system to explore many configurations. These correspond to defects in the mobility field. The interpretation is that a site where $n_i = 1$ has

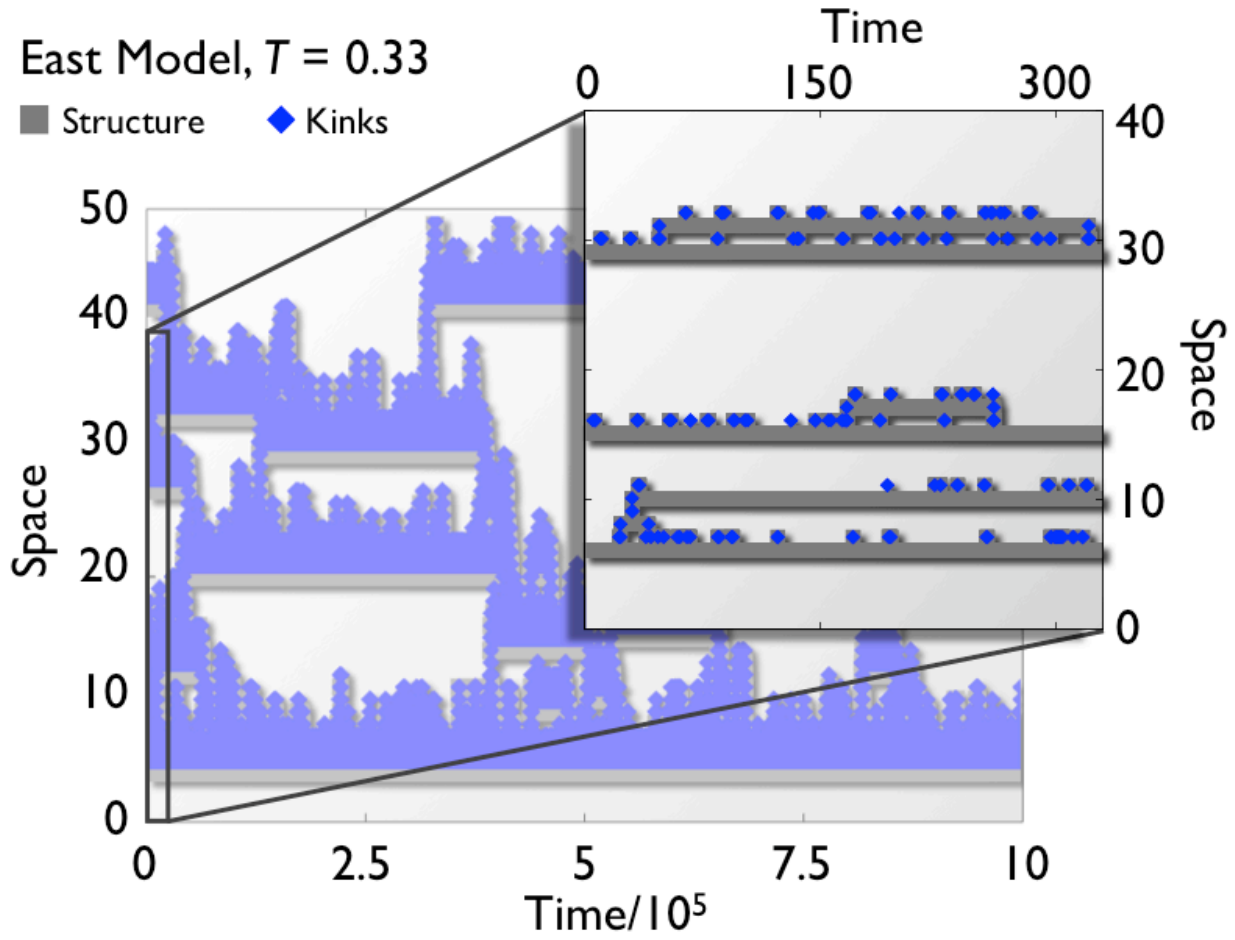

Figure 4.1: Trajectory of an east model with $T = 0.33$. Space is shown on the y-axis and time on the x-axis. Grey squares indicate structure where $n_i(t) = 1$. Blue diamonds indicate kinks where $\kappa_i(t) = 1$. Blowup in top right corner shows a zoomed in section highlighting the difference between structure and dynamics.

the possibility to accommodate mobility, but may not necessarily do so at any particular time point. Kinks, on the other hand, are locations where some kind of motion can necessarily be detected and correlate with a reorganization of the underlying mobility defects. For atomistic system, it is the kinks that are detected - not the defect "structure". However, the majority of kinks are located on an excitation front and are ephemeral. At first glance, these kinks seem to carry no dynamic facilitation. This is related to the surges seen in atomistic systems [50]. The challenge is to try to reconstruct the underlying mobility field to see dynamic facilitation in action in a way such that the information is carried by the kinks (which act as a recorder of this field) without directly detecting these defects.

Figure 4.1 highlights this challenge. For an east model, the kinks appear to be uncor-

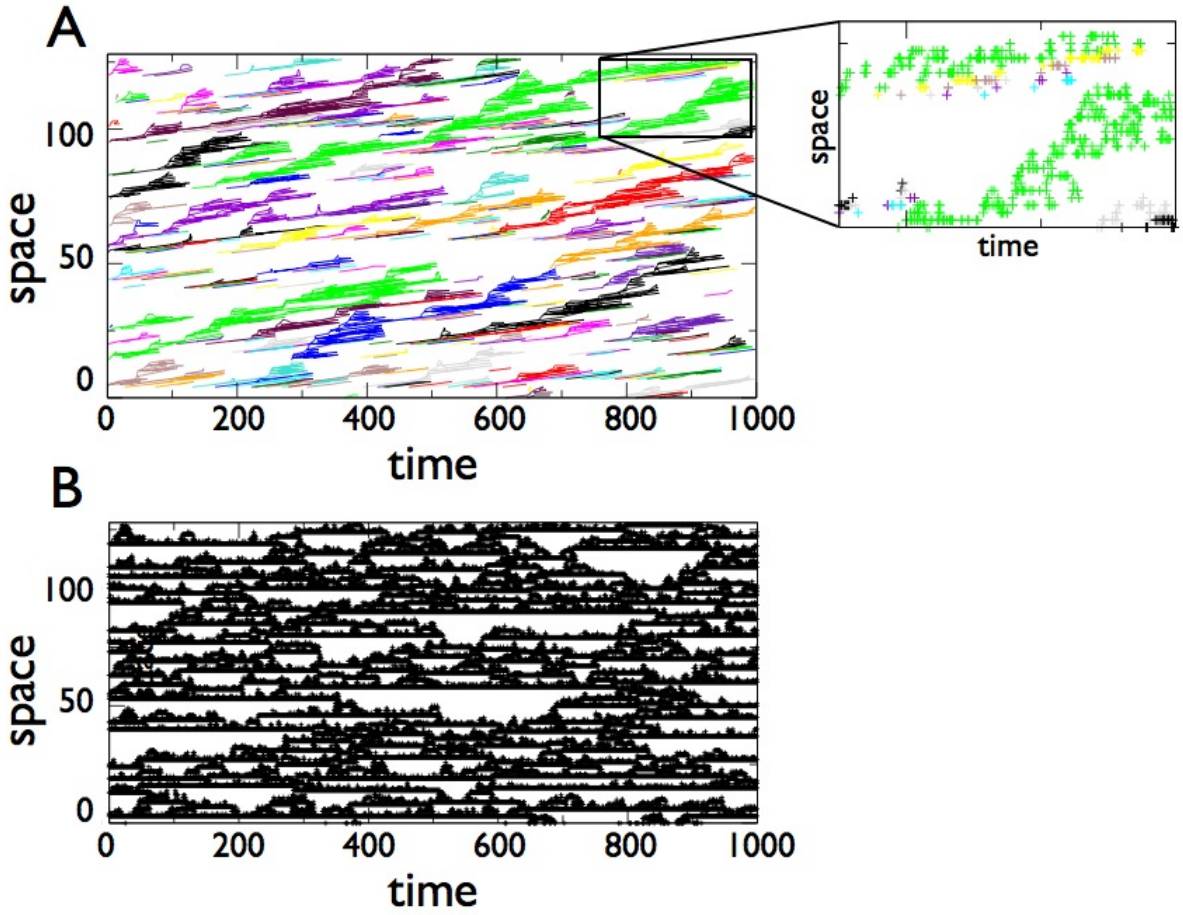

Figure 4.2: Candelier *et al* [21, 22] like analysis of the east model with an observation time of 1000 Monte Carlo time units, system size of 128 sites, and $T = 2$ showing seemingly uncorrelated avalanche events. (A) Avalanches in the east model. Different colors represent distinct avalanches. Points indicate kinks. Inset to (A) is zoomed in portion to show connectivity. (B) Fully connected structure of the same simulation used to generate (A).

related random events. Rather, it is the structure which carries the long time dynamic facilitation and the two only appear the same on long time and length scales.

4.2.4 Measuring Avalanches in KCMs

Candelier *et al* [22] suggest a method for determining the role of dynamic facilitation based on avalanches. An avalanche is a cluster of particles in space and time that relax together and cooperatively. Each avalanche is thus made up of smaller, sequential motions.

In the Candelier *et al* [22] method, particles are clustered into avalanches based on

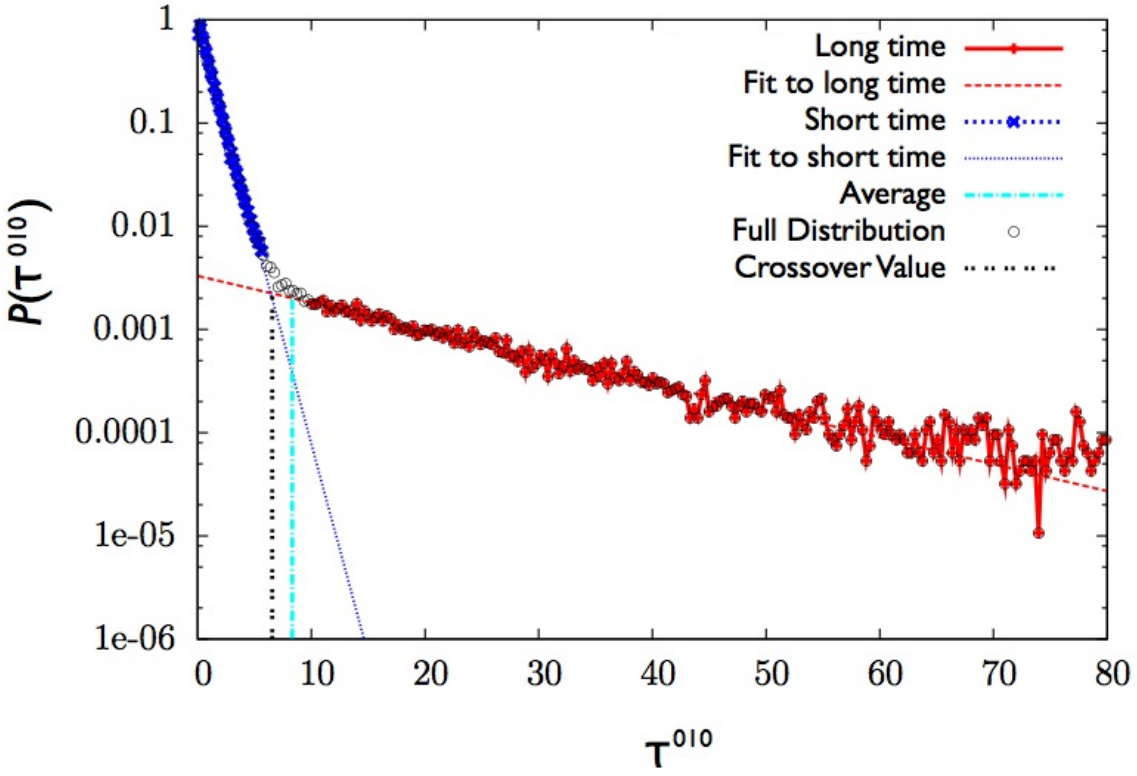

Figure 4.3: $n_i = 0 \rightarrow 1 \rightarrow 0$ Exchange time, τ^{010}, probability distribution, $P(\tau^{010})$, for east model with $T = 0.5$. Black circles represents the full distribution. Dark blue Xs depict the short time population, red points indicate the long time population. Dark blue dotted line is exponential fit to short time population, red dashed line is exponential fit to long time population. Light blue vertical line represents $\langle\tau^{010}\rangle$. Black vertical line represents crossover between the two populations.

whether not they have made a cage escape - defined as when a particle's vibrational center of motion has moved. If such cage events happen to particles who are nearest neighbors and within a time τ_{cl} much less than the structural relaxation time these two events are clustered together into to what Candelier *et al* describe as an elementary excitation. Candelier *et al* then measure the lag time τ_1 between nearby clusters which are separated in time by more than $\tau_{\rm cl}$ to determine their distribution $P(\tau_1)$. They find that τ_1 follows a double exponential distribution. They claim that the fast time part of the distribution is characterized by a time $\tau_{\rm S}$ which correlates to facilitated dynamics, whereas the longtime tail is characterized by a lagtime $\tau_{\rm L}$ which they believe corresponds to the birth of clusters which are not facilitated and arise spontaneously. Nearby spatial clusters of mobility which are separated in time by less than $\tau_{\rm S}$ are said to belong to the same avalanche.

Candelier *et al* [22] report that as a supercooled liquid is lowered below its onset tempera-

ture, their measure of dynamical facilitation seems to diminish. This apparent contradiction arises because the two definitions of dynamic facilitation are incompatible. This is because of the basic distinction between kinks and structure. What Candelier *et al* are measuring is not the underlying mobility defects but rather the detectable kinks. This is expected even in KCMs, as temperature is reduced the system does not have the energy to put together strings of adjacent kinks and spends the majority of its time placing kinks adjacent to an important structural defect and suggest that connecting these defects become even rarer. In order to determine which method can truly distinguish facilitated from non facilitated dynamics, it is useful to test the limits of these measures in models whose dynamics are extreme, such as KCMs. In KCMs such as the hard crossover model, relaxation is by definition facilitated as no 'softness' is permitted. Testing the cluster algorithm on such models can determine if avalanche behavior is present even in models which are fully constrained. If the same trends exists in hard KCMs, the avalanche method cannot truly distinguish between facilitated and non facilitated motion.

Figure 4.2 shows that the appearance and trends of avalanches in an east model mirrors the results of the atomic systems. This suggests that clustering avalanches does not discriminate between models with facilitation and those whose relaxation follows some alternate process. Moreover, preliminary evidence suggests that the same qualitative trends - namely the seeming decrease in the avalanche measure of dynamic facilitation as temperature is decreased - hold for KCMs. This is in light of the fact that KCMs have, built into their nature, increased dynamic facilitation with decreased temperature. This suggests that not only is the avalanche method poor at distinguishing between facilitated and non facilitated motion, it may in fact be picking up on increased dynamical facilitation as T is decreased.

The Candelier *et al* measure of dynamic facilitation seems to be related to exchange times where an exchange time in lattice system is the time between two kinks [29]. I define the lifetime of an excitation as τ^{010} - the time between a kink of type $n_i = 0 \rightarrow n_i = 1$ at site i until the next kink where $n_i = 1 \rightarrow n_i = 0$. This is also known as the exchange time for an excitation. Figure 4.3 shows the probability distribution for these lifetimes. This distribution appear to follow double exponential distribution - akin to the lag time distributions reported in Ref. [22]. In fact, in Ref. [22] they use these double exponetials and their temperature depencence as evidence of a diminishing role of dynamic facilitation – even though, once again, the same results can be found in fully facilitated model KCMs. The full exchange time distribution is given by $P(\tau^{010})/2$ plus its inverse $P(\tau^{101})/2$ (the lifetime of a vacancy) and also retains a double exponential distribution.

4.2.5 Measuring Facilitation

Since the avalanche picture for KCMs and atomistic models is identical, the presence of avalanches cannot preclude pure dynamic facilitation. Instead, we seek an alternative measure to describe the extent to which the system is facilitated. By definition, two point correlation functions of kinks such as the conditional average number of kinks at a distance

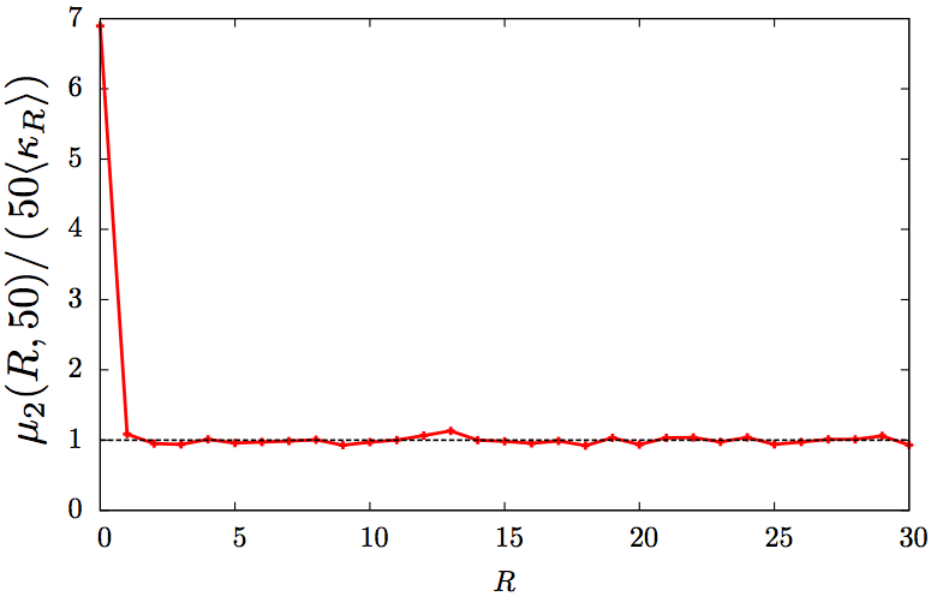

Figure 4.4: $\mu_2(R,t)/(t\cdot\langle\kappa_0(0)\rangle)$ as a function of R for an east model with $T=0.5$ and $t=50$. Red line indicates computed correlation function and black dashed line indicates the uncorrelated value, $(t\cdot\langle\kappa_0(0)\rangle)$.

R recorded during a time t given that a kink occurred at time $t=0$ at the origin $i=0$, $\mu_2(R,t)$ are given by

$$\mu_2(R,t)=\frac{\left\langle\kappa_0(0)\sum_{t'=0}^{t}\kappa_R(t')\right\rangle}{\langle\kappa_0(0)\rangle}=0,\quad R\neq 0\quad . \tag{4.11}$$

In Figure 4.4 a plot of μ_2 divided by $t\cdot\langle\kappa_0(0)\rangle$ is shown for an east model with $T=0.5$ and $t=50$ showing no interesting correlations. With $(t\cdot\langle\kappa_0(0)\rangle)$ being the uncorrelated value of $\mu_2(\infty,t)$ where we have used that all space and time points are equivalent. Here, R is only taken in the positive direction from the origin as the east model is not symmetric with respect to $-R\leftrightarrow R$. For all values of $R>0$ there are no correlations consistent with the underlying lattice gas thermodynamics of the system.

Instead, we will investigate correlation by using multipoint functions. We will look for long lived changes that stick or what will be known as an *enduring kink* which lasts at least a time Δt (which has not exchanged over a time Δt). This corresponds to finding kinks in

the second population of the exchange time distribution.

$$K_i(t, \Delta t) = \kappa_i(t) \prod_{t'=t+\delta t}^{\Delta t} (1 - \kappa_i(t')) \tag{4.12}$$

where $K_i(t, \Delta t)$ is a binary function that is 0 when there has been no enduring kink that first changed state at time t and 1 if there has been such an enduring kink at site i starting at time t. The motivation behind considering only enduring kinks is related to work done on measuring facilitation in atomistic systems where the short-lived surges are separating from the longer lived motions that stick. Next, we define a *doubly enduring kink* given by the function $h(i, t, t_a, \Delta t)$ which is also a binary function

$$h(i, t, t_a, \Delta t) = K_i(t - t_a, \Delta t) \left[1 - \delta \left(\sum_{t''=t-t_a+\Delta t}^{t-\Delta t} K_i(t'', \Delta t) \right) \right] \tag{4.13}$$

where t_a is a time period at least twice as long as Δt, t is a time, and $\delta(a)$ is the Dirac delta function where $\delta(a) = 1$ if $a = 0$ and $\delta(a) = 0$ if $a \neq 0$. $h(i, t, t_a, \Delta t) = 1$ at time t when for a previous time period of t_a there had been an enduring kink that started a time $t - t_a$ and then, in the subsequent period between time $t - t_a + \Delta t$ and time t there had been at least one more such enduring kink at the same site. By detecting at least two changes that enforces that at some point in the interval t_a there was a change from $n_i = 0 \rightarrow n_i = 1$ since in experimental systems, a detection of a kink is unknown as to wether or not it corresponds to a new defect ($n_i = 0 \rightarrow n_i = 1$) or the death of an old defect ($n_i = 1 \rightarrow n_i = 0$) and only the defects can facilitate relaxation. Then, to detect correlations, I will compute the following correlation function, $\mu(R, t, t_a, \Delta t)$

$$\mu(R, t, t_a, \Delta t) = \frac{\langle h(0, 0, t_a, \Delta t) \sum_0^t K_R(t, \Delta t) \rangle}{\langle h(0, 0, t_a, \Delta t) \rangle} \tag{4.14}$$

where R is the distance from the origin. This correlation function states that given that a double enduring kink event has finished at time 0 at the origin where $i = 0$ what is the average number of enduring kinks at a distance R from the origin in a time period 0 to t where now t is a counting time rather than an absolute time. We then define the facilitaiton volume $v_{\mathrm{F}}(t)$ as the sum over R of $\mu(R, t, t_a, \Delta t)$ such that

$$v_{\mathrm{F}}(t) = \sum_{R=0}^{\infty} \left(\frac{\mu(R, t, t_a, \Delta t)}{\mu_\infty(t, \Delta t)} - 1 \right) \tag{4.15}$$

where μ_∞ is the uncorrelated value of $\mu(R, t, t_a, \Delta t)$ as $R \rightarrow \infty$ or simply the average number of enduring kinks between time 0 and time t

$$\mu_\infty(t, \Delta t) = \left\langle \sum_{t'=0}^{t} K_0(t', \Delta t) \right\rangle \quad . \tag{4.16}$$

4.2.6 Conclusions

The measure of Candelier *et al* does not succeed in determining the true role of dynamic facilitation as it fails the test for a class of completely understood models - KCMs. We believe these measurements are trivially related to exchange and persistence processes already known to highlight the role of dynamic facilitation. Preliminary evidence shows that measures introduced here, such as the facilitation volume, can accurately capture the increasing role of dynamic facilitation as temperature is decreased in KCMs such as the crossover and arrow models. Moreover, these results appear to be consistent with recent measurements of correlation functions in atomistic models [50]. In the future, we also hope to determine how the facilitation changes as a function of the softness parameter ϵ where it will be interesting to understand the role of dynamic facilitation in light of the finite-temperature critical point found in Chapter 2.

Bibliography

[1] Y. S. Elmatad, D. Chandler, and J. P. Garrahan, "Corresponding states of structural glass formers," *Journal of Physical Chemistry B*, vol. 113, no. 16, pp. 5563–5567, 2009.

[2] Y. S. Elmatad, D. Chandler, and J. P. Garrahan, "Corresponding states of structural glass formers. II," *Journal of Physical Chemistry B*, vol. 114, pp. 17113–9, Dec. 2010.

[3] Y. S. Elmatad, "Fragile-to-strong crossover in supercooled liquids remains elusive," *Proceedings of the National Academy of Sciences*, vol. 108, p. E230, June 2011.

[4] Y. S. Elmatad, R. L. Jack, J. P. Garrahan, and D. Chandler, "Finite-temperature critical point of a glass transition," *Proceedings of the National Academy of Sciences*, vol. 107, no. 29, pp. 12793–12798, 2010.

[5] S. Swallen, P. Bonvallet, R. McMahon, and M. Ediger, "Self-Diffusion of tris-Naphthylbenzene near the Glass Transition Temperature," *Physical Review Letters*, vol. 90, Jan. 2003.

[6] C. A. Angell, "Relaxation in liquids, polymers and plastic crystals – strong/fragile patterns and problems," *Journal of Non-Crystalline Solids*, vol. 131-133, pp. 13–31, June 1991.

[7] Y. Gebremichael, *Spatially Heterogeneous Dynamics and String-like Correlated Motion in Supercooled Liquids and Polymers*. PhD thesis, University of Michigan, 2004.

[8] H. Shintani and H. Tanaka, "Universal link between the boson peak and transverse phonons in glass," *Nature Materials*, vol. 7, no. 11, pp. 870–877, 2008.

[9] N. Lacevic, F. W. Starr, T. B. Schroder, and S. C. Glotzer, "Spatially heterogeneous dynamics investigated via a time-dependent four-point density correlation function," *The Journal of Chemical Physics*, vol. 119, no. 14, pp. 7372–7387, 2003.

[10] L. Berthier and W. Kob, "The Monte Carlo dynamics of a binary Lennard-Jones glass-forming mixture," *Journal of Physics: Condensed Matter*, vol. 19, no. 20, p. 205130 (10pp), 2007.

[11] S. Karmakar, C. Dasgupta, and S. Sastry, "Growing length and time scales in glass-forming liquids," *Proceedings of the National Academy of Sciences*, vol. 106, pp. 3675–9, Mar. 2009.

[12] L. O. Hedges, L. Maibaum, D. Chandler, and J. P. Garrahan, "Decoupling of exchange and persistence times in atomistic models of glass formers," *Journal of Chemical Physics*, vol. 127, no. 21, p. 211101, 2007.

[13] C. A. Angell, "Entropy and Fragility in Supercooling Liquids," *J. Res. Nat. Inst. Stand.*, vol. 102, p. 171, Mar. 1997.

[14] J. C. Mauro, Y. Yue, A. J. Ellison, P. K. Gupta, and D. C. Allan, "Viscosity of glass-forming liquids," *Proceedings of the National Academy of Sciences*, vol. 106, no. 47, pp. 19780–4, 2009.

[15] H. Tweer, J. H. Simmons, and P. B. Macedo, "Application of the Environmental Relaxation Model to the Temperature Dependence of the Viscosity," *The Journal of Chemical Physics*, vol. 54, no. 5, pp. 1952–1959, 1971.

[16] N. B. Olsen, T. Christensen, and J. C. Dyre, "Time-Temperature Superposition in Viscous Liquids," *Physical Review Letters*, vol. 86, pp. 1271–1274, Feb. 2001.

[17] L. Berthier and G. Tarjus, "Nonperturbative Effect of Attractive Forces in Viscous Liquids," *Physical Review Letters*, vol. 103, Oct. 2009.

[18] F. Mallamace, C. Branca, C. Corsaro, N. Leone, J. Spooren, S.-H. Chen, and H. E. Stanley, "Transport properties of glass-forming liquids suggest that dynamic crossover temperature is as important as the glass transition temperature," *Proceedings of the National Academy of Sciences*, vol. 107, no. 52, pp. 22457–22462, 2010.

[19] R. L. Jack, J. P. Garrahan, and D. Chandler, "Space-time thermodynamics and subsystem observables in a kinetically constrained model of glassy materials," *Journal of Chemical Physics*, vol. 125, no. 184509, pp. 184509–184511, 2006.

[20] J. P. Garrahan, R. L. Jack, V. Lecomte, E. Pitard, K. van Duijvendijk, and F. van Wijland, "Dynamical first-order phase transition in kinetically constrained models of glasses," *Physical Review Letters*, vol. 98, no. 19, p. 195702, 2007.

[21] R. Candelier, O. Dauchot, and G. Biroli, "Dynamical facilitation decreases when approaching the granular glass transition," *Europhysics Letters*, Oct. 2010.

[22] R. Candelier, A. W. Cooper, J. K. Kummerfeld, O. Dauchot, G. Biroli, P. Harrowell, and D. R. Reichman, "Spatiotemporal Hierarchy of Relaxation Events, Dynamical Heterogeneities, and Structural Reorganization in a Supercooled Liquid," *Physical Review Letters*, vol. 105, no. 13, 2010.

[23] M. D. Ediger, C. A. Angell, and S. R. Nagel, "Supercooled Liquids and Glasses," *Journal of Physical Chemistry A*, vol. 100, no. 31, pp. 13200–13212, 1996.

[24] P. G. Debenedetti and F. H. Stillinger, "Supercooled liquids and the glass transition," *Nature*, vol. 410, no. 6825, pp. 259–267, 2001.

[25] D. Chandler, *Introduction to Modern Statistical Mechanics*. Oxford University Press, USA, 1987.

[26] L. Berthier and G. Biroli, "Theoretical perspective on the glass transition and amorphous materials," *Reviews of Modern Physics*, vol. 83, no. 2, pp. 587–645, 2011.

[27] J.-P. Hansen and I. McDonald, *Theory of Simple Liquids, Third Edition*. Academic Press, 2006.

[28] W. Gotze and L. Sjogren, "Relaxation processes in supercooled liquids," *Reports on Progress in Physics*, vol. 55, pp. 241–376, Mar. 1992.

[29] Y. Jung, J. Garrahan, and D. Chandler, "Excitation lines and the breakdown of Stokes-Einstein relations in supercooled liquids," *Physical Review E*, vol. 69, p. 061205, June 2004.

[30] M. D. Ediger, "Spatially heterogeneous dynamics in supercooled liquids," *Annual Review of Physical Chemistry*, vol. 51, no. 1, pp. 99–128, 2000.

[31] A. S. Keys, A. R. Abate, S. C. Glotzer, and D. J. Durian, "Measurement of growing dynamical length scales and prediction of the jamming transtion in a granular material," *Nature Physics*, vol. 3, pp. 260–264, 2007.

[32] J. Lynch, G. Cianci, and E. Weeks, "Dynamics and structure of an aging binary colloidal glass," *Physical Review E*, vol. 78, Sept. 2008.

[33] L.-M. Wang, V. Velikov, and C. A. Angell, "Direct determination of kinetic fragility indices of glassforming liquids by differential scanning calorimetry: Kinetic versus thermodynamic fragilities," *The Journal of Chemical Physics*, vol. 117, no. 22, pp. 10184–10192, 2002.

[34] W. Kob and H. Andersen, "Testing mode-coupling theory for a supercooled binary Lennard-Jones mixture. II. Intermediate scattering function and dynamic susceptibility," *Physical Review E*, vol. 52, pp. 4134–4153, Oct. 1995.

[35] J. P. Garrahan and D. Chandler, "Coarse-grained microscopic model of glass formers," *Proceedings of the National Academy of Sciences*, vol. 100, no. 17, pp. 9710–9714, 2003.

[36] H. Vogel, "Das Temperaturabhängigkeitsgesetz der Viskosität von Flüssigkeiten," *Zeitschrift Für Physik*, vol. 22, pp. 645—-646, 1921.

[37] D. R. Reichman and P. Charbonneau, "Mode-coupling theory," *Journal of Statistical Mechanics: Theory and Experiment*, vol. 2005, p. P05013, May 2005.

[38] G. Adam and J. H. Gibbs, "On the Temperature Dependence of Cooperative Relaxation Properties in Glass-Forming Liquids," *Journal of Chemical Physics*, vol. 43, no. 1, pp. 139–146, 1965.

[39] G. S. Fulcher, "Analysis of Recent Measurements of the Viscosity of Glasses," *Journal of the American Ceramic Society*, vol. 8, no. 6, pp. 339–355, 1925.

[40] G. Tammann and W. Hesse, "Die Abhangigkeit der Viscositat von der Temperatur bie unterkuhlten Flussigkeiten," *Zeitschrift fur anorganische und allgemeine Chemie*, vol. 156, pp. 245–257, Sept. 1926.

[41] V. Lubchenko and P. G. Wolynes, "Theory of Structural Glasses and Supercooled Liquids," *Annual Review of Physical Chemistry*, vol. 58, no. 1, pp. 235–266, 2007.

[42] J. D. Stevenson, J. Schmalian, and P. G. Wolynes, "The shapes of cooperatively rearranging regions in glass-forming liquids," *Nature Physics*, vol. 2, pp. 268–274, Mar. 2006.

[43] E. Rössler, K.-U. Hess, and V. N. Novikov, "Universal representation of viscosity in glass forming liquids," *Journal of Non-Crystalline Solids*, vol. 223, pp. 207–222, 1998.

[44] E. J. Saltzman and K. S. Schweizer, "Universal scaling, dynamic fragility, segmental relaxation, and vitrification in polymer melts," *Journal of Chemical Physics*, vol. 121, pp. 2001–9, July 2004.

[45] D. Chandler and J. P. Garrahan, "Dynamics on the way to forming glass: bubbles in space-time," *Annual Review of Physical Chemistry*, vol. 61, pp. 191–217, Mar. 2010.

[46] G. H. Fredrickson and H. C. Andersen, "Kinetic Ising Model of the Glass Transition," *Physical Review Letters*, vol. 53, no. 13, pp. 1244–1247, 1984.

[47] A. C. Pan, J. P. Garrahan, and D. Chandler, "Heterogeneity and growing lenth scales in the dynamics of kinetically constrained lattice gases in two dimensions," *Physical Review E*, vol. 72, pp. 1–2005, Oct. 2005.

[48] J. Jackle and A. Kronig, "A kinetic lattice-gas model for the triangular lattice with strong dynamic correlations. I. Self-diffusion," *Journal of Physics: Condensed Matter*, vol. 6, no. 38, p. 7633, 1994.

[49] A. C. Pan, D. Chandler, and J. P. Garrahan, "Decoupling of Self-Diffusion and Structural Relaxation during a Fragile-to-Strong Crossover in a Kinetically Constrained Lattice Gas," *ChemPhysChem*, vol. 6, no. 9, pp. 1783–1785, 2005.

[50] A. S. Keys, L. O. Hedges, J. P. Garrahan, S. C. Glotzer, and D. Chandler, "Excitations are localized and relaxation is hierarchical in glass-forming liquids," *arXiv:cond-mat*, vol. 1107.3628, July 2011.

[51] N. Xu, T. K. Haxton, A. J. Liu, and S. R. Nagel, "Equivalence of Glass Transition and Colloidal Glass Transition in the Hard-Sphere Limit," *Physical Review Letters*, vol. 103, p. 4, Dec. 2009.

[52] H. M. Lindsay, W. D. Dozier, P. M. Chaikin, R. Klein, and W. Hess, "On the viscosity and shear modulus of strongly interacting colloids," *Journal of Physics A*, vol. 19, Sept. 1986.

[53] M. Merolle, J. P. Garrahan, and D. Chandler, "Space-time thermodynamics of the glass transition," *Proceedings of the National Academy of Sciences*, vol. 102, no. 31, pp. 10837–10840, 2005.

[54] T. Hecksher, A. I. Nielsen, N. B. Olsen, and J. C. Dyre, "Little evidence for dynamic divergences in ultraviscous molecular liquids," *Nature Physics*, vol. 4, no. 9, pp. 737–741, 2008.

[55] J. P. Garrahan and D. Chandler, "Coarse-grained microscopic model of glass formers," *Proceedings of the National Academy of Sciences*, vol. 100, pp. 9710–9714, Aug. 2003.

[56] J. Jonas, "Nuclear Magnetic Resonance at High Pressure," *Science*, vol. 216, no. 4551, pp. 1179–1184, 1982.

[57] D. Chandler, J. D. Weeks, and H. C. Andersen, "Van der Waals Picture of Liquids, Solids, and Phase Transformations," *Science*, vol. 220, no. 4599, pp. 787–794, 1983.

[58] R. G. Palmer, D. L. Stein, E. Abrahams, and P. W. Anderson, "Models of Hierarchically Constrained Dynamics for Glassy Relaxation," *Physical Review Letters*, vol. 53, pp. 958–961, Sept. 1984.

[59] E. W. Fischer, "Light scattering and dielectric studies on glass forming liquids," *Physica A: Statistical Mechanics and its Applications*, vol. 201, pp. 183–206, Dec. 1993.

[60] F. Stickel, E. W. Fischer, and R. Richert, "Dynamics of glass-forming liquids. II. Detailed comparison of dielectric relaxation, dc-conductivity, and viscosity data," *The Journal of Chemical Physics*, vol. 104, no. 5, p. 2043, 1996.

[61] D. Kivelson, S. Kivelson, X. Zhao, Z. Nussinov, and G. Tarjus, "A thermodynamic theory of supercooled liquids," *Physica A: Statistical and Theoretical Physics*, vol. 219, pp. 27–38, Sept. 1995.

[62] D. Kivelson, G. Tarjus, X. Zhao, and S. Kivelson, "Fitting of viscosity: Distinguishing the temperature dependences predicted by various models of supercooled liquids," *Physical Review E*, vol. 53, pp. 751–758, Jan. 1996.

[63] B. Igarashi, T. Christensen, E. H. Larsen, N. B. Olsen, I. H. Pedersen, T. Rasmussen, and J. C. Dyre, "A cryostat and temperature control system optimized for measuring relaxations of glass-forming liquids," *Review of Scientific Instruments*, vol. 79, no. 4, p. 45105, 2008.

[64] B. Igarashi, T. Christensen, E. H. Larsen, N. B. Olsen, I. H. Pedersen, T. Rasmussen, and J. C. Dyre, "An impedance-measurement setup optimized for measuring relaxations of glass-forming liquids," *Review of Scientific Instruments*, vol. 79, no. 4, p. 45106, 2008.

[65] B. Jakobsen, K. Niss, and N. B. Olsen, "Dielectric and shear mechanical alpha and beta relaxations in seven glass-forming liquids," *The Journal of Chemical Physics*, vol. 123, no. 23, p. 234511, 2005.

[66] D. R. Neuville, "Viscosity, structure and mixing in (Ca, Na) silicate melts," *Chemical Geology*, vol. 229, no. 1-3, pp. 28–41, 2006.

[67] F. H. Stillinger, "Supercooled liquids, glass transitions, and the Kauzmann paradox," *The Journal of Chemical Physics*, vol. 88, no. 12, pp. 7818–7825, 1988.

[68] J. G. Berberian and R. H. Cole, "Approach to glassy behavior of dielectric relaxation in 3-bromopentane from 298 to 107 K," *The Journal of Chemical Physics*, vol. 84, no. 12, pp. 6921–6927, 1986.

[69] T. Blochowicz, *Broadband Dielectric Spectroscopy in Neat and Binary Molecular Glass Formers Frequency and Time Domain Spectroscopy, Non-Resonant Spectral Hole Burning*. PhD thesis, Universitat Bayreuth, 2003.

[70] P. Lunkenheimer, L. C. Pardo, M. Kohler, and A. Loidl, "Broadband dielectric spectroscopy on benzophenone: alpha relaxation, beta relaxation, and mode coupling theory," *Journal of Physics E*, vol. 77, no. 3, p. 31506, 2008.

[71] N. Ito, K. Duvvuri, D. V. Matyushov, and R. Richert, "Solvent response and dielectric relaxation in supercooled butyronitrile," *The Journal of Chemical Physics*, vol. 125, no. 2, p. 24504, 2006.

[72] K. L. Ngai and M. Paluch, "Classification of secondary relaxation in glass-formers based on dynamic properties," *The Journal of Chemical Physics*, vol. 120, no. 2, pp. 857–873, 2004.

[73] C. A. Angell, "Structural instability and relaxation in liquid and glassy phases near the fragile liquid limit," *Journal of Non-Crystalline Solids*, vol. 102, no. 1-3, pp. 205–221, 1988.

[74] N. Ito, W. Huang, and R. Richert, "Dynamics of a Supercooled Ionic Liquid Studied by Optical and Dielectric Spectroscopy," *Journal of Physical Chemistry B*, vol. 110, no. 9, pp. 4371–4377, 2006.

[75] R. Diaz-Calleja, A. Garcia-Bernabe, M. J. Sanchis, and L. F. del Castillo, "Interconversion of mechanical and dielectrical relaxation measurements for dicyclohexylmethyl-2-methyl succinate," *Journal of Physics E*, vol. 72, no. 5, p. 51505, 2005.

[76] L.-M. Wang and R. Richert, "Debye Type Dielectric Relaxation and the Glass Transition of Alcohols," *Journal of Physical Chemistry B*, vol. 109, no. 22, pp. 11091–11094, 2005.

[77] M. Mierzwa, S. Pawlus, M. Paluch, E. Kaminska, and K. L. Ngai, "Correlation between primary and secondary Johari–Goldstein relaxations in supercooled liquids: Invariance to changes in thermodynamic conditions," *The Journal of Chemical Physics*, vol. 128, no. 4, p. 44512, 2008.

[78] J. Wiedersich, T. Blochowicz, S. Benkhof, A. Kudlik, N. V. Surovtsev, C. Tschirwitz, V. N. Novikov, and E. Rossler, "Fast and slow relaxation processes in glasses," *Journal of Physics: Condensed Matter*, vol. 11, no. 10A, pp. A147–A156, 1999.

[79] M. Paluch, K. L. Ngai, and S. Hensel-Bielowka, "Pressure and temperature dependences of the relaxation dynamics of cresolphthalein-dimethylether: Evidence of contributions from thermodynamics and molecular interactions," *The Journal of Chemical Physics*, vol. 114, no. 24, pp. 10872–10883, 2001.

[80] T. Blochowicz, C. Gainaru, P. Medick, C. Tschirwitz, and E. A. Rössler, "The dynamic susceptibility in glass forming molecular liquids: The search for universal relaxation patterns II," *Journal of Chemical Physics*, vol. 124, pp. 134503–134511, 2006.

[81] R. Richert and C. A. Angell, "Dynamics of glass-forming liquids. V. On the link between molecular dynamics and configurational entropy," *The Journal of Chemical Physics*, vol. 108, no. 21, pp. 9016–9026, 1998.

[82] R. Richert, "On the dielectric susceptibility spectra of supercooled o-terphenyl," *Journal of Chemical Physics*, vol. 123, no. 15, p. 154502, 2005.

[83] W. T. Laughlin and D. R. Uhlmann, "Viscous flow in simple organic liquids," *Journal of Physical Chemistry*, vol. 76, no. 16, pp. 2317–2325, 1972.

[84] S. Hensel-Bielowka and M. Paluch, "Origin of the High-Frequency Contributions to the Dielectric Loss in Supercooled Liquids," *Physical Review Letters*, vol. 89, p. 25704, June 2002.

[85] D. L. Plazek and D. J. Plazek, "Viscoelastic behavior of atactic polypropylene," *Macromolecules*, vol. 16, no. 9, pp. 1469–1475, 1983.

[86] M. Liska, P. Simurka, J. Antalík, and P. Perichta, "Viscosity of titania-bearing sodium silicate melts," *Chemical Geology*, vol. 128, no. 1-4, pp. 199–206, 1996.

[87] P. K. Dixon, N. Menon, and S. R. Nagel, "Comment on Light-scattering investigation of alpha and beta relaxation near the liquid-gas transition of the molecular glass Salol," *Physical Review E*, vol. 50, no. 2, pp. 1717–1719, 1994.

[88] C. Gainaru, A. Rivera, S. Putselyk, G. Eska, and E. A. Rossler, "Low-temperature dielectric relaxation of molecular glasses: Crossover from the nearly constant loss to the tunneling regime," *Physical Review B (Condensed Matter and Materials Physics)*, vol. 72, no. 17, p. 174203, 2005.

[89] J. R. Rajian, W. Huang, R. Richert, and E. L. Quitevis, "Enhanced translational diffusion of rubrene in sucrose benzoate," *The Journal of Chemical Physics*, vol. 124, no. 1, p. 14510, 2006.

[90] D. J. Plazek and J. H. Magill, "Physical Properties of Aromatic Hydrocarbons. I. Viscous and Viscoelastic Behavior of 1:3:5-Tri-alpha-Naphthyl Benzene," *The Journal of Chemical Physics*, vol. 45, no. 8, pp. 3038–3050, 1966.

[91] R. Richert, K. Duvvuri, and L.-T. Duong, "Dynamics of glass-forming liquids. VII. Dielectric relaxation of supercooled tris-naphthylbenzene, squalane, and decahydroisoquinoline," *The Journal of Chemical Physics*, vol. 118, no. 4, pp. 1828–1836, 2003.

[92] A. Doss, G. Hinze, B. Schiener, J. Hemberger, and R. Bohmer, "Dielectric relaxation in the fragile viscous liquid state of toluene," *The Journal of Chemical Physics*, vol. 107, no. 6, pp. 1740–1743, 1997.

[93] L. M. Martinez and C. A. Angell, "A thermodynamic connection to the fragility of glass-forming liquids," *Nature*, vol. 410, no. 6829, pp. 663–667, 2001.

[94] M. Wyart, "Correlations between Vibrational Entropy and Dynamics in Liquids," *Physical Review Letters*, vol. 104, Mar. 2010.

[95] C. Toninelli, G. Biroli, and D. S. Fisher, "Jamming Percolation and Glass Transitions in Lattice Models," *Physical Review Letters*, vol. 96, no. 3, 2006.

[96] H. Tanaka, "Relation between Thermodynamics and Kinetics of Glass-Forming Liquids," *Physical Review Letters*, vol. 90, no. 5, 2003.

[97] D. Plazek, C. Bero, and I. Chay, "The recoverable compliance of amorphous materials," *Journal of Non-Crystalline Solids*, vol. 172-174, pp. 181–190, Sept. 1994.

[98] C. Toninelli, G. Biroli, and D. S. Fisher, "Cooperative Behavior of Kinetically Constrained Lattice Gas Models of Glassy Dynamics," *Journal of Statistical Physics*, vol. 120, pp. 167–238, Aug. 2005.

[99] P. Lunkenheimer, S. Kastner, M. Köhler, and A. Loidl, "Temperature development of glassy α -relaxation dynamics determined by broadband dielectric spectroscopy," *Physical Review E*, vol. 81, May 2010.

[100] W. Kob and H. C. Andersen, "Scaling Behavior in the -Relaxation Regime of a supercooled Lennard-Jones mixture," *Physical Review Letters*, vol. 73, no. 10, pp. 1376–1379, 1994.

[101] J. D. Weeks, D. Chandler, and H. C. Andersen, "Role of Repulsive Forces in Determining the Equilibrium Structure of Simple Liquids," *The Journal of Chemical Physics*, vol. 54, no. 12, p. 5237, 1971.

[102] T. B. Schroder, N. P. Bailey, U. R. Pedersen, N. Gnan, and J. C. Dyre, "Pressure-energy correlations in liquids. III. Statistical mechanics and thermodynamics of liquids with hidden scale invariance," *Journal of Chemical Physics*, vol. 131, p. 234503, Dec. 2009.

[103] U. Pedersen, T. Schrø der, and J. Dyre, "Repulsive Reference Potential Reproducing the Dynamics of a Liquid with Attractions," *Physical Review Letters*, vol. 105, Oct. 2010.

[104] S. H. Chen, Y. Zhang, M. Lagi, S. H. Chong, P. Baglioni, and F. Mallamace, "Evidence of dynamic crossover phenomena in water and other glass-forming liquids: experiments, MD simulations and theory," *Journal of Physics: Condensed Matter*, vol. 21, no. 50, 2009.

[105] S.-H. Chen, L. Liu, E. Fratini, P. Baglioni, A. Faraone, and E. Mamontov, "Observation of fragile-to-strong dynamic crossover in protein hydration water," *Proceedings of the National Academy of Sciences*, vol. 103, no. 24, pp. 9012–9016, 2006.

[106] R. Richert and C. A. Angell, "Dynamics of glass-forming liquids. V. On the link between molecular dynamics and configurational entropy," *The Journal of Chemical Physics*, vol. 108, no. 21, pp. 9016–9026, 1998.

[107] D. A. McQuarrie and J. D. Simon, *Physical Chemistry: A Molecular Approach*. University Science Books, 1997.

[108] M. E. J. Newman and G. T. Barkema, *Monte Carlo Methods in Statistical Physics*. Oxford University Press, USA, 1999.

[109] R. J. Allen, C. Valeriani, and P. Rein Ten Wolde, "Forward flux sampling for rare event simulations," *J. Phys.-Condens. Mat.*, vol. 21, p. 463102, Nov. 2009.

[110] W. E, W. Ren, and E. Vanden-Eijnden, "String method for the study of rare events," *Physical Review B*, vol. 66, p. 052301, Aug. 2002.

[111] P. G. Bolhuis, D. Chandler, C. Dellago, and P. L. Geissler, "Transition Path Sampling: Throwing Ropes Over Rough Mountain Passes, in the Dark," *Annual Review of Physical Chemistry*, vol. 53, pp. 291–318, 2002.

[112] V. Lecomte, C. A. Rolland, and F. van Wijland, "Chaotic Properties of Systems with Markov Dynamics," *Physical Review Letters*, vol. 95, no. 1, 2005.

[113] V. Lecomte, C. Appert-Rolland, and F. van Wijland, "Thermodynamic Formalism for Systems with Markov Dynamics," *Journal of Statistical Physics*, vol. 127, pp. 51–106, Apr. 2007.

[114] D. Ruelle, *Thermodynamic Formalism (Encyclopedia of Mathematics and its Applications)*. Cambridge University Press, 1984.

[115] J. Hooyberghs and C. Vanderzande, "Thermodynamics of histories for the one-dimensional contact process," *Journal of Statistical Mechanics: Theory and Experiment*, vol. 2010, p. P02017, Feb. 2010.

[116] M. Baiesi, C. Maes, and B. Wynants, "Fluctuations and Response of Nonequilibrium States," *Physical Review Letters*, vol. 103, no. 1, 2009.

[117] L. O. Hedges, R. L. Jack, J. P. Garrahan, and D. Chandler, "Dynamic order-disorder in atomistic models of structural glass formers," *Science*, vol. 323, no. 5919, pp. 1309–1313, 2009.

[118] T. Speck and J. P. Garrahan, "Space-time phase transitions in driven kinetically constrained lattice models," *The European Physical Journal B*, vol. 79, pp. 1–6, Dec. 2010.

[119] J. J. Sakurai, *Modern Quantum Mechanics (Revised Edition)*. Addison Wesley, 1993.

[120] R. L. Jack, P. Mayer, and P. Sollich, "Mappings between reactiondiffusion and kinetically constrained systems: A+A A and the FredricksonAndersen model have upper critical dimension dc = 2," *Journal of Statistical Mechanics: Theory and Experiment*, vol. 2006, Mar. 2006.

[121] S. Sachdev, *Quantum Phase Transitions*. Cambridge University Press, 2000.

[122] R. L. Jack and P. Sollich, "Large Deviations and Ensembles of Trajectories in Stochastic Models," *Progress of Theoretical Physics Supplement*, vol. 184, pp. 304–317, 2010.

[123] M. Doi, "Second quantization representation for classical many-particle system," *Journal of Physics A*, vol. 9, pp. 1465–1477, Sept. 1976.

[124] R. Stinchcombe, "Stochastic non-equilibrium systems," *Advances in Physics*, vol. 50, pp. 431–496, July 2001.

[125] L. Peliti, "Field theory for birth-death processes on a lattice," *J. Physique-Paris*, vol. 46, pp. 1469–1483, 1985.

[126] J. P. Garrahan, R. L. Jack, V. Lecomte, E. Pitard, K. van Duijvendijk, and F. van Wijland, "First-order dynamical phase transition in models of glasses: an approach based on ensembles of histories," *Journal of Physics A*, vol. 42, no. 7, p. 29, 2008.

[127] R. V. Hogg, A. Craig, and J. W. McKean, *Introduction to Mathematical Statistics*. Prentice Hall, 2004.

[128] F. Ritort and P. Solich, "Glassy dynamics of kinetically constrained models," *Advances in Physics*, vol. 52, pp. 219–342, 2003.

[129] S. Whitelam, L. Berthier, and J. P. Garrahan, "Dynamic Criticality in Glass-Forming Liquids," *Physical Review Letters*, vol. 92, no. 18, 2004.

[130] T. R. Kirkpatrick and D. Thirumalai, "p-spin-interaction spin-glass models: Connections with the structural glass problem," *Physical Review B*, vol. 36, no. 10, pp. 5388–5397, 1987.

[131] T. R. Kirkpatrick and P. G. Wolynes, "Connections between some kinetic and equilibrium theories of the glass transition," *Physical Review A*, vol. 35, no. 7, pp. 3072–3080, 1987.

[132] R. L. Jack and J. P. Garrahan, "Metastable states and space-time phase transitions in a spin-glass model," *Physical Review E*, vol. 81, no. 1, 2010.

[133] B. Gaveau and L. S. Schulman, "Theory of nonequilibrium first-order phase transitions for stochastic dynamics," *Journal of Mathematical Physics*, vol. 39, no. 3, pp. 1517–1533, 1998.

[134] G. Biroli and J. Kurchan, "Metastable states in glassy systems," *Physical Review E*, vol. 64, no. 1, 2001.

[135] H. Tanaka, "Two-order-parameter model of the liquid-glass transition. II. Structural relaxation and dynamic heterogeneity," *Journal of Non-Crystalline Solids*, vol. 351, pp. 3385–3395, Nov. 2005.

[136] L. Xu, P. Kumar, S. V. Buldyrev, S.-H. Chen, P. H. Poole, F. Sciortino, and H. E. Stanley, "Relation between the Widom line and the dynamic crossover in systems with a liquid-liquid phase transition," *Proceedings of the National Academy of Sciences*, vol. 102, pp. 16558–16562, Nov. 2005.

[137] S. F. Swallen, K. Traynor, R. J. McMahon, M. D. Ediger, and T. E. Mates, "Self-diffusion of supercooled tris-naphthylbenzene," *The Journal of Physical Chemistry B*, vol. 113, pp. 4600–8, Apr. 2009.

[138] J. P. Garrahan and D. Chandler, "Geometrical Explanation and Scaling of Dynamical Heterogeneities in Glass Forming Systems," *Physical Review Letters*, vol. 89, no. 3, 2002.

[139] X. Xia and P. G. Wolynes, "Fragilities of liquids predicted from the random first order transition theory of glasses," *Proceedings of the National Academy of Sciences*, vol. 97, no. 7, pp. 2990–2994, 2000.

[140] M. N. J. Bergroth, M. Vogel, and S. C. Glotzer, "Examination of dynamic facilitation in molecular dynamics simulations of glass-forming liquids," *The Journal of Physical Chemistry B*, vol. 109, pp. 6748–53, Apr. 2005.

[141] M. Vogel and S. C. Glotzer, "Spatially Heterogeneous Dynamics and Dynamic Facilitation in a Model of Viscous Silica," *Physical Review Letters*, vol. 92, no. 25, 2004.